UNIVERSITY OF
BIRMINGHAM

COHERENT CHANGE DETECTION WITH GNSS-BASED SAR
- EXPERIMENTAL STUDY -

by

DIMITRIOS TZAGKAS

A thesis submitted to Electronic, Electrical and System Engineering of
The University of Birmingham
for the Degree of
DOCTOR OF PHILOSOPHY

March 2017

Abstract

Bistatic Synthetic Aperture Radar (BSAR) systems are under an increasing amount of research activity over the last years. The possibility of the use of transmitters of opportunity has increased the flexibility and the applications of radar systems. One of the options is the use of Global Navigation Satellite Systems (GNSS) as transmitters, such as GPS, GLONASS or the forthcoming Galileo and Beidou, that is used in this study. This thesis is the result of the study of a GNSS-based SAR used for detection of changes that may occur in a scene. Although passive SAR is outclassed by active SAR in terms of SAR imaging performance, Coherent Change Detection applications in passive SAR can be promising. A proof-of-concept study is presented in this thesis. The connection between spatial target change and the level of coherence before and after the change is investigated. The stages of theoretical analysis and experimental setup are described in detail. Simulated scenarios are presented and the experimental results are analysed.

Acknowledgements

First and foremost, I would like to thank my thesis supervisors, Dr. M. Antoniou and Prof. M. Cherniakov, for their support and guidance through the whole period of my PhD. Their passion and encouragement during these years were very important for the completion of my work.

I would like to thank the technical manager Andy Dunn and the technician Alan Yates of the Department of Electronics, Electrical and Systems Engineering for the help about the experimentation setups and provisions on health and safety.

Special thanks go to PhD and postdoctoral researchers of my group Hui Ma, Hanning Wang, Stanislav Hristov, Alp Sayin and Sukhjit Pooni.

Also, I would like to acknowledge the financial support from the school and from EPSRC.

To my wife Ana Maria and my family,

CONTENTS

List of Figures

List of Tables

Chapter 1 Introduction

1.1. Radar Concept

Radar is an object detection system using electromagnetic radio waves. It can measure the range of stationary targets and also the velocity for moving targets. Radars are used for a wide range of possible targets that vary from aircrafts, ships, cars, to smaller or more specific targets and purposes, such as missiles, weather formations and terrain. The word Radar is the abbreviation for **Ra**dio **D**etection **A**nd **R**anging [1]. A Radar system consists of three parts: the transmitter (Tx), the target and the receiver (Rx). A signal is transmitted from the transmitter towards the target area. A target in the target area scatters a part of the energy of the signal and absorbs the other part. A part of the scattered signal is collected from the receiver antenna and the receiver extracts the target's information from the received signal parameters. These parameters are the signal delay and the Doppler frequency of the received signal. A radar system is defined by the number of platforms used for its operation. A monostatic radar includes one transmitter and one receiver mounted on the same location. In bistatic radar the locations of the transmitter and receiver are separated apart. Also, there is the possibility of the use of multiple transmitters or receivers. In this case the radar is defined as Multi-static .

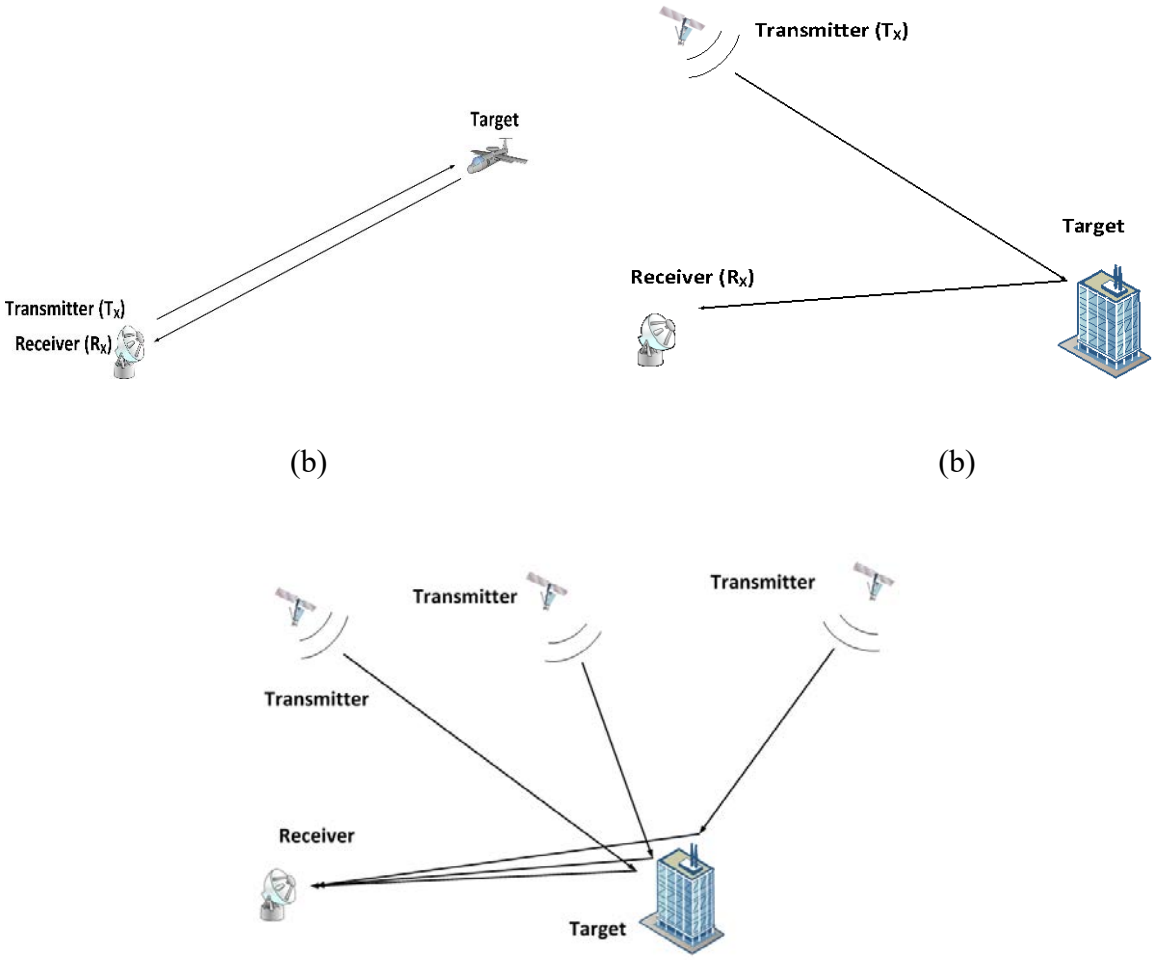

(b) (b)

(c)

Figure 1-1: General radar topologies: (a) Monostatic, (b) Bistatic, (c) Multi-static

1.1.1. Radar equation

The radar range equation (hereafter referred to as the radar equation) represents the fundamental relationship between the radar characteristics, the target and the transmitted and received signals [1], [2] and [3]. By using the fundamental range equation which has been considered in [2] and [4], the power P_r returning to the receiving antenna is expressed by:

$$P_r = \frac{P_t G_t G_r \lambda^2 \sigma}{(4\pi)^3 R_t^2 R_r^2} \tag{1.1}$$

This power depends on the initial transmitted power Pt, the transmitted and received antenna gain Gt and Gr, λ is the wavelength of the radio waves, the reflective characteristics of the target (defined as the radar-cross-section (RCS) (σ) and the range to the target R (in cases where the radar system is monostatic Rt =Rr =R and Gt = Gr). It is important to note that the equation considers bistatic radar configuration for propagation in free space. Equation (1.1) does not take into account miscellaneous losses which are always present in radar. So that in Equation (1.2) extra dimensionless factor La < 1 is used.

$$P_r = \frac{P_t G_t G_r \lambda^2 \sigma L_a}{(4\pi)^3 R_t^2 R_r^2} \tag{1.2}$$

There are two main sources of noise in the receiving system according to [4] and [5]: environmental noise received by the receiving antenna and receiving system internal noise. In the latter case the noise factor is:

$$N = kT_S B_n \tag{1.3}$$

where k is the Boltzmann constant, T_s is the system noise temperature in Kelvin and B_n is the receiver bandwidth. Following the range Equation (1.2), the theoretical maximum range can be calculated if radar parameters are known. For accurate calculation of maximum range, it is important to include in the equation the Signal-to-Noise ratio (SNR) referred to the receiving antenna input:

$$\rho = \frac{P_r}{N} = \frac{P_t G_t G_r \lambda^2 \sigma L_a}{(4\pi)^3 R_t^2 R_r^2 k T_S B_n} \tag{1.4}$$

where ρ is the signal-to-noise ratio. For desired target detection performance, ρ should be less than a certain value ρ [2]. Depending on the type of the radar two maximum range equations are shown below [2]:

- bistatic radar equation

$$(R_t R_r)_{\max} = \sqrt{\frac{P_t G_t G_r \lambda^2 \sigma L_a}{(4\pi)^3 \rho k T_S B_n}} \tag{1.5}$$

- monostatic radar equation

$$R_{\max} = \sqrt[4]{\frac{P_t G_t G_r \lambda^2 \sigma L_a}{(4\pi)^3 \rho k T_S B_n}} \tag{1.6}$$

1.1.2. Target Resolution

Target resolution is defined in the same way for monostatic and bistatic radars. The definition of the target resolution is: the degree to which two or more targets may be separated in one or more dimensions, such as angle, range, velocity (or Doppler) etc [5]. In monostatic radar, the range resolution is c/2B, where B is the signal bandwidth. In the bistatic case, the slant range resolution is taken as:

$$\Delta R = \frac{c}{2B} \cdot \frac{1}{\cos(\beta/2)} \tag{1.7}$$

where β is the bistatic angle and can be seen in Figure 1-2. During this study the bistatic configuration of Synthetic Aperture Radar (SAR) is used. The fundamentals on a Synthetic Aperture Radar can be explained better in the simplest case that is the Monostatic SAR. The Monostatic SAR is used widely and the most common configurations are the Spaceborne and Airborne configurations.

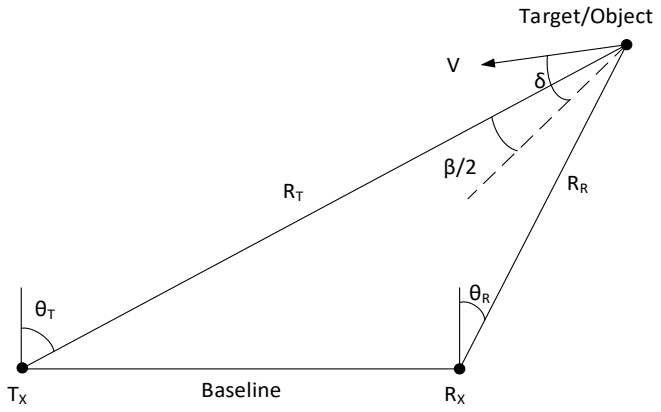

Figure 1-2: Bistatic configuration and bistatic angle

1.2. Synthetic Aperture Radar

1.2.1. Monostatic SAR

Monostatic SAR is one of the major remote sensing tools today. Only its major principles are covered here to provide a basis for comparison with the GNSS-based SAR concepts later on. For an in-depth analysis of monostatic SAR, there are a number of excellent textbooks such as [6] and [7].

Systems employing synthetic apertures seek to overcome the constraints of physical antenna arrays by moving a single antenna to different positions in an array, radiating, collecting and storing echo signals in each position (Figure 1-3). In principle, synthetic arrays may be one or

two dimensional; one dimensional arrays are commonly used and these are usually (but not necessarily) approximately linear.

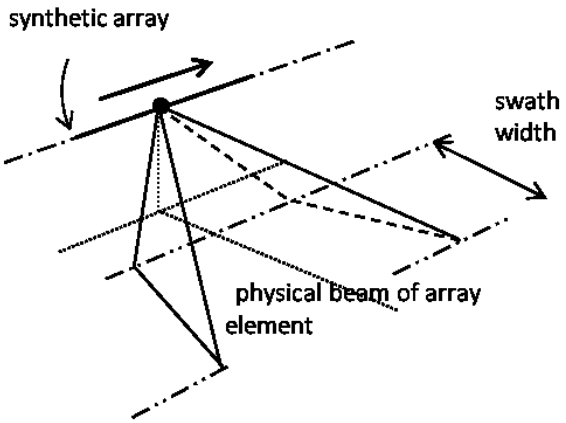

Figure 1-3: Monostatic SAR concept

Typically, an aircraft or spacecraft equipped with a terrain-mapping SAR forms a synthetic array by flying along a linear trajectory while illuminating a swath of the ground beneath it using a small antenna. In monostatic SAR, the same antenna is normally used for signal transmission and echo reception. Long linear arrays can be formed and, if the array is sufficiently long, its effective length when observing a target will depend on the beamwidth of the physical antenna (array element) and the range of the target, the effective array length being the lateral width of the physical beam at the range of interest.

As an imaging system, it is crucial to know the spatial resolution in the range and azimuth dimensions for a SAR system, as they define the size of an image pixel. “Resolution” is defined here as the minimum distance two targets should be separated by in order to appear as two returns in the radar image. For a monostatic SAR, image resolution in both range and azimuth is easy to calculate as follows. In the slant range direction, the resolution is defined by the transmitted signal bandwidth ΔF as:

$$\delta_{rm} = \frac{c}{2\Delta F} \tag{1.8}$$

where c is the speed of light. For the azimuth resolution, it can be shown [7] that it is equal to half the lateral dimension *D* of the physical antenna used for SAR image formation:

$$\delta_{am} = \frac{D}{2} \tag{1.9}$$

Equation (1.9) states that the shorter the physical antenna, the finer the azimuth resolution. This is in contrast to conventional radar, where long (i.e. narrow-beam) physical antennas are required to provide a sufficiently high angular resolution. This is because a shorter antenna implies a wider beamwidth, therefore a longer target exposure within it and a longer synthetic, rather than physical, antenna aperture length.

1.2.2. Bistatic SAR

Contrary to monostatic SAR, in bistatic SAR (BSAR) the transmitter and receiver are onboard different, spatially separated platforms. The only fundamental restriction is for at least one of the platforms to be moving, so that at least one synthetic aperture may be formed. This separation introduces an extra degree of freedom with regards to the system topology, as well as additional complexity. Despite the complexity, however, this spatial separation has opened new horizons to SAR research. For example, in terms of scientific progress, a bistatic acquisition may substantially increase the information space of monostatic SAR acquisitions by considering different target scattering angles, among other things.

A number of different BSAR topologies have been proposed on the theoretical level and/or demonstrated at the experimental level (Figure 1-4), such as: bistatic airborne SAR [8],

bistatic spaceborne SAR [9] and [10], and hybrid spaceborne/airborne bistatic SAR [11]. In any of these cases either the transmitter or the receiver could be fixed on the ground.

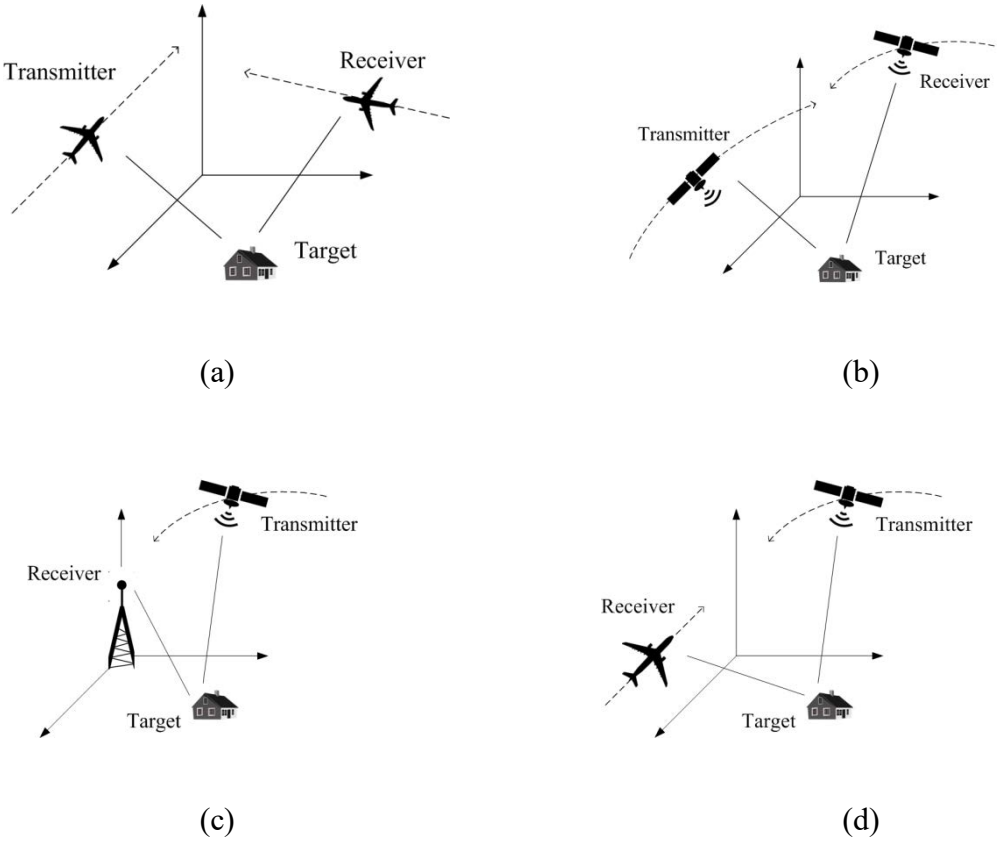

Figure 1-4: Example BSAR topologies

From this plethora of possible topologies we will focus on hybrid BSAR ((c) and (d) of Figure 1-4). Even this special topology offers a number of system configurations. The receiver can be onboard an aircraft, a ground moving vehicle or even fixed on the ground. On the other hand, the spaceborne segment can be a radar satellite or even a transmitter of opportunity. The most typical situation uses radar satellites as the illumination sources.

Perhaps the first record of a hybrid bistatic SAR experiment with a dedicated radar satellite goes back to 1998 [12]. Since then, substantial research has been conducted on this topic by a number of organisations on the theoretical and experimental levels, with [13]-[16] as some of the notable examples. Figure 1-5 [17] shows an example image obtained by the

spaceborne/stationary bistatic topology using the TerraSAR-X radar satellite as the transmitter. It is a detail of the image showing a factory 700m away from the position of the stationary receiver (Figure 1-5 a)), with the monostatic image in slant range geometry shown in Figure 1-5 b) and an optical view of the scene in Figure 1-5 c) for comparison. Results such as these confirm the fundamental feasibility of hybrid BSAR as well as the motivation for conducting BSAR research in general, since by simple observation there is a substantial difference between the monostatic and bistatic SAR images of the same scene.

a) b) c)

Figure 1-5: Bistatic vs Monostatic SAR images with hybrid SAR:

(a) Bistatic Result (Ground Range Geometry),

(b) Monostatic Image (Slant RangeGeometry) ©DLR TerraSAR-X Ground Segment,

(c) Orthophoto ©LVermA NRW (GEObasis.nrw) [17]

However, despite using dedicated radar satellites in a hybrid SAR configuration is feasible and of great scientific interest, it does suffer from a number of limitations. Perhaps unsurprisingly, these restrictions are similar to those of spaceborne SAR in general. The major limitation is that current commercial SAR cannot provide persistent area monitoring. This is limited by the small amount of satellites in any given SAR constellation and their revisit cycles, which can vary from 10 days to more than a month.

1.2.3. GNSS-based SAR

One hybrid BSAR variant uses GNSS, rather than radar satellites, as transmitters of opportunity (Figure 1-6). Any GNSS can be used, including GPS (US), GLONASS (RU), Beidou (China) and the Galileo (EU) constellations. The receiver can be stationary or mounted on a surface vehicle or an aircraft, and comprises two separate channels. The first channel records the direct satellite signal(s) for signal synchronisation purposes, a necessary process in any coherent bistatic radar (more in Chapter 2). Usually this channel is equipped with a low-gain antenna to avoid antenna pointing errors and to maximise the number of satellites that can be used. This channel will be referred to as the Heterodyne Channel (HC) hereafter. The second channel has a high-gain antenna pointed towards the observation area to record satellite signal reflections for image formation. This channel will hereafter be called the Radar Channel (RC). In the case of an airborne receiver, the synthetic aperture is essentially formed by the aircraft motion only, since the Doppler contribution due to the spacecraft motion over the dwell time on target is insignificant. In the case of a stationary receiver, the synthetic aperture is formed solely from the GNSS motion, and therefore longer data acquisitions are required to bring azimuth resolution to acceptable levels (more in Chapter 2).

While a GNSS system cannot outclass a dedicated SAR constellation in terms of image quality by default, it possesses unique properties which make it attractive for radar and remote sensing purposes. GNSS constellations possess potential for permanent and continuous monitoring of the Earth's surface anywhere in the world, including the poles. A fully operational GNSS constellation guarantees that any point on Earth is illuminated by several satellites (typically 8-11 for a single GNSS constellation) simultaneously from

different angles, and therefore the satellites at the most appropriate positions could be selected for forming the optimal bistatic topology to achieve better spatial resolutions while minimizing shadowing effects. For the same reason, multi-static or multi-perspective SAR techniques are possible, using all satellites in the field of view of the system and a single receiver. The receiver itself has an architecture similar, if not identical, to that of a GNSS receiver used for navigation, which enables a passive, low-cost operation with no additional contribution to electromagnetic pollution.

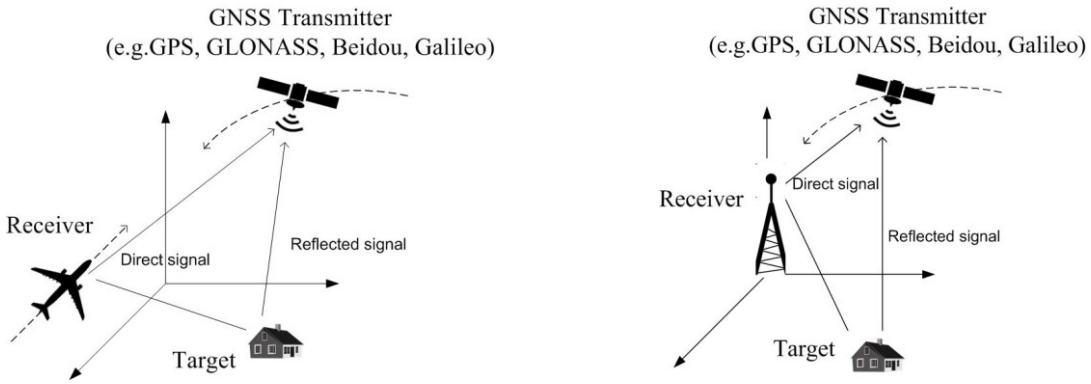

a) b)

Figure 1-6: GNSS-based SAR with a) airborne, b) fixed receiver

Apart from its unique advantages, this system also has its unique challenges. Since GNSS were not originally intended for remote sensing, their power density near the Earth's surface is substantially low. For this reason long dwell times on target are needed to increase Signal-to-Noise Ratio (SNR) via coherent integration (Chapter 2), however even in that case the system is more suited to local area monitoring. In terms of signal processing, signal synchronisation differs to that of traditional passive radar. Furthermore, the asymmetric structure of the system restricts the types of image formation algorithms that can be used.

1.3. Foundation work

Over the last years, the Microwave Integrated Systems Laboratory (MISL) has acquired high experience in remote sensing technology. One of the fields of work and study is also bistatic SAR. Since GNSS signals are transmitted already, the needed equipment is a receiver for receiving these signals and decoding algorithms to decode and process the received data. At the beginning of the current study, a receiver system was developed. The receiver system consists of the hardware and the software for the acquisitions. The hardware is University of Birmingham made and the software/scripts for the data acquisition are also produced from the same group (MISL). The receiver is a Super Heterodyne receiver (two intermediate frequencies) which one of the intermediate frequencies is tuneable to cover all GNSSs. The receiver consists of 3 RF channels as input (in this study only two of which are used) and the output is in digital form through an express card to the computer.

Figure 1-7: GNSS-based SAR receiver

The main function of Super Heterodyne receiver module is to amplify the received signal, then to convert it to intermediate frequencies (2) and to pass it to the band pass filter (BPF). The receiver is used for separating and removing the carrier frequency from the modulated

target return signal. Next step in the receiver box is to pass the signal trough an analog-to-digital convertor (ADC) which will allow data to be analysed by signal processor. In former radar systems the received data is presented on displays/indicators and analysis and target recognition is performed by human operators. In modern radars automatic target detection and tracking (ATDT) and air traffic control (ATC) are performed by computer system but still display targets for human recognition.

Despite the fact that radars have evolved so much during the past few decades, still one of the most important characteristics of radar is its ability to measure distance. The simplest way to express the range to a detected object is by taking into account the time, that is needed for a EM wave to propagate from the transmitter, reflect from the target and get back to the receiver unit. This relationship is expressed by Equation (1.1) [1], [9], [11]:

$$\mathrm{R} = \frac{c\Delta T}{2} \tag{1.10}$$

where c is the speed of light (c = 3.108 m/s) and ΔT is the round-trip time delay.

The output data are in bit form, and they are the samples for the I and Q outputs for each RF channel. The signals I and Q for each RF channels are in baseband frequency. The sampling frequency is set at 50 MHz when 2 RF channels are used. In the case of the operation to all 3 RF channels the sampling frequency is set to 25 MHz because the amount of data to be stored is enormous for the computer to handle. Another advantage of the receiver is the ability to work for hours with the use of a set of 2 car batteries.

The University of Birmingham (UOB) has done an extensive work in the area of SS-BSAR with GNSS, both on analytical and experimental level. The previous work concentrated on fundamental radar performance analysis and signal processing in moving receiver case. The ambiguity function and resolution analysis of such a system were examined in [19],[20]. The power budget and interference level evaluation could be found in [21],[22]. Interferometric applicability [23] and surface change detection [24] were studied. The image algorithm modified for SS-BSAR with GNSS could be referred to [25]-[27] where three different configurations have been considered, namely: SS-BSAR with stationary receiver, with parallel transmitter-to-receiver trajectory (different velocities), and generalized SS-BSAR. Signal synchronization algorithm could be found in [30],[31]. [32],[33] summarize the work.

1.4. Problems statement and contribution

The existing knowledge and equipment mentioned above are the state of the art in the beginning of my Ph.D. studies. They can be summarized as:

a) A GNSS receiver with proven GNSS-based SAR imaging capabilities
b) Signal processing and image formation algorithms
c) Coherent Change Detection models for monostatic SAR
d) Spatial decorrelation model for GNSS-based SAR

A study on temporal decorrelation in GNSS-based SAR completes the missing part for a Coherent Change Detection model for bistatic SAR.

The aim of this thesis is to explore whether or not it is fundamentally possible to use GNSS-based SAR imagery to detect temporal changes, i.e. displacements, in a scene. This study uses existing work on GNSS-based SAR image formation and interpretation as the stepping

stone to investigate whether a series of such images can be processed to reveal scene changes, and how this may be achieved in practice with real GNSS-based SAR images.

To understand whether the above is plausible, and as the first comprehensive study in this area, this thesis considers a Coherent Change Detection (CCD) scheme. In this scheme, multiple, temporally separated images can be compared at the phase level. The complex temporal de-correlation coefficient between consecutive images can then be used to estimate the amount of physical target displacements. CCD is not the most advanced technique for change detection in SAR, however CCD is used here as a means of confirming the system's fundamental capability in monitoring scene changes. In addition, while from an algorithmic point of view CCD is well-known for monostatic SAR, its application to a bistatic SAR with as highly an asymmetric structure as GNSS-based SAR is unknown. The results of this thesis contribute to the understanding of the bistatic SAR, where the transmitter is any GNSS satellite.

To address the fundamental challenges of this research, this thesis proposes a proof-of-concept theoretical and experimental research study. The work done by myself, with the guidance of my supervisor, and my contribution to GNSS-based SAR include:

e) A model of temporal de-correlation effects in GNSS-based SAR and its relationship to scene displacements
f) The development of a CCD algorithm for GNSS-based SAR images
g) The design and execution of a proof-of-concept experimental campaign to confirm the feasibility of GNSS-based SAR change detection
h) A comparison between theoretical and experimental results to confirm the validity of theoretical models

1.5. Thesis outline

Chapter 2 focuses on the GNSSs available for use and their specifications. Frequency allocations and power budget analysis are presented. The receiver system is also explained. In Chapter 3 the coherent change detection analysis is described and the processing of the acquired images is explained. Chapter 4 focuses on the experimental program description and a part of the data analysis is presented. The stages of processing as analysed and expected results are explained. Then, in Chapter 5 the coherent change detection results and the data processing analysis are shown. Coherence levels are calculated and decorrelation outputs and presented. The conclusions of the thesis will be presented in the Chapter 6 along with the future work.

Chapter 2 GNSS-based SAR System Overview

2.1. Introduction

In this chapter, the GNSS-based SAR system overview is presented. As every radar or communication's system consists of the two major parts, the transmitter and the receiver, the same principle is used in the system used in this study. First an overview of the GNSSs and the specifications of which will be given. Signal bandwidths and signal properties for each system will be presented and explained. Also, the receiver system explanation will follow. Configuration and inputs will be explained and output data use will be presented. The output data and the way of processing to create the output image follows. The last part of this chapter focuses on the resolution analysis of the system and the image production and characteristics conclude the chapter.

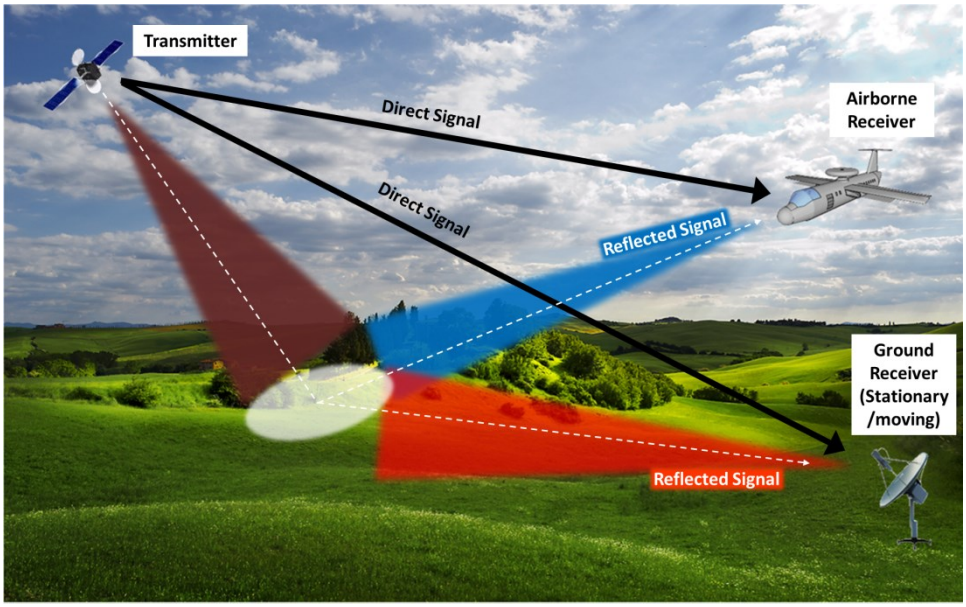

Figure 2-1: GNSS-based SAR system

2.2. GNSS Constellations

Out of the four available GNSS constellations, two of them are currently in full operation. These are the Global Positioning System (GPS) and the Global Navigation Satellite System (GLONASS). The other two, Galileo and BeiDou, are still on the deployment stage and scheduled to reach their full operational capacity in 2019 and 2020 respectively. For all four GNSS, their system characteristics are published in detail under their respective interface control documents (ICDs), which are available online [35]-[38].

Global Navigation satellites continuously transmit navigation signals in multiple frequencies bands within the L band. From the radar user's perspective, these signals contain ranging codes which can be used for remote sensing, as well as navigation codes which can additionally be used for positioning. For example, in GPS, Figure 2-2 shows the available GNSS frequency bands [36]. Note the "SAR" acronym in the figure refers to Galileo's Search And Rescue service. An overview of some most popular GNSS signals and their generic structure is provided below.

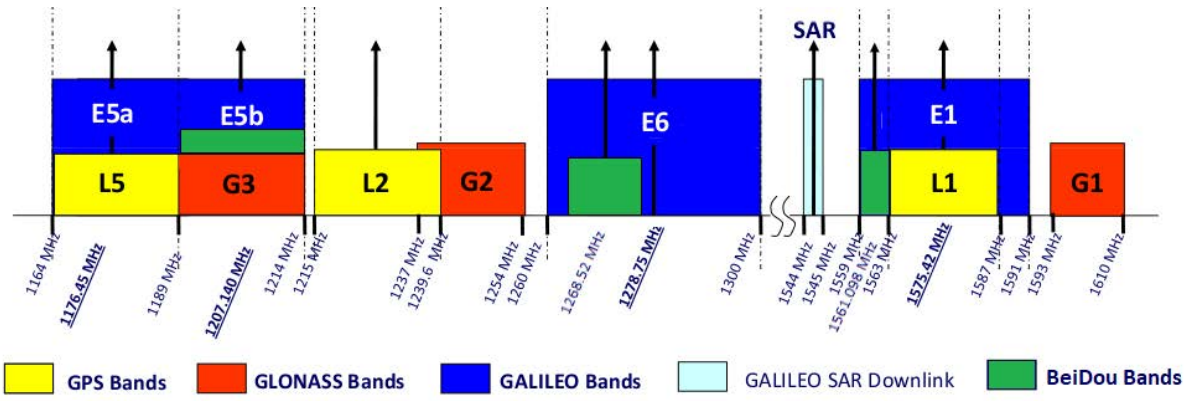

Figure 2-2: GNSS navigation frequency bands [36]

Although several signals are transmitted in the same band, and often with the same carrier frequency, they are received and decoded because they are using different ranging codes. The ranging codes are generated with shift registers and they are repeated periodically. They are also known as pseudorandom noise (PRN) and in Code Divided Multiple Access systems, each satellite/transmitter is using a different ranging code that identifies it (GPS, Galileo). However in GLONASS, the ranging code is the same for all satellites, as the signal from each satellite is using different carrier frequency.

An example of a ranging code is the pseudorandom (PR) sequence used in all GLONASS satellites [35]. PR ranging code is a sequence of maximum length of shift register with a period 1 millisecond and bit rate 511 kbps. PR ranging code is sampled at the output of 7^{th} stage of the 9-stage shift register. The initialization vector to generate this sequence is (111111111). The first character of the PR ranging code is the first character in the group 111111100, and it is repeated every 1 millisecond. The generating polynomial, which corresponds to the 9-stage shift register (see Figure 2-3: Structure of shift register used for ranging code generation [35]Figure 2-3), is

$$G(x) = 1 + x^3 + x^9 \tag{2.1}$$

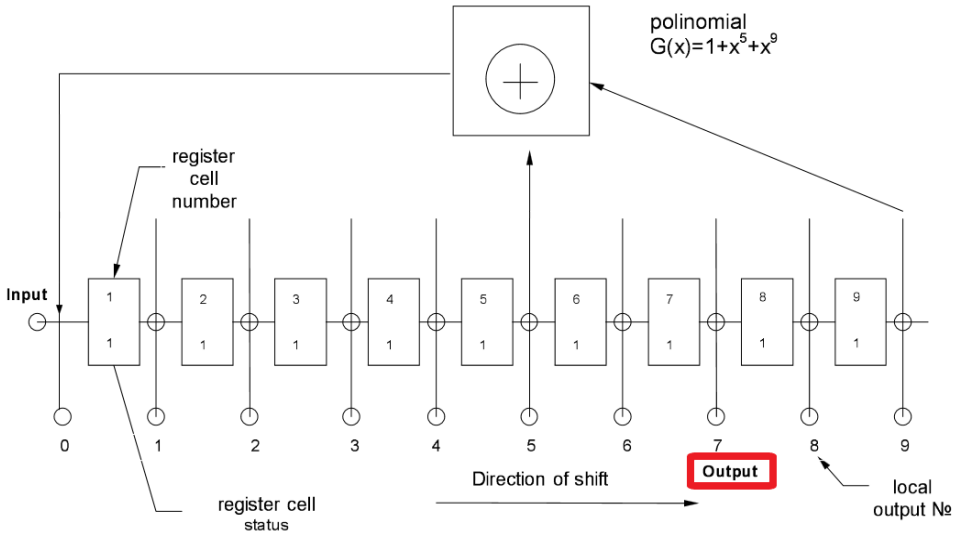

Figure 2-3: Structure of shift register used for ranging code generation [35]

2.2.1. GPS Constellation

GPS has three dedicated frequency bands, L1 (carrier frequency at 1575.42 MHz), L2 (carrier frequency at 1227.60 MHz), and the new frequency band L5 (carrier frequency at 1176.45 MHz). The satellites in L1 band transmit two ranging codes- the Coarse Acquisition (C/A) and/or the Precision (P) code, where the satellites operating in the L2 band transmit only the P-code. Both the C/A- and the P-codes are binary sequence codes with the C/A-code to be names as Gold (from Robert Gold). The GPS L5 signal is modulated by two codes, L5-I and L5-Q, that are in phase quadrature for the L5 data and L5 pilot channels respectively. Satellite codes are uniquely identified by a Code Division Multiple Access (CDMA) protocol, meaning that different satellites transmit different codes, whose generation methods are listed in the GPS ICD [37]. The C/A-code on L1 is also referred to as the “legacy” signal and is broadcast by all satellites. This code is transmitted using Binary Phase Shift Keying (BPSK), as shown in Figure 2-4.

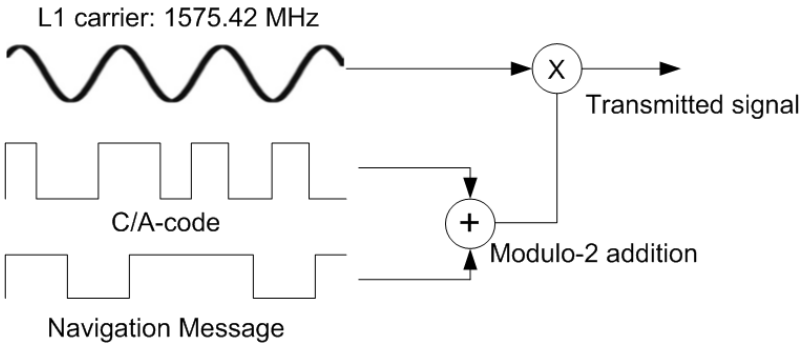

Figure 2-4: GPS legacy signal structure [37]

2.2.2. GLONASS Constellation

Similarly, two GLONASS bands are shown as G1 and G2 in Figure 2-2. Their nominal center frequencies are 1602 MHz and 1246 MHz, respectively. Like GPS, both C/A- and/or P-codes are transmitted in these bands, with a signal structure almost identical to that shown in Figure 2-4. Also similar to GPS, GLONASS ranging codes are pseudo-random sequences. Unlike GPS, different satellites are uniquely identified by transmitting at a carrier frequency that is slightly offset from the nominal G1 and G2 values, i.e. GLONASS operates on a Frequency Division Multiple Access (FDMA) protocol. The frequency for each satellite at the G1 and G2 bands is given by [35]

$$f_{K1} = f_{01} + K\Delta f_1 \tag{2.2}$$

$$f_{K2} = f_{02} + K\Delta f_2 \tag{2.3}$$

where K is a frequency index, f_{01} and f_{02} are the G1 and G2 nominal frequencies, Δf_1 and Δf_2 are the frequency spacings for the G1 and G2 bands that are equal to 562.5 kHz and

437.5 kHz, respectively. A new frequency band, G3, has been proposed and is planned as part of the new GLONASS satellites from 2018.

2.2.3. Galileo Constellation

Even though Galileo is not yet fully deployed, perhaps one of its most interesting frequency bands is the E5 band. That is due to its Alternative Binary Offset Carrier (AltBOC) type of modulation [38] that substantially differs from legacy GPS and GLONASS signal structure. The E5 band consists of two sub-bands, namely E5a and E5b, εαψη centred 15.345 MHz to the sides of the E5 carrier at 1191.795 MHz (Figure 2-5). However, the two sub-carriers for E5a and E5b are actually generated as digital bit streams. Furthermore, in each sub-band there are two primary codes based on a CDMA protocol which are transmitted in phase quadrature (E5a-I/Q, E5b-I/Q), and with each primary code comes a secondary code. The E5 signal structure is shown in Figure 2-6 [40].

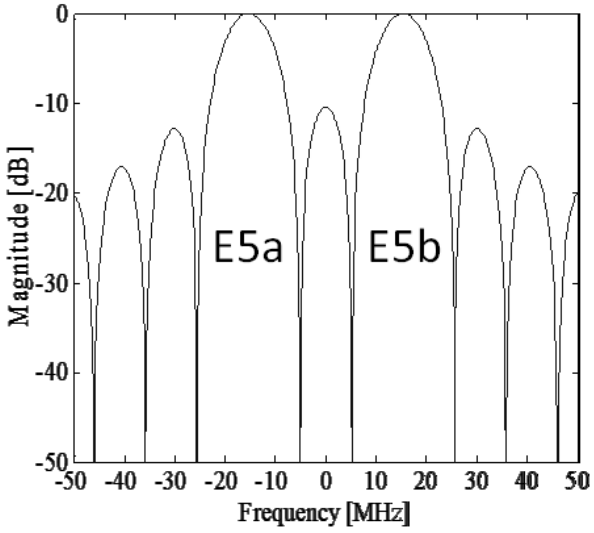

Figure 2-5: Power spectral density of E5 signal

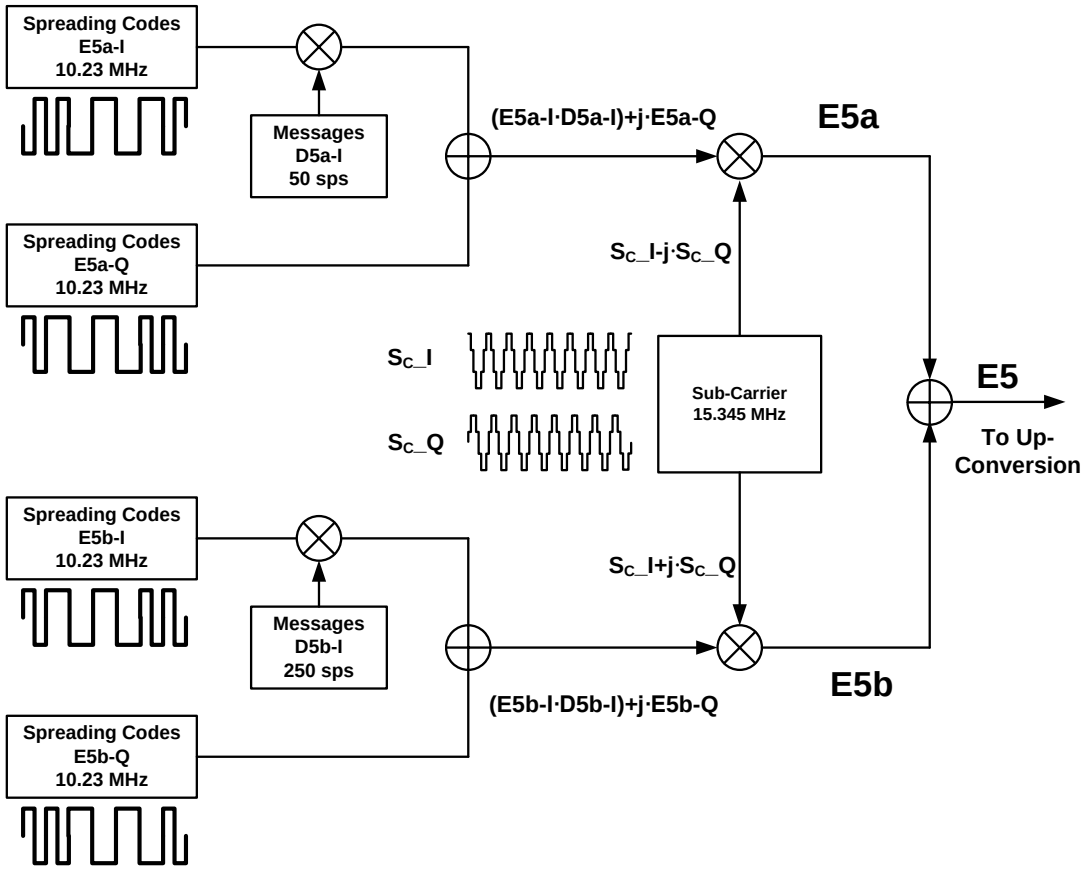

Figure 2-6: E5 signal structure

In choosing appropriate GNSS signals for passive radar applications, the ranging signal bandwidths and their time durations are of significant importance, as well as their complexity. That is because signal time delay is with respect to the start of the code, and the ranging signal bandwidth is directly related to range resolution as shown in equation (1.8). Table 2-1 shows the major characteristics for the signals described above.

Table 2-1: GNSS major signal characteristics

Signal	Code duration	Bandwidth (MHz)	Navigation Message/ Data rate
GPS C/A-code (L1)	1ms	1.023 MHz	Yes/50 bits/s
GPS P-code (L1/L2)	7 days	10.23 MHz	Yes/50 bits/s
GPS L5-I	1ms	10.23 MHz	Yes/50 bits/s
L5-Q (L5)	1ms	10.23 MHz	No
GLONASS C/A-code (G1/G2)	1ms	0.511 MHz	Yes/50 bits/s
GLONASS P-code (G1/G2)	1s	5.11 MHz	Yes/50 bits/s
Galileo E5a-I	1ms	10.23 MHz	Yes/ 50 symbols/s
Galileo E5b-I	1ms	10.23 MHz	Yes/ 250 symbols/s
Galileo E5a-Q/E5b-Q	1ms	10.23 MHz	No

From the table, GPS P-code is already inappropriate due to its duration of 7 days. GPS C/A-code is of a sufficiently short duration, but from equation (1.8) its bandwidth yields a range resolution of approximately 147m, that is too coarse for imaging purposes. That rules out the use of GPS L1 and L2 for passive SAR. However the introduction of GPS L5 band, fully overlapping with Galileo's E5a band, shows great potential. With regards to GLONASS, the P-code is usable, its details having been published in [39]. This is the signal that has been used for GNSS-based SAR in the last years by the Microwave Integrated Systems Laboratory of the University of Birmingham. The most promising signals in this group are the Q-components of Galileo E5. Not only their durations and bandwidths (14.7m resolution) are acceptable, but also they lack of navigation message data which makes their signal processing

simpler. However, for Galileo only a handful of satellites were in operation during this study. This thesis considers GLONASS satellites as the transmitter. The processes described, on the other hand, are applicable to any GNSS transmitter, theoretically.

2.3. GNSS Signal Power

In order to derive the GNSS-based SAR power budget, the power flux density of GNSS signals near the Earth's surface is required. The power flux density over 1m^2 surface area, the entire signal bandwidth, may be calculated in dB($\frac{W}{m^2}$) via

$$\rho = \frac{EIRP}{4\pi R_T^2} \tag{2.4}$$

where EIRP is the Effective Isotropic Radiated Power of the satellite and R_T is the range from the satellite to the Earth's surface. Note that GNSS are designed to have an almost constant power flux density over their overall antenna beam coverage. What is also often quoted in the GNSS community is the guaranteed minimum power levels near the Earth's surface. They are given as signal power levels at the output of a linear or circularly polarised low-gain antenna, including some atmospheric attenuation and assuming the satellite is at least 5^o over the horizon. The power flux density and the minimum received power levels (obtained from [35], [37], [38]) are listed in Table 2-2. The power flux density is calculated via (2.4), taking R_T as the satellite orbital altitude for simplicity (R_T in general varies with the relative position between the satellite and the surface). GPS, GLONASS and Galileo systems generate more or less same power flux density, with Galileo having 4 dB higher minimum received power level than GLONASS.

Table 2-2: GNSS power flux densities and minimum received power levels

Transmitter	Power output (W)	EIRP (dBW)	Orbit Altitude (km)	Power Density (dBW/m^2)	Minimum power level (dBW)
Galileo E5a/b	50	32	23222	-126	-157
GPS L1	50	30	20180	-127	-158
GLONASS L1	50	28	19130	-128	-161

Now that the specifications of GNSS signals and their power levels are presented, a study for the power budget for SAR with the use of GNSS as transmitters follows.

2.4. Power budget for GNSS-based SAR

The study of the power budget is done for the receiver end. The receiver records two signals via two separate channels, heterodyne and radar channels. The heterodyne channel (HC) records the direct satellite-receiver signal for signal synchronization, while the radar channel (RC) records satellite signal reflections from an observation area.

The power received at the output of the HC antenna is given by:

$$P_{HC} = \rho A_{eH} \tag{2.5}$$

where A_{eH} is the effective area of the HC antenna. For a 6 dB low-gain antenna, that is typical for GNSS antennas used for navigation, A_{eH} is approximately $0.013m^2$ at the GNSS frequency bands. Using values for ρ from Table 2-2 the received power for Galileo signals is approximately 3.265×10^{-15} W and for the GLONASS used in this study it is approximately 2.06×10^{-15} W.

The signal is received at the background of receiver thermal noise, whose power is

$$P_N = kT_s\Delta F \tag{2.6}$$

where k is Boltzmann's constant, T_s is the operating temperature, in Kelvins and ΔF is the signal bandwidth. An SNR prior to any signal processing is the ratio of the received power to the noise power, hence

$$SNR = \frac{P_{HC}}{P_N} \tag{2.7}$$

Assuming the receiver operates at room temperature (290 K), and the system bandwidth is equal to that of Galileo E5a band, SNR at the receiver output is approximately equal to -11 dB, where it is -10 dB for the GLONASS, i.e. the direct signal is buried under the noise and therefore cannot be used for signal synchronisation. However, using a matched filter SNR can be substantially improved. For a phase-coded waveform such as a GNSS signal, it can be shown that SNR at the matched filter output is equal to:

$$SNR_{MF} = SNR \times T_p \times \Delta F \tag{2.8}$$

where T_p is the ranging code duration. For Galileo E5a/E5b $T_p = 1$ ms and $\Delta F = 10.23$ MHz, whereas for GLONASS-L1 P-code $T_p = 1$ ms and $\Delta F = 5.11$ MHz, a matched filter gives an SNR improvement of about 40 dB and 37 dB respectively. This is why signal synchronisation is based on matched filtering techniques.

For the RC, calculations are more complex. Following the analysis in [22] and assuming free space propagation, SNR at the output of SAR image formation processor may be written as:

$$SNR_{RC} = \rho \times \frac{\sigma A_{eR}}{4\pi R_R^2} \times T_p \Delta F \times T_D PRF \times \frac{1}{kT_s \Delta F} \tag{2.9}$$

where σ is the bistatic Radar Cross-Section, A_{eR} is the effective area of the RC antenna, R_R is the receiver-target range, T_D is the dwell time on target, and PRF is the pulse repetition frequency along the synthetic aperture.

The first factor, ρ, in equation (2.9) is the power flux density near the Earth's surface, which can be taken as a constant for a given observation area. The third factor, $T_p \Delta F$, is the signal processing gain due to matched filtering in range, which is identical to the matched filter operation described in (2.8). The fourth factor, $T_D PRF$ is the signal processing gain obtained after azimuth signal processing. Note the product of the total dwell time on target with the PRF equals to the amount of pulses, *N*, transmitted over the full aperture. This is assuming that the target RCS remains constant over the dwell time. Hence azimuth processing is an equivalent of coherent summation of all transmitted pulses.

Equation (2.9) can be further simplified by assuming the receiver bandwidth (used for receiver noise calculations) is equal to the ranging signal bandwidth. Moreover, the total pulse duration is usually taken as the Pulse Repetition Interval (PRI) in this case, so $T_p \times PRF = 1$. Therefore equation (2.9) takes its final form as:

$$SNR_{RC} = \rho \times \frac{\sigma A_{eR}}{4\pi R_R^2} \times \frac{1}{kT_s} \times T_D \tag{2.10}$$

Equation (2.10) indicates that SNR for GNSS-based SAR may be substantially increased by increasing the dwell time on target. The same expression is valid for both the airborne and ground-fixed receiver configurations. The only difference lies in the practicalities of these two options. For a stationary receiver setup, the dwell time on target may be from the order of minutes to hours, since GNSS transmitters are visible above an area for long intervals while

the receiver's antenna is constantly pointed at the area of interest. Typically an integration of several minutes (5 or more) is sufficient to obtain a sufficient SNR and azimuth resolution. Note that this is in contrast to spaceborne SAR, where dwell times on target may be fractions of a second. Table 2-3 shows SNR obtained for a fixed receiver, for different target RCS's and at different distances. Table entries have been calculated using equation (2.10), assuming a receiving antenna gain of 15 dB and additionally 3 dB system losses with a receiver noise figure of 1.5 dB. The transmitter is assumed to be Galileo, however similar values can be found for GPS and GLONASS simply by subtracting their difference in the power flux density, listed in Table 2-2.

Table 2-3: Example SNRs for stationary receiver

RCS (m^2)	10	10	50	250	250
Distance receiver-target (km)	3	5	5	10	15
Dwell time on target (s)	300	1000	300	1000	1000
Signal-to-noise (Power ratio-dB)	17	18	20	26	22.5

Setting a SNR of 12 dB as the target detection threshold, it shows that GNSS-based SAR operational ranges are in the order of a few kms. That is the reason why GNSS-based SAR is more attractive for the persistent monitoring of local areas.

For a ground stationary receiver, the power budget is more favourable since the dwell time on target can be substantial. For an airborne receiver, the dwell time on target and hence its power budget are restricted by the RC antenna beamwidths and the aircraft speed. To illustrate this, (2.10) may be slightly re-arranged by re-writing T_D as

$$T_D = \frac{2R_R tan(\theta/2)}{V_a} \tag{2.11}$$

where V_a is the aircraft speed and θ is the RC antenna beamwidth, equal to λ/D where D is the along-track physical dimension of the RC antenna. Combining equation (2.10)

$$SNR_{RC} = \rho \times \frac{\sigma A_{eR}}{4\pi R_R^2} \times \frac{1}{kT_s} \times T_D$$

and (2.11), with D= 1m and V_a = 100m/s, that may be towards the speed upper limit for a practical detection range, Table 2-4 shows example SNRs for the airborne receiver case.

Table 2-4: Example SNRs for airborne receiver

RCS (m^2)	10	50	50	100	100	250
Distance receiver-target (km)	1	1	2	2	4	5
Dwell time on target (s)	9.6	9.6	19	19	38	47.6
Signal-to-noise (Power ratio-dB)	12	19	16	19	16	19

The analysis introduced above does not include other ways of further power budget improvement. For example, SNR can be further improved essentially by using non-coherent integration of signals from more than one transmitting channel and/or more than one satellite.

2.5. Receiver equipment

The receiver equipment consists of a superhererodyne receiver and multiple antennas. Although the receiver comprises three antenna inputs (3 RF input channels), for the applications studied in this thesis only two were needed. All three channels are identical, and they are split in three stages: a) radio frequency, b) intermediate frequency and c) baseband.

The RF stage consists of a 35dB gain amplifier followed by a mixer. Mixing the RF with the output of a frequency synthesizer the RF signal is down-converted to the IF band. The frequency synthesizer at this stage is tuneable and can be adjusted to the carrier frequency of any GNSS constellation. Going to the IF stage the signal, now in IF band, is filtered and amplified with having 100dB gain amplifiers. Last is the baseband stage, and it is reached with the use of a second frequency synthesizer. This frequency synthesizer has a fixed output frequency and it is set at 140 MHz. In order to preserve the coherence in the down-conversion both frequency synthesizers use the same reference clock. Also, at the baseband stage the quadrature demodulation is performed. The quadrature outputs are then digitized through an Analog-to-Digital Converter (ADC). The digital outputs are stored to a PC with a sampling frequency of 50MHz. For the current computer used for the data storage, when all 3 RF channels are is use simultaneously the sampling frequency is decreased to 25MHz. In this way the processing of all signals is done offline. A block diagram of the receiver is given in Figure 2-7.

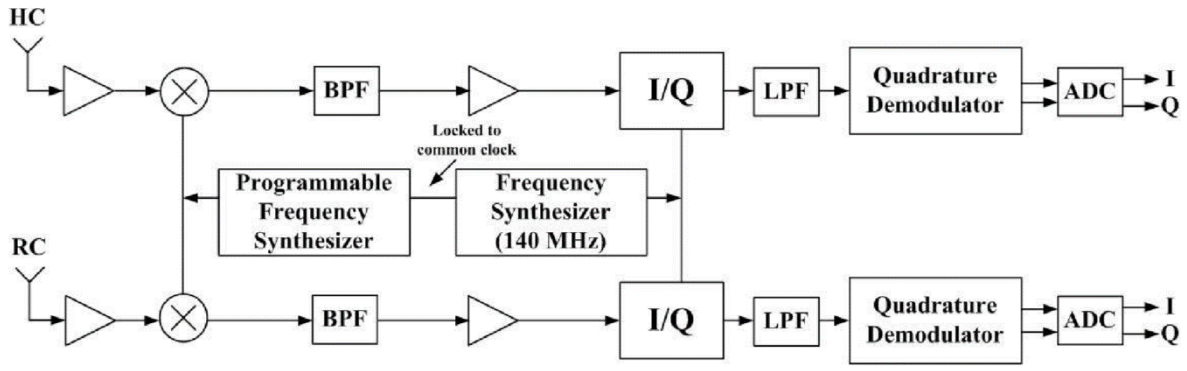

Figure 2-7: Block diagram of receiver

Figure 2-8: Photograph of receiver from outside

As mentioned, the receiver consists of three channels, and in the figure above we can see the quadrature outputs, I and Q for each channel. Those are connected to the ADC for sampling and with the use of a PCI-express card the data is saved on the computer. Two channels are used for most of the experiments. The third RF channel can be used for interferometric studies and applications. For any non-interferometric experiment, two channels are used. The two channels are named as Heterodyne Channel (HC) and Radar Channel (RC). The heterodyne channel is used for the collection of the direct signal from the satellite, whereas the radar channel is used for the reflected satellite signal from targets. For each channel an antenna is needed for the collection of the signals. For the HC signal a low-gain antenna is used, since we are interested in the direct satellite signal. Here there are two options on the antenna to be used, a) a patch antenna made by University of Birmingham – MISL or b) a TOPCON GNSS antenna (CR-G5). The gain of the patch antenna is 5dBi and the beamwidth covers a cone of 60 degrees. Equivalent specifications apply to the TOPCON antenna. The broad beamwidth of the antennas ensures that the satellite remains in the view during the

whole dwell time. For the RC signal, a helical antenna is used with a gain 16dBi for main-lobe and its -3dB beam width covers a cone of 30 degrees to the direction of the antenna.

(a) (b) (c)

Figure 2-9: Receiver antennas (a)TOPCON, (b) UoB patch and (c) helical

2.6. GNSS Signal synchronization

The spatial separation between the transmitter and the receiver in bistatic radar creates the need of synchronization. Timing and local oscillator differences between the transmitter and the receiver systems are the factors that are not as easily solved as in monostatic radar. Thus, the synchronization is an essential part for the signal collection and the processing afterwards in bistatic radar. In GNSS-based SAR, the synchronization is even more crucial as the received signal has very low power. With the term synchronization we refer to the direct signal tracking.

The direct signal power is not high enough to be used as it is for reference, as it has been presented before. The SNR at the input of the receiver can be as low as -20 to -30 dB, and this makes the synchronization process necessary for the signal parameters extraction. Another reason for the signal synchronization is that GNSS signals consist of three sequences (Primary code, secondary code, Navigation message) and not all of them are needed for

imaging. In most cases it is just the primary code that is needed. The signal synchronization for GNSS-based SAR is formed by modifying the signal processing algorithms that are used for positioning and navigation purposes. Positioning and navigation devices need to cancel out the ranging codes and isolate the navigation message. But in order to do so, they need to track the delay, Doppler and phase of the ranging codes. The same principals can be used to track direct signal parameters for an imaging GNSS-based SAR as this one. The algorithm for the signal synchronization hat is created from the block adjustment of synchronizing signals (BASS),[41], is shown in the block diagram in Figure 2-10.

Figure 2-10: BASS-based algorithm for signal synchronization

The generic form of a transmitted GNSS signal is:

$$\begin{aligned} Y(t) = {} & P(t)M_P(t)\cos(\omega_c t + \varphi) \\ & + D(t)M_D(t)\sin(\omega_c t + \varphi) \end{aligned} \tag{2.12}$$

where t is time, $P(t)$ and $D(t)$ are the primary and secondary GNSS ranging code envelopes, $M_p(t)$ and $M_D(t)$ are the associated navigation messages, ω_c is the signal carrier frequency and φ is the initial phase.

The primary and secondary ranging codes have different code rates, with the primary to be the high precision one. Thus the primary codeis the one that is needed for the image formation. In order to extract the tracking outputs for the primary code, the secondary code modulation needs to be removed from the equation (2.12). Let us explain the received direct signal at the HC of the receiver (after quadrature demodulation) that is as:

$$\begin{aligned} s(t_n,u) = P\left[t_n - \tau_{dP}(u)\right] M_P\left[t_n - \tau_{dP}(u)\right] \exp\left[j\left(\omega_d(u)t_n + \varphi_{dP}(u)\right)\right] \\ + j \times D\left[t_n - \tau_{dD}(u)\right] M_D\left[t_n - \tau_{dD}(u)\right] \exp\left[j\left(\omega_d(u)t_n + \varphi_{dD}(u)\right)\right] \end{aligned} \quad (2.13)$$

where $t_n \in [0, PRI]$ denotes fast-time and PRI is the pulse repetition interval, $u \in [-T/2, T/2]$ is slow-time and T is the dwell time, and $\tau_{dP/D}(u)$, $\omega_d(u)$ and $\varphi_{dP/D}(u)$ are the instantaneous direct signal time delay, Doppler shift and initial phase associated with each code, respectively, all of which are varying with slow-time. We can observe here that, although the time delay and phase of primary and secondary codes are different by a constant (due to structure and length), the Doppler is the same (considering that Doppler is defined as the derivative of the phase). Since the information needed for image formation is the primary code, the tracking is done for the secondary code first.

The first stage in the algorithm (Figure 2-10: BASS-based algorithm for signal synchronizationFigure 2-10) combines the delay $\tau_{dD}(u)$ and coarse Doppler frequency tracking of the secondary code. These parameters are provided at every PRI, which for GNSS is usually 1 ms, resulting in a pulse repetition frequency (PRF) of 1 kHz. The tracking process consists of a bank of matched filters and it is a 2D search algorithm in delay and Doppler. A locally generated replica of *D(t)* is created and it is modulated with Doppler frequencies for the Doppler search. The envelope of each matched filter is formed with the

replica and a modulation of Doppler frequency that has the step of the PRF (1 kHz) and covers frequencies between -20 and +20 kHz. The step is rather big and this is why this stage is categorised as coarse frequency. Also, the |20 kHz| value is the maximum Doppler expected from a GNSS satellite with stationary receiver [41]. On the delay part, it is referred to the time difference between the start of the secondary code of the replica and the start of the secondary code in the currently processed PRI (msec). Thus, the time delay has values between 0 and PRI (1 msec) with a step that depends on the sampling frequency of the system and it is *1/fs* , where *fs* represents the sampling frequency. Figure 2-11 presents the processing steps for a single Doppler frequency and Figure 2-12 shows a typical 2D delay/coarse frequency estimate for one PRI, obtained from experimental data acquired at one of the experiments conducted for the Coherent Change Detection study that is explained later in the thesis. The location of the peak indicates the estimated delay and coarse frequency.

Experimental confirmation and produced outputs are presented in the next paragraph using a GLONASS satellite. In the signal tracking, the secondary code is the GLONASS C/A-code and the primary code is the GLONASS P-code.

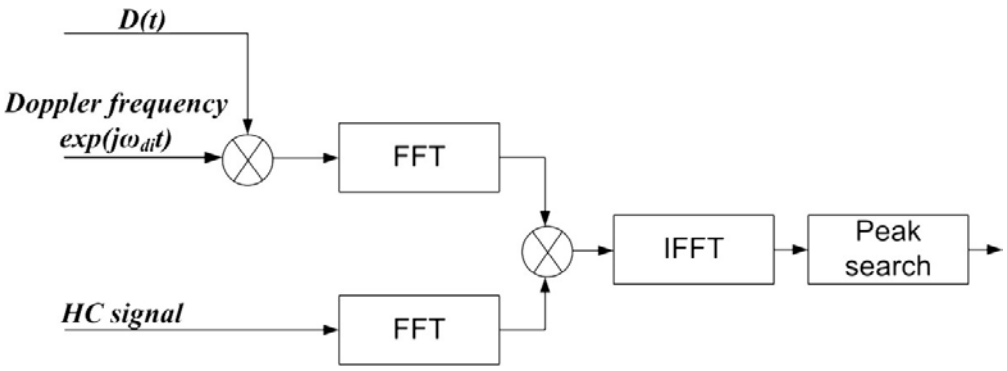

Figure 2-11: Delay/coarse frequency tracking block diagram [42]

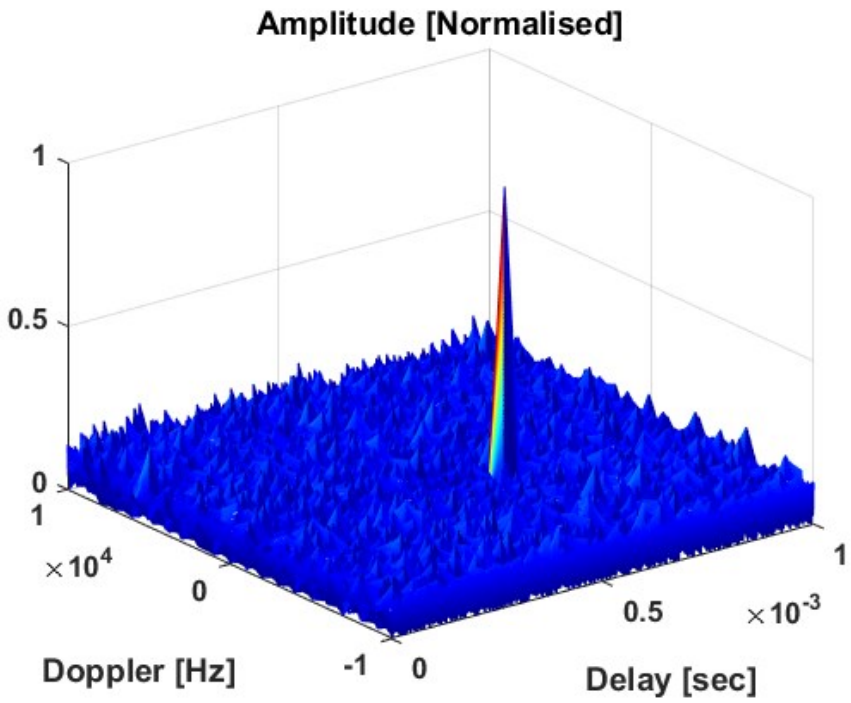

Figure 2-12: Output of delay/coarse frequency tracker for 1-ms data.

The tracking process continues with the medium and fine frequency tracking. The medium frequency tracking works in similar way to the coarse frequency with the difference that the Doppler estimation is calculated with 200 Hz resolution. The fast Fourier transform (FFT) processing provides satisfactory levels of Doppler estimation. However, the fine frequency tracking operates on the phase difference between signals at adjacent PRIs, where Doppler tracking has an accuracy of up to two decimal places in practice. In order to do so, there should be no phase transitions due to the secondary code. Thus, the removal of the secondary code modulation is essential and is done by stripping the $D[t_n - t_{dD}(u)]$ from the data. A graphical representation of the removal of the secondary code is shown in the following figure.

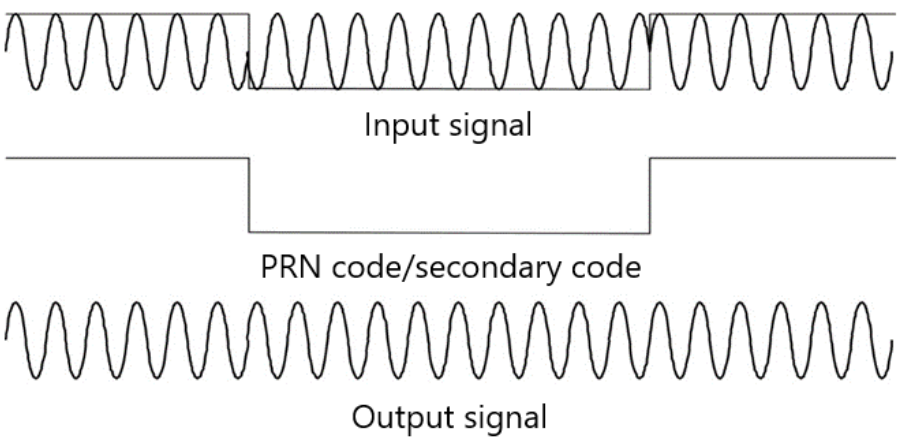

Figure 2-13: Removing GNSS signal from code [42]

After the fine frequency tracking process is done, the Doppler shift of the direct signal $\omega_d(u)$ has been estimated for the secondary code, but also for the primary code since the Doppler is assumed to be the same for primary and secondary code as shown in the equation (2.13).

With the fine frequency estimation the tracking of the secondary code is done and the time delay and Doppler of the secondary code are known. Thus, the secondary code can be removed from (2.13). Although the navigation message $M_D(t)$ has not been tracked, it can be considered as a random signal with low cross-correlation level with the primary, and therefore can be neglected. Removing the secondary code part from equation (2.13), we get the remaining received signal to be as:

$$s(t_n,u) = P\left[t_n - \tau_{dP}(u)\right] \cdot M_P\left[t_n - \tau_{dP}(u)\right] \cdot \exp\left[j\left(\omega_d(u)t_n + \varphi_{dP}(u)\right)\right] \qquad (2.14)$$

The tracking of the primary code $\tau_{dP}(u)$ is done again with matched filtering. The reference signal is the envelope of $P(t)$ that is shifted by the previously estimated Doppler $\omega_d(u)$. For the secondary code, the matched filtering was done by shifting the reference signal in

Doppler frequencies and detecting the peak on a 2D (Doppler, delay) map. For the primary code, the Doppler shift is calculated, thus the reference signal gets time-delayed for the matched filtering. Finally, the phase and the navigation message can be extracted after the time-delayed and Doppler shifted primary code has been stripped from the received signal in equation (2.14). The navigation message is a BPSK modulation on primary code and can be regarded as a phase transition of $\pm\pi$ on the signal's phase $\varphi_{dP}(u)$. In this way, a phase transition detector can be used for the extraction of the phase and the navigation message. The phase and navigation message extraction is presented in the following diagram in Figure 2-14.

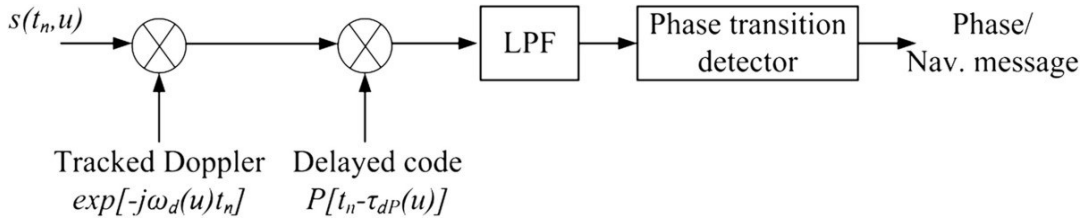

Figure 2-14: Phase/Navigation message extraction [42]

2.6.1. GLONASS Signal synchronization

The signal synchronization explained above is applied for confirmation using a GLONASS satellite signal for GNSS-based SAR. The experimental parameters are given in the following table.

Table 2-5: Experimental parameters

Parameter	Value
Satellite used	GLONASS COSMOS 744
Operating frequency	1604.8125 MHz (n=+5)
Primary satellite signal	P-code
Signal bandwidth	5.11 MHz
Dwell time	240 s
Satellite elevation	49°–55°
Satellite azimuth	85°–98°
PRF	1 kHz

The direct signal tracking outputs (tracked Doppler frequency, tracked delay, a part of the tracked Navigation message and the tracked phase spectrum) are presented in the figures below

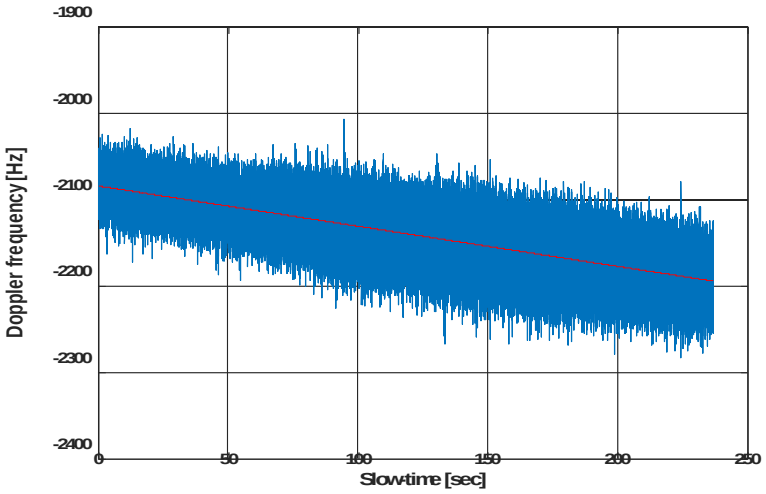

Figure 2-15: Tracked Doppler from direct signal

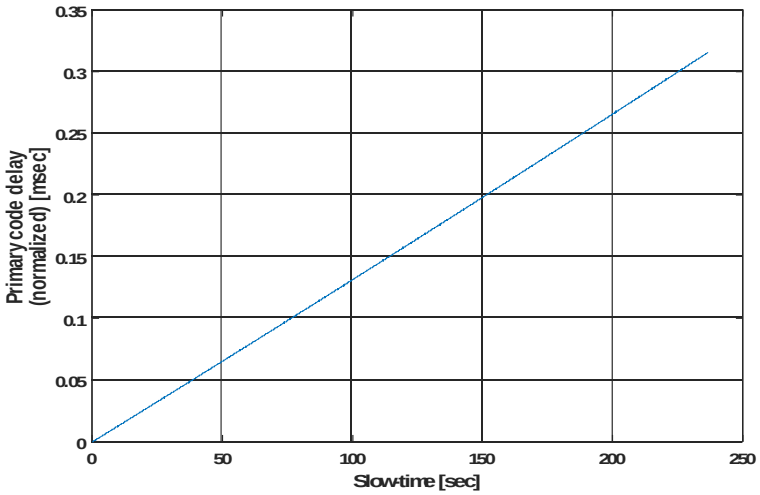

Figure 2-16: Tracked delay from direct signal (normalized)

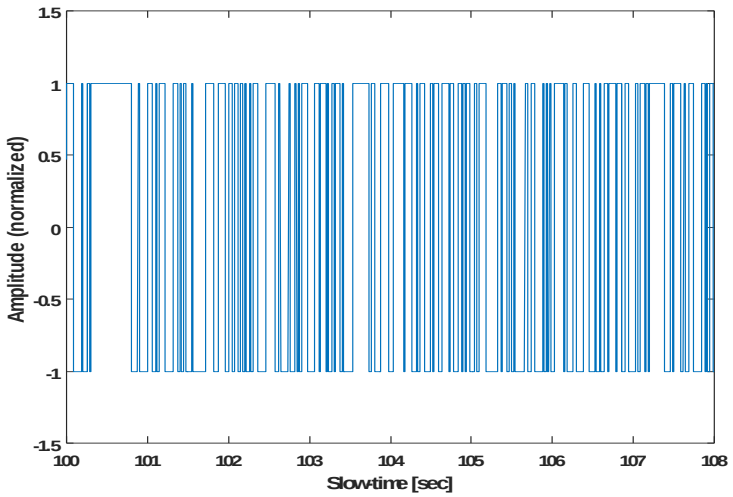

Figure 2-17: Tracked navigation message (part) from direct signal

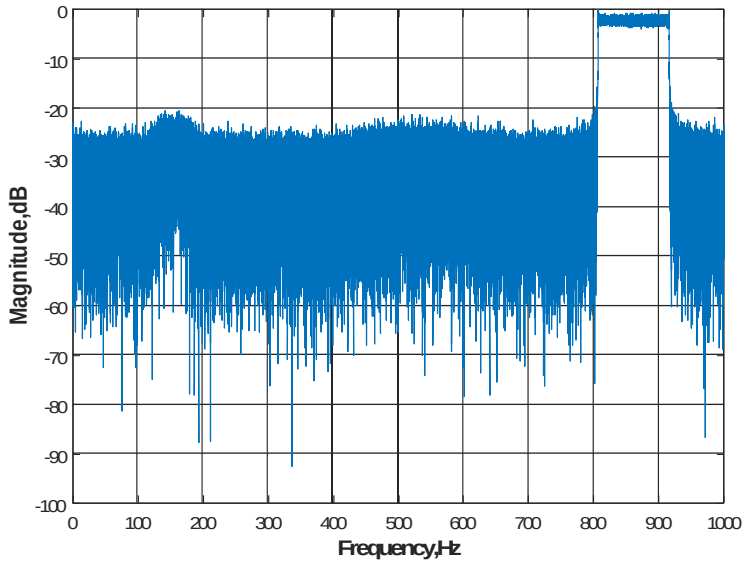

Figure 2-18: Tracked phase spectrum from direct signal

The phase spectrum that is presented above is the FFT of the complex exponential form of the tracked phase. The width of the chirp signal spectrum represents the Doppler spread of the signal for the duration of the experiment.

The tracked Doppler, the delay of primary code and the Navigation message are the information used for the next step of the processing. The additional information needed for the Image Formation algorithms are the geometrical parameters of the experiment.

2.7. Image formation

An image formation algorithm is required in order to generate the imagery of the scene under study. Bistatic SAR image formation algorithm has been developed and discussed for

decades. It can be divided into two categories: time domain algorithm and frequency domain algorithm. The time domain algorithm derives from original thoughts of forming the image by direct 2-D matched filter between raw data and conjugate of replica of echo signal [52], which is known as Time Domain Correlation (TDC) algorithm. It gives the best reconstruction accuracy. Sometimes, a faster variant, called Back Projection (BP) algorithm is used alternatively. Instead of performing 2-D correlation pixel by pixel, BP achieves block-by-block range compression for every azimuth bin before azimuth matched filter implemented. The time domain algorithm has good phase preservation and is exempt from bistatic geometry limit. However, such algorithms suffer from high computational loads, due to their processing is based on point-to-point. In addition, the range compression mentioned above is matched filtering between the two receiving channels (HC and RC) and the azimuth compression is implemented with fitted matched filter in the frequency domain, followed by residual error compensation. An overview of the Back-Projection algorithm for monostatic SAR is presented in the following figure.

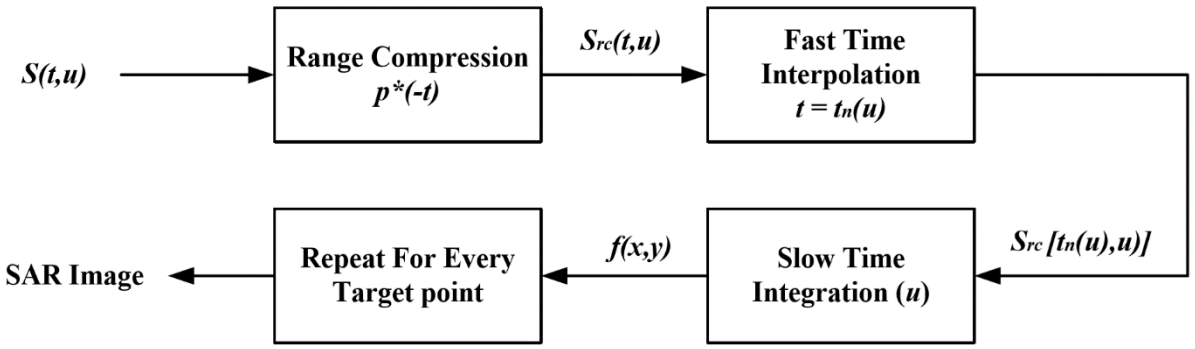

Figure 2-19: Block diagram of Back-Projection algorithm [43]

2.7.1. Back-Projection

To implement BP algorithm in practice, range compression is performed on raw data for every azimuth bin. Then the range history for a target point is mapped to all range compressed signal by fast-time interpolation. Finally, the interpolated values on all the azimuth bins accumulate coherently to get the response of this target point. To form a full image, the processes mentioned above will be repeated for all the pixels in the scene.

The advantage of the BP algorithm in bistatic SAR, is that it can be used when non-linear transmitter/receiver trajectories occur. Due to the fact that the satellite trajectories are nonlinear, frequency based algorithms are not applicable.

In general Bistatic SAR case two things are needed. The first is the synchronization outputs that are acquired using coherence maintaining methods. The second is the topology of the bistatic configuration of the acquisition. The topology is essential because different acquisition geometries imply different bistatic range/Doppler histories, and mismatches of the previous affect the efficiency of the processing algorithms. The receiver can be fixed on the ground or moving. However, since the transmitter is spaceborne, the geometry of the acquisition is not fully controlled despite the receiver configuration. The case of a fixed receiver is generally simpler to process, as in the moving case there is the addition of the complexity of motion compensation. The algorithm for image formation is similar for the moving receiver and fixed receiver scenarios with one difference. In the moving case there is a need of receiver motion compensation stage in the Back-Projection algorithm. The block diagram of the image formation algorithm is presented in the following figure.

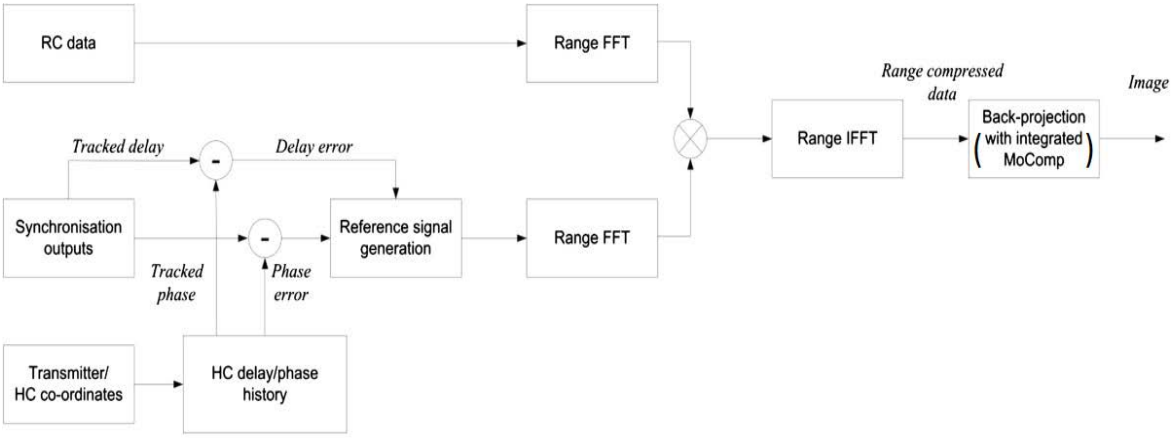

Figure 2-20: Image formation algorithm for Bistatic SAR

[for fixed (and moving) receiver] [42]

The image formation will be explained for the fixed receiver as this was used during the experimentation in this thesis.

Let us consider a three-dimensional GNSS-based SAR geometric model operating with a fixed receiver configuration as shown in the figure below.

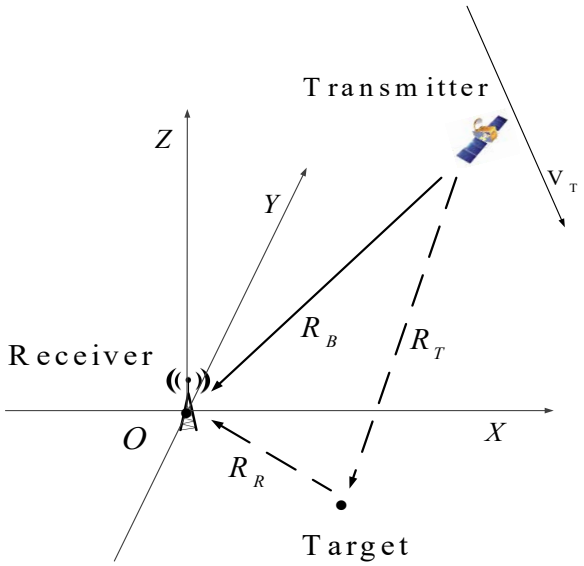

Figure 2-21: Bistatic SAR with spaceborne transmitter and fixed receiver

From the figure above we can see that the receiver is fixed and its coordinates are $(0, 0, 0)$. The range and the cross-range are selected independently to the trajectory of the transmitter, with fast-time (t) to be connected to the range dimension and slow-time to cross-range dimension (u). Also, the trajectory of the transmitter cannot be considered as a straight line, which can happen only for a relatively short observation time (e.g. moving receiver). The transmitter's coordinates are given as $(x_T(u),\ y_T(u),\ z_T(u))$. The heterodyne and the radar channels are both on the receiver, and the transmitter-receiver baseline is given as:

$$R_B(u) = \sqrt{\left[x_T(u)\right]^2 + \left[y_T(u)\right]^2 + \left[z_T(u)\right]^2} \tag{2.15}$$

Considering a point target in the imagery scene with coordinates $(x_{Ta},\ y_{Ta},\ z_{Ta})$ we get the instantaneous transmitter-target $(R_T(u))$ and receiver-target $(R_R(u))$ ranges as:

$$R_T(u) = \sqrt{\left[x_T(u) - x_{Ta}\right]^2 + \left[y_T(u) - y_{Ta}\right]^2 + \left[z_T(u) - z_{Ta}\right]^2} \tag{2.16}$$

$$R_R = \sqrt{\left[x_{Ta}\right]^2 + \left[y_{Ta}\right]^2 + \left[z_{Ta}\right]^2} \tag{2.17}$$

The Heterodyne Channel (HC) records the direct signal from the transmitter and the time delay and phase are related to $R_B(u)$. The Radar Channel (RC) records the reflected signal from the point target, where now the time delay and phase are related to the sum of $R_T(u)$ and $R_R(u)$. Nevertheless, these parameters are affected by other errors and the image focusing is impossible without the compensation of them. The sources of these errors may occur from receiver hardware artefacts $(t_{e_{Rx}}, \varphi_{e_{Rx}})$ or even from atmospheric propagation

($t_{e_{atm}}, \varphi_{e_{atm}}$). Considering these errors, the received signals at the HC and at the RC, after quadrature demodulation, can be written as:

$$s_{\mathrm{HC}}(t,u) = p\left\{t - \left[\frac{R_B(u)}{c} + t_{e_{Rx}} + t_{e_{\mathrm{atm}}}\right]\right\} \times \exp\left\{-j\left[\frac{2\pi}{\lambda} R_B(u) + \varphi_{e_{Rx}} + \varphi_{e_{\mathrm{atm}}}\right]\right\} \tag{2.18}$$

$$s_{\mathrm{RC}}(t,u) = p\left\{t - \left[\frac{R_T(u) + R_R}{c} + t_{e_{Rx}} + t_{e_{\mathrm{atm}}}\right]\right\} \times \exp\left\{-j\left[\frac{2\pi}{\lambda}\left(R_T(u) + R_R\right) + \varphi_{e_{Rx}} + \varphi_{e_{\mathrm{atm}}}\right]\right\} \tag{2.19}$$

where $p(t)$ is the transmitted signal envelope (primary code), c is the speed of light and λ is the radar wavelength.

As we can see from (2.18) and (2.19) the HC and RC show to have the same errors. This is due to the fact that they are identical channels on the same receiver and the oscillators are common for both channels. Therefore, they share the same common receiver errors and approximately equal atmospheric errors, since the range difference between $R_T + R_R$ and R_B is relatively small. For this reason, the errors that are tracked during the HC synchronization, can be used to compensate the errors in the RC.

In order to compensate the receiver and atmospheric errors it is essential to separate them from the terms that are connected with the baseline (see equation (2.18)). The time delay is actually $\left[R_B(u)/c + t_{e_{Rx}} + t_{e_{\mathrm{atm}}}\right]$ and the phase is $\left[2\pi R_B(u)/\lambda + \varphi_{e_{Rx}} + \varphi_{e_{\mathrm{atm}}}\right]$. This can be done if the transmitter and receiver coordinates are known. The way to do that is to calculate the $R_B(u)$ using the equation (2.15) and then remove it from the synchronization outputs. Once the errors are isolated, the reference signal for range compression can be written as:

$$s_0(t,u) = p\left[t - \left(t_{e_{Rx}} + t_{e_{\text{atm}}}\right)\right]\exp\left[-j\left(\varphi_{e_{Rx}} + \varphi_{e_{\text{atm}}}\right)\right] \tag{2.20}$$

We can observe that all the receiver and atmospheric errors change with slow-time u, but they are not direct functions of it. The range compression can be conducted in the order as:

1. in the fast-time frequency domain via an FFT on (2.19) and (2.20)
2. complex conjugate multiplication and
3. an inverse FFT.

At the output of this operation, the range-compressed RC data are modelled as:

$$r(t,u) = R_x\left[t - \frac{R_T(u) + R_R}{c}\right]\exp\left\{-j\frac{2\pi}{\lambda}\left[R_T(u) + R_R\right]\right\} \tag{2.21}$$

where $R_x(t)$ is the cross-correlation function between the received and reference signals in fast-time direction (range). We can see from eq (2.21) that the synchronization algorithm and the modified range compression scheme are effective in removing the receiver and atmospheric errors from the range-compressed data. The time delay and phase histories are solely due to propagation time delay and phase.

The last stage for the Back Projection Algorithm is the computation of the back-projection integral, which is similar to monostatic cases. A rectangular grid of points with coordinates (x_i, y_i) is needed for the BPA. The BPA back-tracks signal returns at the time delays (transmitter-target and receiver-target) associated with each target based on equations (2.16) and (2.17), and integrates over slow-time [42] [43], and it is given as:

$$f\left(x_i, y_j\right) = \int_u r\left[t_{ij}\left(u\right), u\right] du \tag{2.22}$$

where $t_{ij}\left(u\right) = \left(R_{Tij(u)} + R_{Rij}\right)/c$. When the data is discrete, the integration process can be approximated using complex summation. It is important to note here that the accuracy of the algorithm and the quality of the final image depend heavily on the accuracy of the known transmitter and receiver coordinates. In order to confirm the imaging ability of the system that is explained above, an experiment is to be set and the above algorithms are applied.

2.8. Validation

The validation of the above-mentioned imaging algorithm can be done experimentally. Apart from the acquired data that are the outputs of the receiver saved on the computer, the transmitter coordinates are needed too for the image formation. The transmitter coordinates can be acquired from the online database:

(https://cddis.nasa.gov/Data_and_Derived_Products/GNSS/orbit_products.html)

The format of the data provided is the global x,y and z coordinates of each satellite. The coordinates are given with a step of 15 minutes. Since the coordinates are given with this step, an interpolation process is needed. The coordinates are given in the earth centered coordinate system but a local coordinate system can be used with coordinate transformation. Conducting the experiments, the preferred method was the generation of a local coordinate system and the satellite coordinates were transformed to the local coordinate system. The advantage of this method is that the radar image is going to be generated for the desired area and the point (0,0) of the system refers to the location of the receiver. Also, it is easier to calculate distances for target confirmation.

As mentioned above, these coordinates are given with an interval of 15 minutes. However, the duration of each acquisition is approximately 5 minutes, and this interval is not enough. To create the desired interval, a number of satellite positions before and after the experiment are collected, and they should cover a duration of at least one hour, which means 4-6 sets of coordinates with interval of 15 minutes. These coordinates are used in a Lagrange interpolation which is a linear polynomial interpolation (see Appendix A). After this interpolation, we have the satellite trajectory values sampled every 1 second. With the timestamp accuracy to the size of seconds, we can select the starting and the ending points of the transmitter trajectory. When the appropriate part of the satellite trajectory is selected, it is interpolated with millisecond step. For this interpolation, a forth order least means square fitting curve is used. Finally we have ended up with the desired trajectory that is sampled every millisecond. This trajectory will be used for the image formation part.

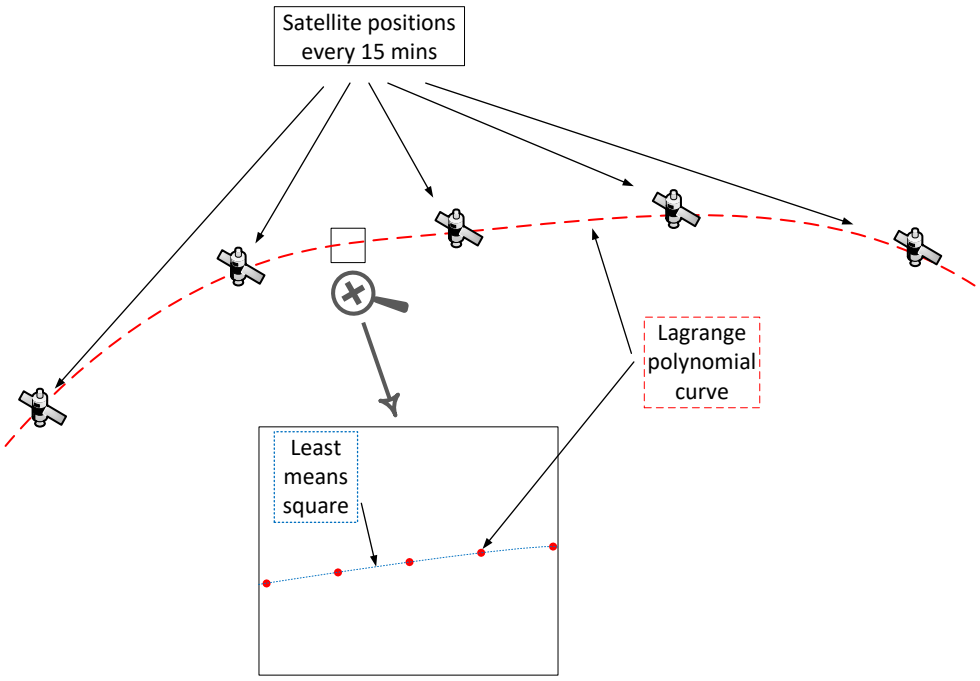

Figure 2-22: Coordinate transformation/interpolation process

An experiment for the validation of the algorithm is conducted. The area to be imaged is the area that is on the west of the Electronic, Electrical and Systems Engineering building. The interesting part of this area is that there are two grass fields that are separated by a tree line and beyond the grass areas there are four big buildings of different size and design. Here, in this area, the capabilities of the system can be tested. The satellite used is a GLONASS satellite and the experimental parameters of the acquisition are shown in the table below.

Table 2-6: Experimental parameters

Parameter	***Value***
Satellite used	GLONASS Cosmos 743
Satellite position	Elevation: 70 deg || Azimuth: 110 deg
Bistatic angle	40 deg
Carrier frequency	1605.375 MHz
Ranging code bandwidth	5.11 MHz
Wavelength	0.1868 m

A top view image of the area, acquired using the google earth program is given below.

Figure 2-23: Google Earth image for the west of EESE

The radar image generated using the above algorithm is given in the next figure. For comparison reasons, the area is shown again next to the radar image in the same scale.

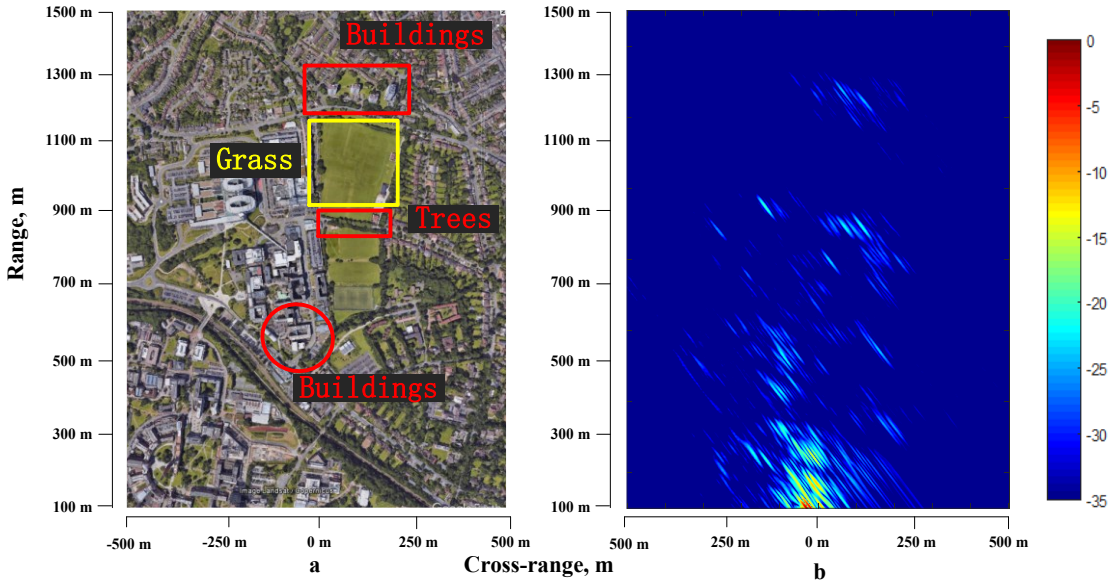

Figure 2-24: (a) Google Earth image, (b) SAR image

As we can see in the figure above, the SAR image is in good correspondence with the Google Earth image. The buildings near the receiver give higher power returns as expected, and we can also illuminate the trees at approximately 900 meters and the buildings at 1200-1300 meters range. The ranges are accurate enough for the SAR image due to the fact that the receiver is located close to the surface (roof of EESE ~30 m).

2.9. Point Spread Function analysis

The target detection ability of any radar system is defined by its target resolution. The definition of target resolution is same for all radar systems: the degree to which two or more targets may be separated in one or more dimensions, such as angle, range, velocity (or Doppler) etc. However, unlike monostatic SAR (1)-(2), the resolution in BSAR depends on

the bistatic data collection geometry. This issue is much more acute in GNSS-based SAR, due to its asymmetric topology and additionally due to the fact that special data acquisition geometries that often simplify matters are difficult, if possible at all, to implement in practice.

A general method for BSAR resolution analysis was proposed in [20], by means of the Generalized Ambiguity Function (GAF) approach [44], that is directly applicable to GNSS-based SAR.

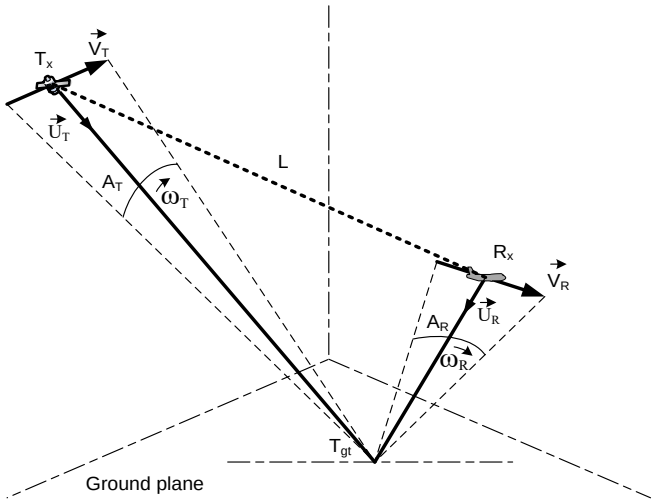

Figure 2-25: Bistatic SAR geometry

Figure 2-25 shows the general BSAR geometry used in the following analysis. L denotes the baseline between the transmitter and the receiver. $\overrightarrow{V_T}, \overrightarrow{\omega_T}, A_T$ are the transmitter's velocity, angular speed and coverage with respect to the target, and $\overrightarrow{V_R}, \overrightarrow{\omega_R}, A_R$ are the corresponding receiver parameters. $\overrightarrow{U_T}, \overrightarrow{U_R}$ are unit vectors in the transmitter-target and receiver-target directions, respectively.

To obtain the resolution performance, we can refer to the point spread function (PSF) or GAF [44]. The PSF describes the 2-D auto-correlation function of one point target and can be decomposed into the range and azimuth correlation functions, while the GAF is the 2-D correlation function in the delay-Doppler domain. Therefore, the PSF and the GAF are

representations of the same parameter but in different domains, and one can be transformed to the other via the appropriate domain transformation. The 3dB widths of GAF in range and azimuth dimensions are respectively the range resolution and azimuth resolution. Considering a ground-based stationary receiver collecting the signals emitted from a GNSS transmitter and reflected by one stationary point target, the two-dimensional bistatic resolution cell of such a system can be derived from the GAF. In the hypothesis of narrowband signal and narrow synthetic aperture, the GAF, $X(A,B)$, is given by the product of two normalized functions, $p(\cdot)$ and $m_{\mathrm{A}}(\cdot)$. The former is the matched filter output of the ranging signal and the latter is the inverse transform of the normalized received signal magnitude pattern. The derivation is lengthy and will not be shown here, but may be found in detail in [44]. The final result can be found as:

$$\left|\mathrm{X}\left(A,B\right)\right| \approx p\left(\frac{2\cos\left(\beta/2\right)\Theta^{T}\left(r\right)}{c}\right)\cdot m_{A}\left(\frac{2\omega_{E}\Xi^{T}\left(r\right)}{\lambda}\right) \tag{2.23}$$

where A is the vector position of the desired point reflector to be evaluated, vector B is an arbitrary position of another reflector in the vicinity of A and $r = B - A$; β is the bistatic angle and Θ is a unit vector in the direction of its bisector; $\omega_E = \frac{|\overrightarrow{\omega_T}+\overrightarrow{\omega_R}|}{2}$ and Ξ are called the equivalent angular speed and motion direction, since a monostatic SAR moving in the direction Ξ with angular speed ω_E would exhibit similar Doppler-based resolution characteristics, c is the speed of light and λ is the radar wavelength. The superscript 'T' denotes matrix transpose.

We define the resolution as the -3dB width of the PSF (2.23) in the range and azimuth directions. The bistatic range and azimuth resolutions, δ_r and δ_a , are along the directions of Θ and Ξ and can be found as [44]:

$$\delta_r = \frac{c}{2\Delta F \cos(\beta/2)}$$
$$\delta_a = \frac{\lambda}{2T_D \omega_E} \tag{2.24}$$

Comparing δ_r with its monostatic equivalent (equation (1.8), it can be seen that the bistatic range resolution is degraded by a factor of $\cos(\beta/2)$. The worst case scenario is when $\beta = 180^o$, which corresponds to a forward-scatter geometry where there is no range resolution ($\delta_r = \infty$). The best case scenario is the quasi-monostatic configuration, where the transmitter and receiver are directly behind each other so $\beta = 0^o$. In this case, the bistatic resolution is equal to the monostatic one, similar to the general case of bistatic radar [46].

For the azimuth resolution, $T_D \omega_E$ is similar to the length of the aperture along the direction of the BSAR equivalent motion. If an airborne receiver is used, the angular speed of the transmitter relevant to a target is negligible (since the satellite is at a distance of tens of thousands of km from it) compared to that of the receiver. In that case, the azimuth resolution is mainly defined by the receiver motion and can be written as:

$$\delta_a = \frac{\lambda R_R}{V_R T_D} \tag{2.25}$$

On the other hand, if the receiver is fixed, azimuth resolution is only defined by the motion of the satellite and can be calculated as:

$$\delta_a = \frac{\lambda R_T}{V_T T_D} \tag{2.26}$$

Therefore, to obtain a sufficiently high azimuth resolution in this mode, a long T_D is desirable. As an example, for GNSS, R_T is around 20,000 km (Table 2-2) and V_T, the orbital speed, is around 7km/s. For a GNSS wavelength in the order of 20cm, a dwell time of 300s (5mins) yields an azimuth resolution of approximately 2 m. For a dwell time on target of 0.5s, which is typical for a monostatic spaceborne SAR in low Earth orbit, the azimuth resolution would be nearly 1.15 km. So, long dwell time on target for GNSS-based SAR serve a dual purpose, to maximise both the SNR and the azimuth resolution. For acceptable resolution in azimuth the dwell time in the order of several minutes is required.

Moreover, it can be shown that very long dwell time on target can also the increase range resolution [47]. The main idea is that over the dwell time the trajectory of the satellite can no longer be approximated as a straight line. In terms of imaging and the PSF, this means that range and azimuth are no longer independent entities but rather they are coupled, and therefore an increase in the total dwell time/aperture length results in both an azimuth and range resolution increase. In order to quantify this, the extended Generalised Ambiguity Function (GAF) to equation (2.23) was derived as:

$$\left|\mathrm{X}_g\left(A,B\right)\right| = \left|\int p\left(f_{dc}/f_c \cdot \bar{u}\right) m_A\left(\bar{u}\right) exp\left(j2\pi f_{dc}\bar{u} + j\pi f_{dr}\bar{u}^2\right) d\bar{u}\right| \tag{2.27}$$

where $\bar{u} = u - u_c$ is the slow-time vector u minus the time u_c corresponding to the midpoint of the synthetic aperture, f_c is the carrier frequency and f_{dc}, f_{dr} are the Doppler centroid and Doppler rate, respectively.

Based on the extended GAF, the range and azimuth resolution improvements vs the dwell (integration) time on target could be computed, and also cross-checked with experimental

results from a GLONASS essential bistatic resolution. The same results could be compared by those expected from (2.23), as shown in Figure 2-26.

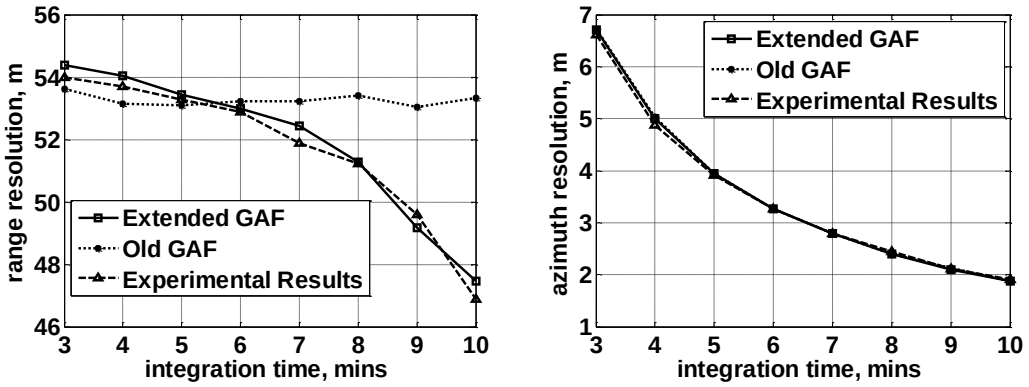

a) b)

Figure 2-26: a) Range and b) Azimuth resolution improvements for long dwell time on target [47]

The figure shows that for shorter integration times, the extended GAF (2.27) and the standard GAF (2.23) nearly coincide, as expected. However, as the integration time increases, the range resolution becomes finer. Of course this is one of the ways to improve the range resolution, and there are other techniques employing different principles.

For experiments that are less than 7 minutes, both the GAF and the extended GAF give almost equal results. Using a GLONASS satellite as a transmitter, 5 minutes integration time gives a sufficient resolution both in range and in azimuth. The theoretical form of the PSF in (2.23) has been confirmed using experimental data. An experimental PSF is obtained using a point-like target with GLONASS emissions. A simulated PSF is generated from (2.23) for the same bistatic geometry, as the expected PSF. The colourscale is in dB, with 0 dB representing the highest intensity point in the PSF. Two results are nearly identical, so (2.27) can be

replaced by the (2.23) when long integration times are taking place. It should also be stated that (2.23) holds for any BSAR system and is not restricted to GNSS-based SAR.

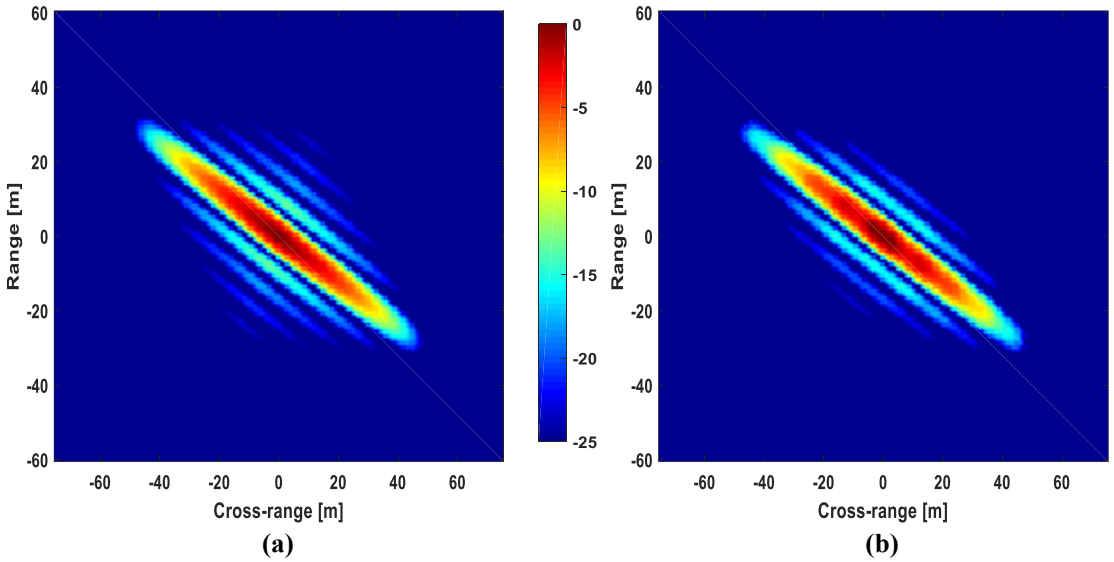

Figure 2-27: a) Theoretical and b) Experimental PSF for GNSS-based SAR

In GNSS-based SAR, since the transmitted signals are bit sequences, $p(\cdot)$ is a triangular function. On the other hand, due to the azimuth compression of the received signal, $m_{\mathrm{A}}(\cdot)$ is a $\mathrm{sinc}(\cdot)$ function, hence the shape of the PSF in Figure 2-27. For a better visualisation, Figure 2-28 shows an example PSF computed using (2.23) and assuming GLONASS transmissions, along with its range and azimuth cross-sections. The first thing to note is that the sidelobe directions are not orthogonal, which is unlike the monostatic SAR case. This is because the resolution directions Θ and Ξ are not orthogonal but depend on the bistatic acquisition geometry. This means that depending on the data collection geometry, the orientation, as well as the size, of the resolution cell will change.

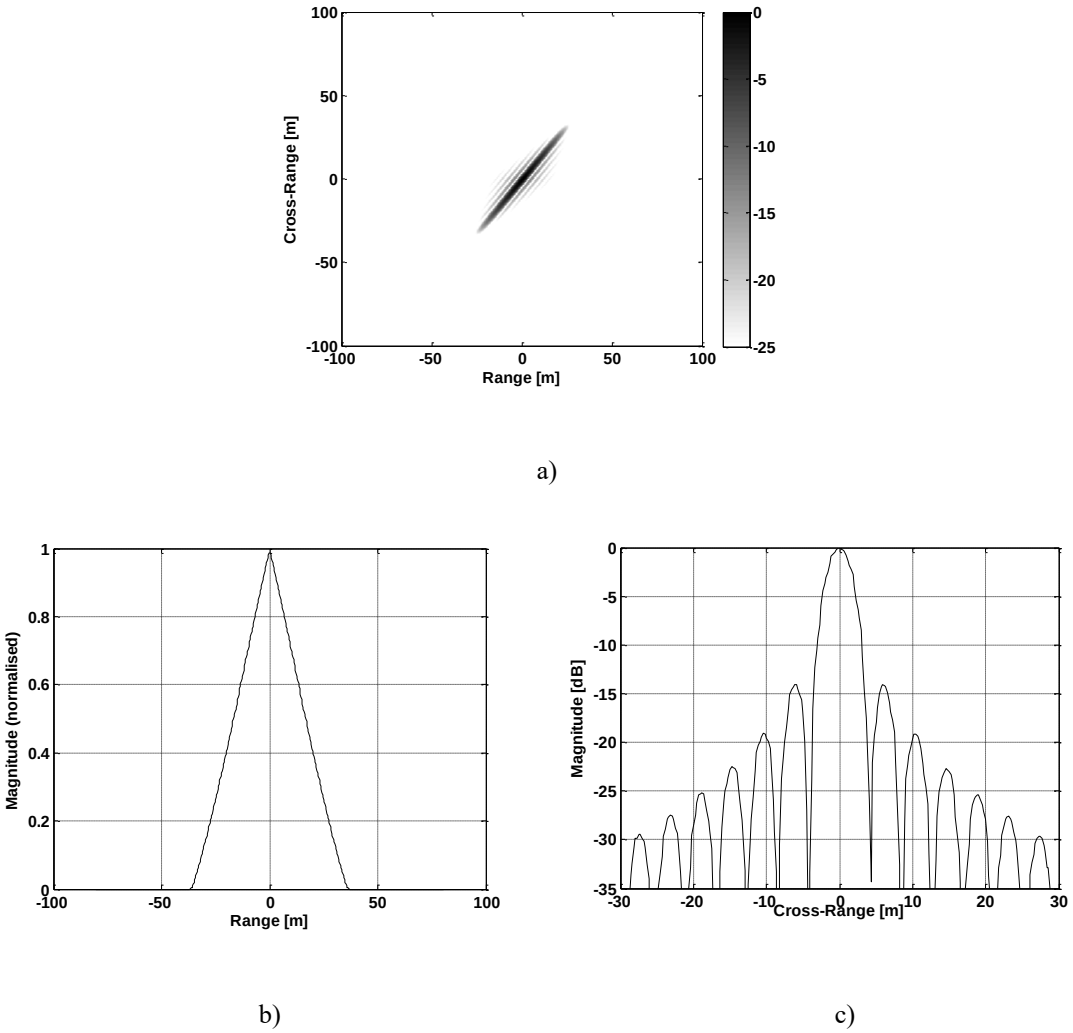

a)

b)

c)

Figure 2-28: a) Example PSF and its b) range, c) cross-range cross sections

2.10. Conclusions

In this chapter, the information about GNSS constellations is given and signal properties are presented. The operating frequency and the signal bandwidths for GNSS are shown. The GNSS signal power is explained and its power densities are studied. Following the signal power, the power budget analysis is done for GNSS-based SAR.

The spatial separation of the transmitter from the receiver and the low SNR of the GNSS-based SAR, make it impossible to use the signal for imaging without a synchronization process. Thus, the processing algorithm for the tracking of the GNSS signal is explained. Although the explanation is done for one system, GLONASS, the same algorithm is applied for any GNSS. The image formation algorithm is explained as well. The steps followed are explained and the back projection process is analysed. The approach is similar between the fixed receiver, that is explained, and the moving receiver cases. Experimental validation is done and the scene-image correspondence is shown.

Finally, the chapter concludes with the Point Spread Function analysis. The Generalized Ambiguity Function is presented for any bistatic spaceborne SAR, and the extended GAF is presented as a method of resolution improvement using long integration time. Theoretical PSF created using the GAF is compared to the experimental PSF. Also the range cross section and the cross-range cross section are presented.

Chapter 3 Coherent Change Detection

3.1. Introduction

In this chapter the Coherent Change Detection analysis is explained. The imaging radar that has been presented previously is able to generate images over scenes. Acquiring several images over a scene creates a question on the compassion of these images and whether any information can be extracted about the scatterers or whether the detection of any change that has occurred in the scene is noticeable. In this chapter the latter is to be studied.

The detailed study of scenes can be done in two ways. The first one is the interferometric SAR and the second is the Coherent Change Detection. In the interferometric SAR, two radar images are created with the use of two different antenna polarizations (horizontal-vertical or left-right hand). In the Coherent Change Detection the phase of each target is used for the study. It is important to note here that the targets are complex in shape, meaning many scatter points for each target. Thus the phase becomes a statistical value and not an absolute value.

The fundamental reason for the use of the Coherent Change Detection is the coherence. During every step of the synchronization and the image formation, the coherence is kept. This happens because only coherent methods of processing are used for the whole process.

By referring to coherence and coherent processes, there is a need of explaining what is this coherence. A process is called coherent when the phase continuance information is kept and used for every calculation. When a continuous signal is used, the phase information has a continuous form. In a coded pulse system, the phase continuity can be kept only if the complete signal during the acquisition time is processed. The used system, records and uses

the full signal for the whole acquisition period. Even though the signal is processed part by part, these parts still keep the continuity of the signal phase. Thus, the used system is categorized as coherent.

The image properties that are explained in the next paragraph, consist the base for the Coherent Change Detection.

3.2. Image properties

The observed area is being imaged using a GNSS system. The range and azimuth resolutions of this system depend on the system configuration as it has been explained in Chapter 2. The output image is a matrix that consists of complex values that correspond to each pixel of the image of the observed area. The output Image is formed using two variables. These are the Resolution Cell and the Resolution Pixel. The Resolution cell is a cell that includes the information of a specific area. In that area the existence of one or more targets cannot be distinguished. The Resolution Pixel refers to the fine resolution we choose to sample the area and also every Resolution Cell. Although the Resolution Cell dimensions for point targets are not controlled in the process, the Resolution Pixel dimensions can be controlled in the imaging process. In traditional SAR same dimensions for Pixel and Cell resolution are used, but in our case we choose a better Pixel resolution because the Cell resolution covers a rather big area. The Resolution Cell and the Resolution Pixel that are described above can be explained graphically in the next figure.

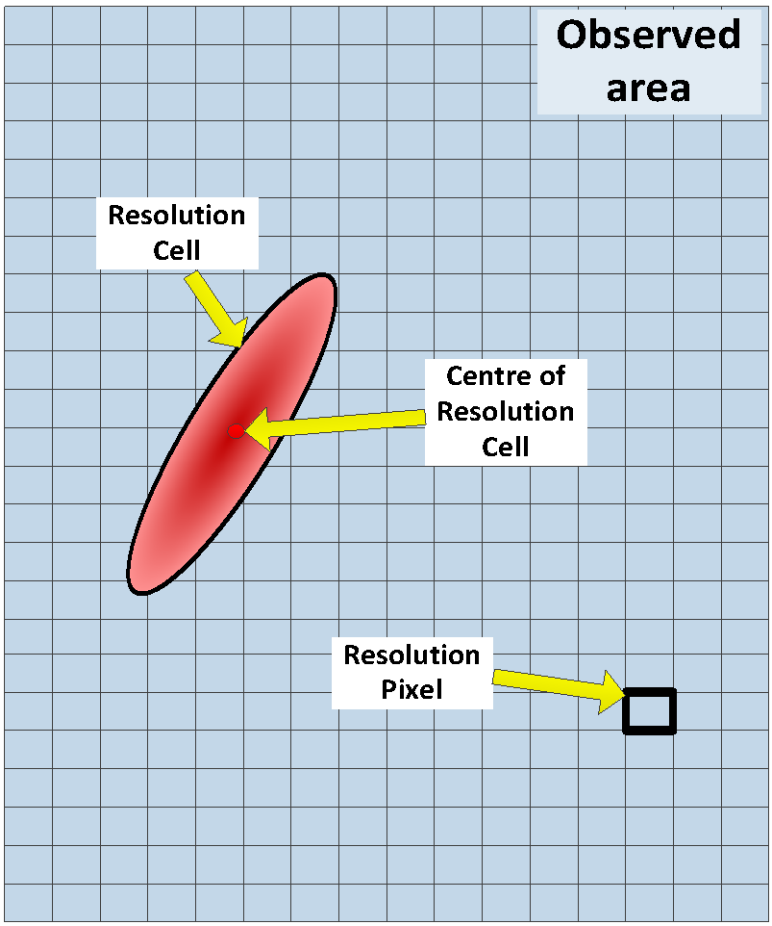

Figure 3-1: Observed Area, Resolution Cell and Image Pixel

In our system, the dimensions of the Resolution Cell are much greater than the Resolution Pixel dimensions. An approximate example is that the Resolution Cell has dimensions of 30 meters in the range and 5 meters in the azimuth, while the Resolution Pixel is selected to be 2m x 2m. At this point it is obvious that a signal return from a point target covers an area of many Pixels. In other words, a point target is spread in many Pixels. Although the center of the resolution cell is more opaque, it is sometimes difficult to define the exact position of a target that is not a point but has the dimensions. The situation becomes even more difficult and challenging when it comes to big targets or many scatter points close to each other.

The image formation process consists of only coherent processes. This means that at all times and all stages the coherence is kept, providing in this way accurate results. Although the imaging here is a result of a SAR system, each target return is the coherent summation of the returns at each dedicated point. As it is explained above, the aperture is considered to be separated in small dedicated positions separated by 1 millisecond, because this is the duration of one epoch.

Here we will analyze the image with physical meaning. Let us consider a monostatic SAR. The range and the azimuth information are given by the Delay and the Doppler of the received returns. The range resolution and the azimuth resolution define the dimensions of the resolution cell. In the same way, using the bistatic configuration, the resolution cell is defined in Bistatic SAR. The definition of a resolution cell is that all the scatterers in the resolution cell are going to contribute to the signal return that corresponds to that specific area. The figures below show the geometrical representation of the Resolution Cell in bistatic configuration and the Resolution Cell and the individual scatters.

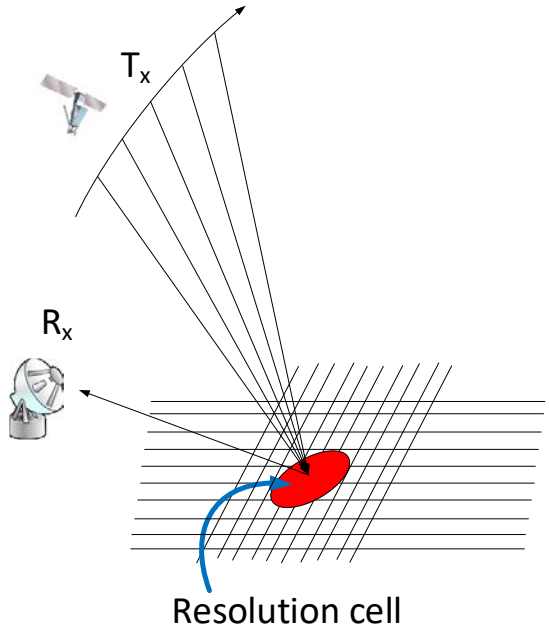

Figure 3-2: Resolution Cell in Bistatic SAR

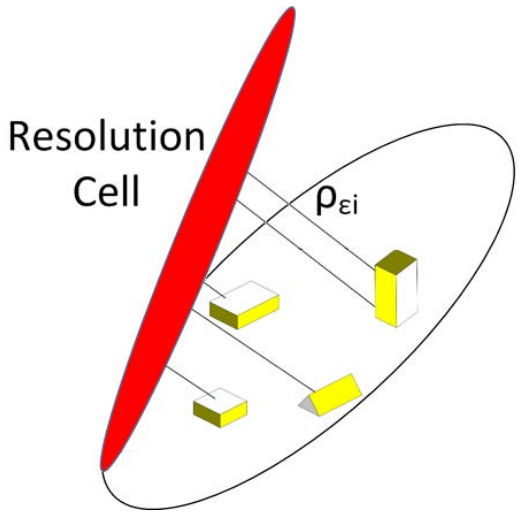

Figure 3-3: Resolution Cell formation

The reflected signal that corresponds to a resolution cell is given in the equation below.

$$S = A_b \cdot e^{-j\frac{4\pi}{\lambda}r_b} = \sum \left[A_{\varepsilon i} \cdot e^{-j\frac{4\pi}{\lambda}r} \cdot e^{-j\frac{4\pi}{\lambda}\rho_{\varepsilon i}} \right] \tag{3.1}$$

where r corresponds to the Transmitter-Target-Receiver range cell and $\rho_{\varepsilon i}$ corresponds to the range of every scatterer in the resolution cell. The return signal has the information about the magnitude and the phase as one value per resolution cell. For this reason, the isolated detection of a change of one scatter inside the resolution cell is not something that can be extracted, and an analytical prediction of the phase is difficult, if possible at all. However, since coherence is kept during all stages from data acquisition until the image formation for every acquisition/measurement, using the phase information is the way to compare target returns and calculate small changes. Since every signal return is a statistical value, only statistical results can be provided.

3.3. Coherence in Imaging

As it has been explained, the coherence needs to be kept at all stages until we get the output image. When using a SAR system on the same exact area, using the exact same configuration, we create an image pair of the same area. The purpose of such experiment is to compare the two images and detect changes that have occurred in the time period between the two images were acquired. In order to extract this kind of information, two methods are used. The first one is called Incoherent Change Detection, in which changes are identified by the use of power changes in the scene. The second is called Coherent Change Detection and it uses the amplitude and the phase information to identify changes in the scene. Although big changes in the scene can be extracted easily using Incoherent methods, small changes can be

detected only using Coherent Change Detection processes. These processes are also used in interferometry.

An image pair is needed for a Coherent Change Detection process to occur. In order to acquire an image pair, the acquisitions must have the same parameters. First and foremost the geometrical parameters should be the same. For both monostatic and bistatic SAR, the same synthetic aperture in terms of position-velocity of the radar is needed. Despite the minimization of error sources, small variations will still occur, and maybe the bistatic configuration introduces more complexity.

The GNSS-based SAR experimentation for Coherent Change Detection has a limitation though. The dependency on the GNSS transmitters controls the image pair creation. All satellites are on specific orbits, with specific trajectories and the revisit time is constant. For example, in the GLONASS constellation, the revisit is set to be eight sidereals days, and this is seven days, twenty three hours, twenty seven minutes and twenty eight seconds (7days 23hours 27minutes 28seconds). So by definition, the minimum revisit time is set by the constellation, and only with an integer multiplier of that. Also, sometimes the selected satellite can be on maintenance, and this increases more the revisit period. In general, revisit imaging is a time demanding process.

3.3.1. Coherent Processing of Image Pairs

The coherent processing of image pairs provides the opportunity of detection changes that cannot be detecting using Incoherent processing methods. In addition this provides a big boost on the capabilities of systems with not very high cell resolution. The image pairs need to be cross-compared in the amplitude and the phase. This is a kind of correlation, but since

we use also the phase information it is a complex correlation. The expression of this complex correlation of a SAR image pair, namely correlation coefficient, is given as [48]

$$\gamma = \frac{\left|\left\langle s_1 \cdot s_2^* \right\rangle\right|}{\sqrt{\left\langle s_1 \cdot s_1^* \right\rangle \cdot \left\langle s_2 \cdot s_2^* \right\rangle}} \tag{3.2}$$

where s_1 and s_2 represent the two pixels of the image pair under test (see equation (3.1), and $\langle \cdot \rangle$ denotes ensemble averaging. From the above equation (3.2) we can see the limits of the correlation coefficient to be as $0 \le \gamma \le 1$. The condition that gives the maximum value of the correlation coefficient γ=1 is when $s_1 = s_2$. In the following figure a general bistatic SAR is shown.

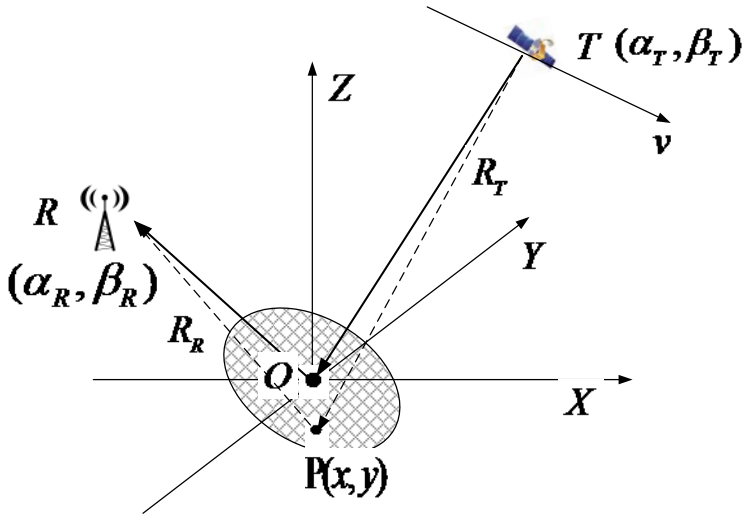

Figure 3-4: Bistatic SAR Geometry

To start with, we explain in more detail how the complex image is formed. In order to simplify the analysis, we consider local coordinate system with reference O(0,0) the center of a resolution cell at a point in the area under investigation.

According to the 'speckle' model, [48] and [51], the complex image pixel measured at the position O can be represented as the coherent summation of the complex returns of all the scatters in the resolution cell:

$$s = \iint \sigma(x,y)\exp(-j\frac{2\pi}{\lambda}(\mathrm{R}_T(x,y,\alpha_T,\beta_T)+R_R(x,y)))\cdot W(x,y)dxdy + n \tag{3.3}$$

where

- $\sigma(x,y)$ represents the complex backscatter coefficient at each point on the plane ,
- λ is the radar wavelength,
- a_T is the azimuth angle of the transmitter
- β_T is the elevation angle of the transmitter
- $R_R(x,y)$ is the distance from target to the receiver,
- $W(x,y)$ is the system's Point Spread Function
- and n is the system thermal noise.

The Point Spread Function for the used system using a linear satellite trajectory has been studied and analysed and it has the following form [20]:

$$|\mathrm{W(x,\ y)}| \approx tri\left(\frac{2\cdot\cos\left(\beta/2\right)\cdot\Theta^{\mathrm{T}}\cdot P(x,y)}{c\cdot\delta_\tau}\right)\times\sin c\left(\frac{2\cdot\omega_{\mathrm{E}}\cdot\Xi^{\mathrm{T}}\cdot P(x,y)}{\lambda\cdot\delta_d}\right) \tag{3.4}$$

Where

- $tri(\cdot)$ is the triangular function, specifying that the range resolutions for transmitter signals of GNSS are pseudorandom sequences,

- $\mathrm{sinc}(\cdot)$ specifies the azimuth resolution.,
- β is the bistatic angle ($T\hat{O}R$),
- Θ is the unit vector in the direction along the bisector of β,
- ω_E is the equivalent bistatic angular speed,
- Ξ is the unit vector along the satellite's motion direction, and
- $P(x,y)$ is the position vector of a scattering point P relevant to the origin,
- $\delta_\tau = 1/\mathrm{B}$ and $\delta_d = 1/T_{sys}$ are the time delay and Doppler resolution respectively (T_{sys} is the dwell time on target).

Generally, paramenters Θ and Ξ define the direction of the range and azimuth resolution respectively.

With the expression $S_1 = S_2$ it is meant that the two image pixels are exactly the same. In practice, there are several unrelated components between S_1 and S_2 that affect their complex correlation. In interferometric SAR and Coherent Change Detection there are three major factors that affect the decorrelation of an image pair, and they are shown in the following equation:

$$\gamma = \gamma_{Thermal} \cdot \gamma_{Spatial} \cdot \gamma_{Temporal} \tag{3.5}$$

where

a) the Thermal decorrelation factor $(\gamma_{Thermal})$,

b) the Spatial decorrelation factor $(\gamma_{Spatial})$

c) the Temporal decorrelation factor $\left(\gamma_{Temporal}\right)$

The above factors control the coherence level between the two images (summation of image pixels). However, with good experimentation and in depth study, the influence of one sole factor might be possible to calculate. The objective in this study is the calculation of the temporal decorrelation factor with a change on a target in the scene. Firstly, we try to minimize the thermal and the spatial factors, and then to study the relation between a target change and the temporal decorrelation factor. Therefore, measuring the coherence needs to be done in steps.

3.4. Measuring Coherence

Although measuring the coherence level between two images of an image pair is a simple process, the method to be used has an important role. The calculation of a single decorrelation factor is not something that can be done easily. In order to isolate the temporal decorrelation factor out of the equation (3.5) the calculation of the thermal and spatial factors is also needed. The minimization of the thermal and spatial factors needs to be confirmed experimentally before the temporal factor gets under the study. The best way to do so, is to study first the stability when no change has occurred. In other words, the coherence level when the temporal decorrelation is not present ($\gamma_{temporal} = 1$). This can be done when stability measurements are acquired and studied first.

The provision for the minimum possible thermal and spatial decorrelation is essential for this study. An experimental program is needed, in which the thermal and spatial decorrelation factors are kept as low as possible ($\gamma_{thermal} \cong 1 \; and \; \gamma_{spatial} \cong 1$) and the temporal decorrelation to be considered as non-existent ($\gamma_{temporal} = 1$). Also, during the image

processing, the image properties need to be taken into account. The image properties give some specifications about the image processing such as pixel to pixel processing and if a certain processing/averaging window is needed. The image properties that were mentioned in the previous paragraph can be used in the way explained below.

3.4.1. Image properties in coherence calculation

In most monostatic SAR systems the resolution cell and the resolution pixel coincide. Thus, the scene is represented in a matrix of complex values (image). The dimensions of the matrix depend on the resolution of the system, and each value corresponds to a specific resolution cell. In this way, the coherence in an image pair is calculated for each value of the image matrix. In bistatic SAR systems, where the resolution cell and the resolution pixel do not have the same dimensions, a window processing mode is used.

Using a window for the process of the image has both positive and negative effect. The disadvantage is that the resolution/accuracy decreases. But usually this is a price that most system can afford up to a point. On the other hand the advantage is big mostly in terms of noise reduction. For example, let us consider a system with lower cell resolution than pixel resolution (like the used system). When decreasing the pixel resolution that is still kept higher than the cell resolution is not going to create big loss. The use of an averaging window is going to provide more solid results. Averaging is a widely used technique in the interferometry, it is usually used to reduce the air turbulence effect and also the speckle noise.

The used window can be rectangular or square. It is advised that the window should have the form of the Ambiguity Function of the system. In the current system, the Ambiguity Function has an ellipsoid shape, and for this reason a rectangular shaped window is used. Also, for rectangular windows, the dimensions should have a ratio of 1:3 or 1:4. In the analysis of the

data, the windows that are used are rectangular, with ratio as suggested. The absolute dimensions varied also for better evaluation of the data. In order to enhance better results, the orientation of the window is selected to be the same to the orientation of the Point Spread Function of the measurements.

3.5. Decorrelation factors analysis

In order to create an experimental program for the temporal decorrelation calculation, the correlation coefficient components need to be analysed. As shown before in equation (3.5), the correlation coefficient components are:

$$\gamma = \gamma_{Thermal} \cdot \gamma_{Spatial} \cdot \gamma_{Temporal}$$

In the paragraphs below these components (decorrelation factors) are analysed.

3.5.1. Thermal decorrelation

The thermal factor or noise factor depends on the system features, as is the gain and the antenna characteristics. A widely used form to calculate the thermal factor is given below:

$$\gamma_{thermal-1,2} = \frac{1}{\sqrt{\left(1+1/SNR_1\right)\cdot\left(1+1/SNR_2\right)}} \tag{3.6}$$

The decorrelation factor is calculated per pixel for the image pair. Each pixel from the first image is compared to the equivalent pixel of the second image, with 1 and 2 to refer to the images of the pair as first and second respectively.

The Thermal decorrelation factor can be seen also as γ_{SNR}, and stands for the decorrelation effect due to the reality of finite signal-to-noise ratio (SNR) of the system. The SNR in a passive Bistatic Synthetic Aperture Radar is a little different from the traditional monostatic SAR, mostly due to the bistatic configuration. Here we only consider the targets that have RCS independent of frequency and aspect angle. After the range and azimuth compression, the final SNR can be written as:

$$SNR = \frac{P_t G_t}{4\pi R_t^2} \cdot \frac{A_r \sigma}{4\pi R_r^2} \cdot \frac{\tau_i}{\tau_o} \cdot \frac{PRF \cdot T_c}{KT_0 FB} \cdot \eta \tag{3.7}$$

where

- $\frac{P_t G_t}{4\pi R_t^2}$ is the power flux density on the earth's surface produced by the GNSS signal,
- A_r is the effective area of receiver antenna,
- R_r is the range from the target to receiver,
- σ is the RCS of the target,
- τ_i the uncompressed signal duration,
- τ_0 is the compressed signal duration,
- KT_0FB is the noise power (with B the bandwidth and F the noise factor),
- T_c is the duration of time integration, and
- η is the loss factor in our system.

It is worth to note that $B \cdot \tau_0 \approx 1$, and $PRF \cdot \tau_i = 1$.

Letting $\rho = \frac{P_t G_t}{4\pi R_t^2}$ is the signal power, $T_c = \frac{R_r \cdot \lambda}{V \Delta_{az}}$ is the integrated time, the SNR of SS-BSAR can be rewritten as:

$$SNR = \rho \cdot \frac{A_r \sigma}{4\pi R_r^2} \cdot \frac{T_c \cdot \eta}{K T_0 F} \tag{3.8}$$

Using the parameters listed in the Table 2-2, we can obtain the SNR of SS-BSAR as shown in Figure 3-5.

Table 3-1: The parameter of SS-BSAR

Parametters	Value
Signal Power Density	1.42×10^{-14} W/m^2
Effective area of Receiver Antenna	0.5 m^2
Integrated Time	300 s
Antenna Noise Temperature	290 K
Receiver Noise Factor	1.41254 (or 1.5 dB)
Loss	0.5

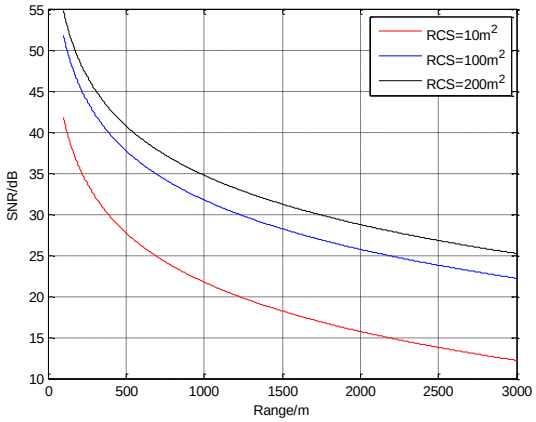

Figure 3-5: The SNR of SS-BSAR

Therefore, the SNR decorrelation of SS-BSAR with respect to the range of receiver is shown below:

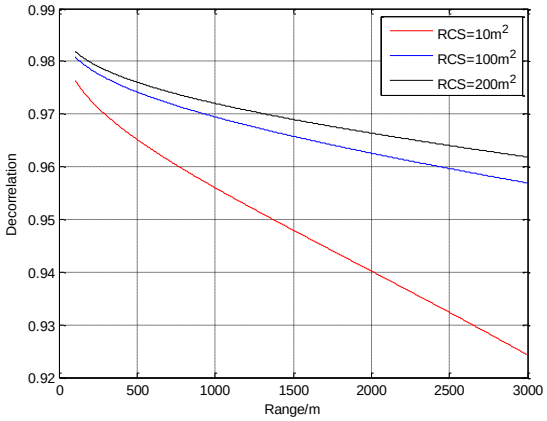

Figure 3-6: The SNR decorrelation of SS-BSAR

As it can be shown in Figure 3-5 and Figure 3-6, with the increase of range, the SNR is decreasing and the correlation is also decreasing. Keeping the range of receiver invariant, the SNR and correlation increase with the increase of RCS.

3.5.2. Spatial decorrelation

The spatial decorrelation analysis studies the signal decorrelation due to spatial errors and differences on the radar aperture that is the transmitter trajectory in our case. Here again we start from equation (3.2) with the correlation coefficient

$$\gamma = \frac{\left|\left\langle s_1 \cdot s_2^* \right\rangle\right|}{\sqrt{\left\langle s_1 \cdot s_1^* \right\rangle \cdot \left\langle s_2 \cdot s_2^* \right\rangle}}$$

where s_1 and s_2 are the complex images (primary and repeat respectively) over the same scene, received using a fixed receiver. In the following figure the topology is reshown.

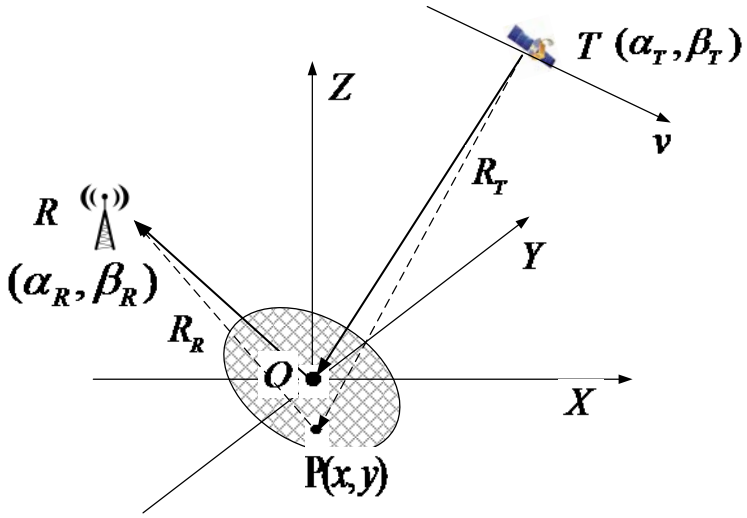

Figure 3-7: Bistatic SAR Geometry

For the simplicity of the analysis, as previously, we consider local coordinate system with reference O(0,0) the center of a resolution cell at a point in the area under investigation.

Due to motion errors that occur on the trajectory of the transmitter, the correlation coefficient decreases. Considering an image pair, with s_1 as the primary image and s_2 as the repeat pass image we have [50]:

$$s_1 = \iint \sigma(x,y)\exp\left[-j\frac{2\pi}{\lambda}\left(\mathrm{R}_{T1}\left(x,y,\alpha_{T1},\beta_{T1}\right)+R_R\left(x,y\right)\right)\right]\cdot W(x,y)dxdy + n_1 \tag{3.9}$$

$$s_2 = \iint \sigma(x,y)\exp\left[-j\frac{2\pi}{\lambda}\left(\mathrm{R}_{T2}\left(x,y,\alpha_{T2},\beta_{T2}\right)+R_R\left(x,y\right)\right)\right]\cdot W(x,y)dxdy + n_2 \tag{3.10}$$

Thus we have:

$$\begin{aligned} s_1 s_2^* = \int\int\int\int \sigma\left(x,y\right)\sigma^*\left(x',y'\right)\exp\left[-j\frac{2\pi}{\lambda}\left(R_{T1}+R_R\right)\right]W\left(x,y\right) \\ \times\exp\left[j\frac{2\pi}{\lambda}\left(R_{T2}+R_R\right)\right]W^*\left(x',y'\right)dxdydx'dy' \end{aligned} \tag{3.11}$$

And assuming that the imaged surface consists of uniformly distributed and uncorrelated scattering center we have:

$$\left\langle \sigma(x,y)\sigma^*(x',y')\right\rangle = \sigma^0\cdot\delta(x-x',y-y') \tag{3.12}$$

where σ^0 is the average complex backscatter coefficient. Applying the (3.12) in the (3.11) we take:

$$\begin{aligned} \left\langle s_1 s_2^*\right\rangle &= \iint \sigma^0\exp\left[-j\frac{2\pi}{\lambda}\left(\mathrm{R}_{\mathrm{T1}}\left(x,y,\alpha_{T1},\beta_{T1}\right)-R_{T2}\left(x,y,\alpha_{T2},\beta_{T2}\right)\right)\right]\cdot\left|W(x,y)\right|^2 dxdy \\ &= \sigma^0\exp\left[-j\frac{2\pi}{\lambda}\left(R_{T1}-R_{T2}\right)\right]\cdot\iint\exp\left[-j\frac{2\pi}{\lambda}\left(x\cdot U+y\cdot V\right)\right]\cdot\left|W(x,y)\right|^2 dxdy \end{aligned} \tag{3.13}$$

Where U and V are determined by the position offset of the transmitter:

$$U = \cos a_{T2} \cos \beta_{T2} - \cos \alpha_{T1} \cos \beta_{T1} \tag{3.14}$$

$$V = \sin a_{T1} \cos \beta_{T1} - \sin \alpha_{T2} \cos \beta_{T2} \tag{3.15}$$

In a similar way the autocorrelation of the images can be given as:

$$\left\langle s_1 s_1^* \right\rangle = \left\langle s_2 s_2^* \right\rangle = \sigma_0^2 \cdot \iint \left| W(x,y) \right|^2 dxdy \tag{3.16}$$

Substituting (3.13) and (3.16) in (3.2) and after simplifying, the correlation coefficient caused by spatial decorrelation can be calculated by:

$$\gamma = \frac{\left| \iint \exp\left[-j \frac{2\pi}{\lambda} \left(x \cdot U + y \cdot V \right) \right] \cdot \left| W(x,y) \right|^2 dxdy \right|}{\iint \left| W(x,y) \right|^2 dxdy} \tag{3.17}$$

From equation (3.17), the spatial coherence equals 1 if $U = V = 0$. In all other cases $0 \le \gamma < 1$. In addition, the calculation of (3.17) is also dependent on the PSF $W(x,y)$.

Let us consider a bistatic geometry for the validation of the above approach, and that will be the quasi-monostatic topology. In the quasi-monostatic scenario the transmitter and the receiver are at the same azimuth position. From PSF analysis we can consider the $W(x,y)$ as [50]:

$$W(x,y) = tri\left(\frac{y}{R_r} \right) \cdot \sin c\left(\frac{x}{R_a} \right) \tag{3.18}$$

where

$$\begin{cases} R_r = \dfrac{c\delta_\tau}{2\cos^2(\beta_b/2)} \\ R_a = \dfrac{\delta_D \lambda}{2\omega_E} \end{cases} \tag{3.19}$$

- ***Azimuth offsets***

If the elevation angle is assumed to be fixed, i.e., $\beta_{T1} = \beta_{T2} = \beta$ and only the azimuth angle offset $\delta\alpha = \alpha_{T1} - \alpha_{T2}$ is considered, U and V reduce to

$$\begin{cases} U = \cos\beta \cdot (\cos\alpha_{T2} - \cos\alpha_{T1}) = \cos\beta \sin\alpha\delta\alpha \\ V = \cos\beta \cdot (\sin\alpha_{T1} - \sin\alpha_{T2}) = \cos\beta \cos\alpha\delta\alpha \end{cases} \tag{3.20}$$

where $\alpha = (\alpha_{T1} + \alpha_{T2})/2$. For the quasi-monostatic configuration and assuming that the offset is slight, then $\alpha \approx \pi/2$. Hence, the (3.17) becomes

$$\gamma = 1 - \frac{|\cos\beta\delta\alpha|}{\lambda} \cdot R_a \tag{3.21}$$

- ***Elevation offsets***

Similarly, if the azimuth angle is assumed to be fixed, i.e., $\alpha_{T1} = \alpha_{T2} = \pi/2$ and only the elevation angle offset $\delta\beta = \beta_{T1} - \beta_{T2}$ is considered, then

$$\begin{cases} U = 0 \\ V \approx \sin\beta \cdot \delta\beta \end{cases} \tag{3.22}$$

where $\beta = \left(\beta_{T1} + \beta_{T2}\right)/2$. Thus

$$\gamma = \mathbf{F}\left(tri^2\left(\frac{y}{R_r}\right), \sin\beta \cdot \delta\beta \right) \tag{3.23}$$

The spatial de-correlation coefficient due to different azimuth (3.21) or elevation (3.23) offsets is plotted in Figure 3-8 for a quasi-monostatic configuration in example. The calculation parameters correspond to those of a GLONASS satellite, and are listed in Table 3-2. It is assumed that the satellite azimuth and elevation angles in the first pass are $\alpha_{T1} = 90^\circ, \beta_{T1} = 85^\circ$. The two-dimensional resolution can be calculated using equation (3.19) for the listed parameters as $R_a = 3.04m, R_r = 39.14m$.

Table 3-2: Calculation parameters

Parameters	Value
Satellite effective velocity	3953 m/s
Carrier Frequency	1602.5625 MHz
Signal Bandwidth	5.11 MHz
Integration Time	300 s
Satellite-to-Target Range r_{T0}	19284 Km
Receiver Azimuth Angle	90 deg
Receiver Elevation Angle	5 deg

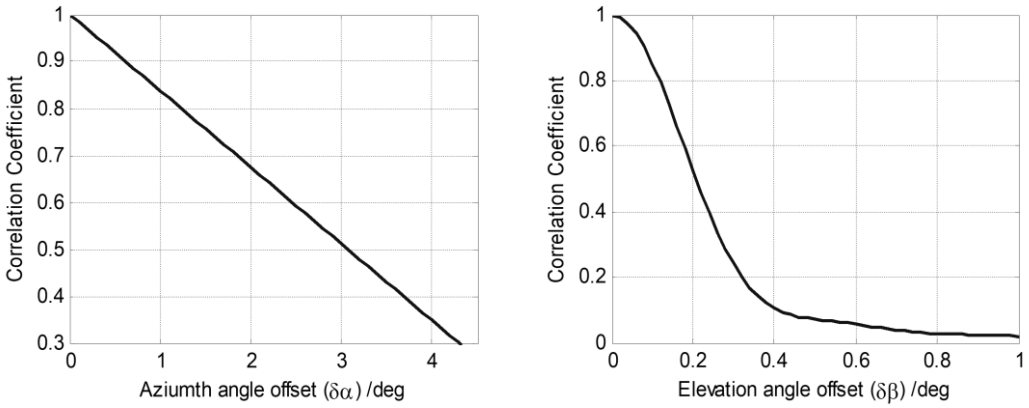

(a) (b)

Figure 3-8: Spatial de-correlation in quasi-monostatic configuration due to (a) azimuth, (b) elevation angle offsets [50].

It can be seen from Figure 3-8 that the correlation coefficient decreases as the angular offset increases, as expected. Moreover, the spatial de-correlation due to elevation offsets is much more sensitive than those due to azimuth offsets. The main reason for this is the difference in the range and azimuth resolutions. Inspection (3.21) and (3.23) demonstrates that spatial de-correlation due to azimuth offsets depends on azimuth resolution, whereas that due to elevation offsets depends on range resolution. Since $R_r \gg$ for GNSS-based SAR, the sensitivity to spatial effects is more pronounced on (3.23).

The validity of the analytical derivations made above is tested using Monte Carlo simulations. It is assumed that a set of 10,000 scattering centres are located randomly within a resolution cell. Changes in the satellite's position were added and the corresponding image signal s_2 was calculated in the same way. The correlation coefficient between the two images

was then calculated directly using equation (3.2). This process was repeated 1,000 times to get the ensemble average.

A comparison between the simulated and theoretical results for the quasi-monostatic configuration is shown in Figure 3-9. It can be seen that the simulation result is in agreement with the theoretical derivation. Any difference between simulated and theoretical results is accredited to the truncated impulse response used in the simulations. This is not a special problem in BSAR, and has also been encountered with monostatic SAR data [48].

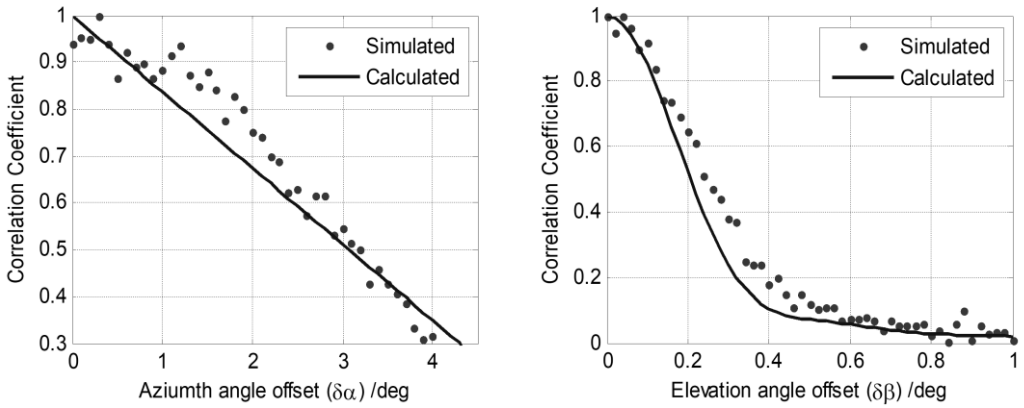

(a) (b)

Figure 3-9: Simulation result of spatial de-correlation effect in quasi-monostatic configuration, (a) Spatial de-correlation due to the elevation angle's variation, (b) Spatial de-correlation due to the azimuth angle's variation [50].

3.5.3. Temporal Decorrelation

The Temporal decorrelation refers to the decorrelation of the correlation coefficient that is connected to physical changes in the scene over the time period between the observations. Thus, the Coherent Change Detection was introduced, and it aims to study the property of change through the correlation coefficient. During the last years many models have been created for different scenes of interest, e.g. vegetated areas, urban areas, etc. The most generic and appropriate for the used system in this study is the one that the temporal decorrelation is based on the volume scattering model. The figure below is used for the explanation of the model.

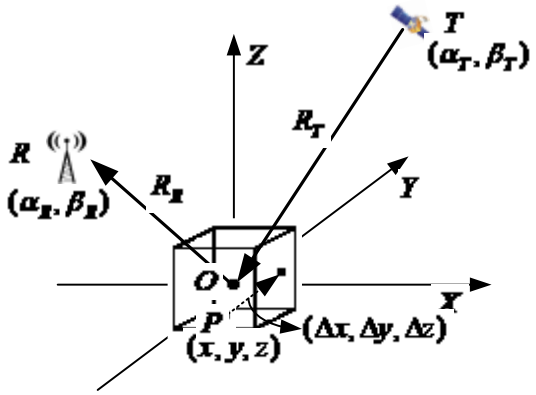

Figure 3-10: Resolution cell and imaging geometry in BSAR

For the simplicity of the analysis, as previously, we consider local coordinate system with reference O (0,0,0) the center of a resolution cell at a point in the area under investigation.

In Figure 3-10, the imaging geometry and the resolution cell of a target are presented, where *O* refers to the centre of the resolution cell. Here we have the three dimensions of the resolution cell and change in any direction (x,y,z) will apply phase change on the signal return. As for the Spatial decorrelation analysis, the a_T and β_T are the azimuth and the

elevation angles for the transmitter, and a_R and β_R are the azimuth and the elevation angles for the receiver, respectively. Starting again from the equation (3.2), we need to define the complex SAR received images s_1 and s_2 for the target *P* as below, where s_1 is the primary image and s_2 is the repeat pass image.

$$s_1 = \iiint f_1(x,y,z)\exp\left[-j\frac{2\pi}{\lambda}\left(R_T + R_R\right)\right]W(x,y)dxdydz + n_1 \tag{3.24}$$

$$s_2 = \iiint f_2(x,y,z)\exp\left[-j\frac{2\pi}{\lambda}\left(R_T + R_R\right)\right]W(x,y)dxdydz + n_2 \tag{3.25}$$

where $W(x,y)$ is the system response function, n_1 and n_2 are the system thermal noise, $f_1(x,y,z)$ and $f_2(x,y,z)$ represent the complex scattering density of the target for the primary acquisition and the repeat-pass acquisition, respectively.

Assuming a displacement of a scatter from the position (x,y,z) by $(\Delta x, \Delta y, \Delta z)$ occurs in the meantime between the primary and the repeat acquisitions. This results to a Trasmitter-Target-Receiver range change that can be expressed as:

$$\begin{aligned}\Delta R(\Delta x,\Delta y,\Delta z) = {} & \Delta x\cdot(\cos\alpha_T\cos\beta_T + \cos\alpha_R\cos\beta_R) \\ & + \Delta y\cdot(\sin\alpha_T\cos\beta_T + \sin\alpha_R\cos\beta_R) \\ & + \Delta z\cdot(\sin\beta_T + \sin\beta_R)\end{aligned} \tag{3.26}$$

Also, here we assume that the dielectric constant of the scattering elements is unchanged during the acquisitions. For this, we get:

$$f_2(x,y,z) = f_1(x,y,z)\cdot\exp\left[j\frac{2\pi}{\lambda}\cdot\Delta R(\Delta x,\Delta y,\Delta z)\right] \tag{3.27}$$

Using the above relation, we can start to calculate the correlation coefficient γ.

$$s_1 s_2^* = \iiint\iiint f_1(x,y,z) f_2^*(x',y',z')\cdot W(x,y)W(x',y')dxdydzdx'dy'dz' \tag{3.28}$$

Here we consider the two complex scattering densities as uniformly distributed as:

$$\begin{aligned}\left\langle f_1(x,y,z) f_2^*(x',y',z')\right\rangle = \rho(x,y,z)\cdot\exp\left[-j\frac{2\pi}{\lambda}\cdot\Delta R(\Delta x,\Delta y,\Delta z)\right] \\ \times\delta(x-x',y-y',z-z')\end{aligned} \tag{3.29}$$

where $\langle\cdot\rangle$ indicates ensemble average, and $\rho(x,y,z)$ is the average complex scattering density, representing the structure function of the resolution cell. Furthermore, assuming that the random motion of the scatterers is the dominant dynamic process that occurs within the resolution cell, and the position changes can be characterized by independent probability distributions $p_x(\Delta x)$, $p_y(\Delta y)$ and $p_z(\Delta z)$, we get

$$\begin{aligned}\left\langle s_1 s_2^*\right\rangle = \iiint\iiint \rho(x,y,z)\cdot\exp\left[-j\frac{2\pi}{\lambda}\cdot\Delta R(\Delta x,\Delta y,\Delta z)\right]\cdot|W(x,y)|^2 \\ \cdot p_x(\Delta x)p_y(\Delta y)p_z(\Delta z)dxdydzd\Delta xd\Delta yd\Delta z\end{aligned} \tag{3.30}$$

and

$$\left\langle s_1 s_1^*\right\rangle = \left\langle s_2 s_2^*\right\rangle = \iiint \rho(x,y,z)|W(x,y)|^2 dxdydz \tag{3.31}$$

where the thermal noises are assumed uncorrelated with each other and with the signals.

Instituting the equations (3.30), (3.29) and (3.31) into equation (3.2) yields the correlation coefficient caused by temporal de-correlation. The temporal change that occurs is the ΔR that is presented in the equation (3.26). The derived form from the above analysis is given as:

$$\begin{aligned}\gamma_{Temp} = \exp\left[-\frac{2\pi^2}{\lambda^2}\cdot\Delta x^2\cdot(\cos\alpha_T\cos\beta_T+\cos\alpha_R\cos\beta_R)^2\right]\\ \cdot\exp\left[-\frac{2\pi^2}{\lambda^2}\cdot\Delta y^2\cdot(\sin\alpha_T\cos\beta_T+\sin\alpha_R\cos\beta_R)^2\right]\\ \cdot\exp\left[-\frac{2\pi^2}{\lambda^2}\cdot\Delta z^2\cdot(\sin\beta_T+\sin\beta_R)^2\right]\end{aligned} \tag{3.32}$$

The bistatic configurations are distinguished as quasi-monostatic, nadir-looking and general bistatic configuration. The quasi-monostatic, as it has been presented previously, is when the transmitter and the receiver are located at the same azimuth. In this way it emulates a monostatic configuration, but transmitter and receiver differ in elevation angle only. In the nadir-looking configuration, the transmitter is at high elevation angle close to 90 degrees. Last, for any other configuration it is referred as general bistatic configuration.

In the next figure, the correlation coefficient is presented for all three bistatic configurations. In the first plot (a), the temporal change of the target is considered to be on the x-direction and in the second plot the temporal change occurs only in the y-direction. The parameters of transmitter and receiver positions are given in the Table 3-3 below.

Table 3-3: Calculation parameters

Parameters	Value
Satellite effective velocity	3953 m/s
Carrier Frequency	1602.5625 MHz
Signal Bandwidth	5.11 MHz
Integration Time	300 s
Satellite-to-Target Range r_{T0}	19284 Km
Wavelength	0.187 m
Receiver Azimuth Angle	90 deg
Receiver Elevation Angle	5 deg
Quasi-monostatic transmitter azimuth	90 deg
Quasi-monostatic transmitter elevation	60 deg
Nadir-looking transmitter azimuth	50 deg
Nadir-looking transmitter elevation	85 deg
General bistatic transmitter azimuth	50 deg
General bistatic transmitter elevation	55 deg

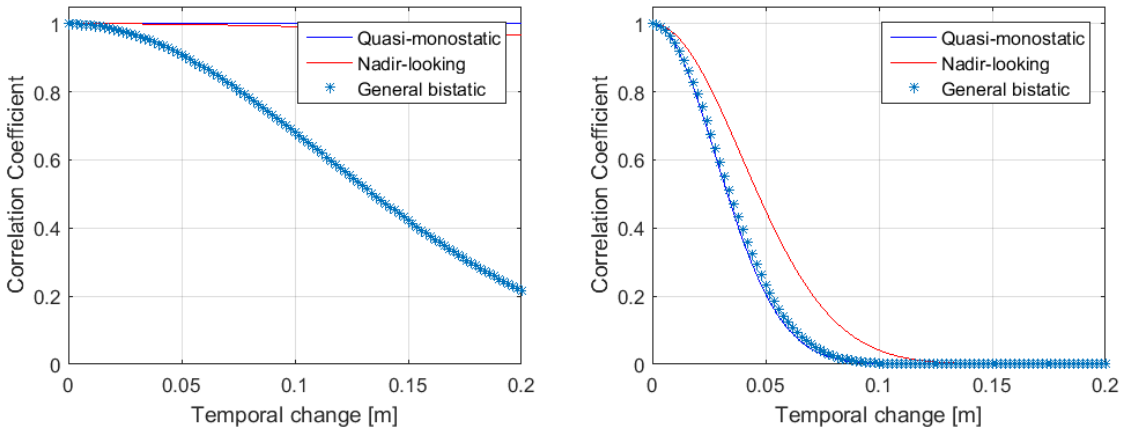

(a) (b)

Figure 3-11: Calculation results of temporal decorrelation in bistatic configurations for target temporal change in (a) x-direction (range), (b) y-direction (cross-range)

From the above figure we can observe that the correlation coefficient is more sensitive on the cross range target displacement. Although it can be easily expected to be the opposite, this is the correct because of the Point Spread Function properties in GNSS-based SAR.

The above analysis can be validated at this point with Monte Carlo simulations. It is assumed that a set of 1,000 scattering centres are located randomly within a resolution cell. Changes in the scattering centres were added and the corresponding image signal s_2 was calculated in the same way. The correlation coefficient between the two images was then calculated directly using equation (3.2). This process was repeated 1,000 times to get the ensemble average. A comparison between the simulated and theoretical results for the general bistatic configuration is shown in Figure 3-12 below. It can be seen that the simulation result is in agreement with the theoretical derivation. Any difference between simulated and theoretical results is accredited to the truncated impulse response used in the simulations. This is not a special problem in BSAR, and has also been encountered with monostatic SAR data [48].

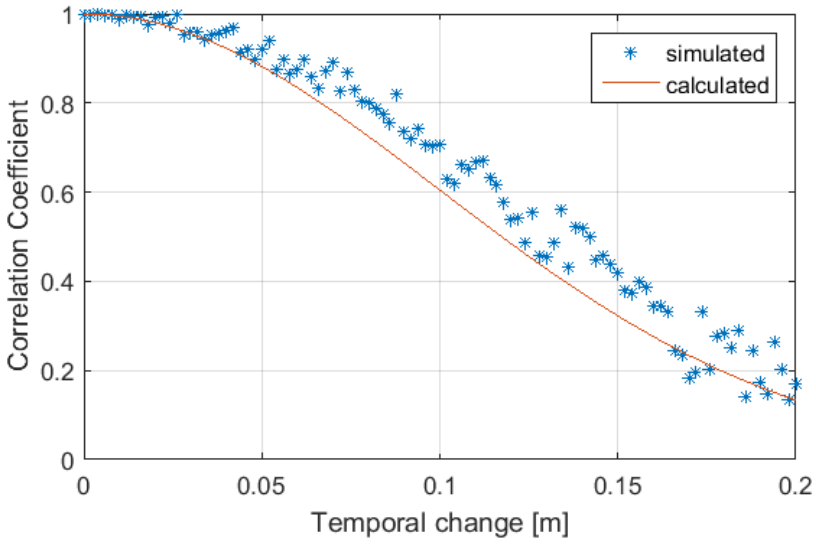

Figure 3-12: Simulation result of temporal decorrelation effect in general bistatic configuration for target temporal change in the range direction (x-axis)

3.6. Conclusions

In this chapter the Coherent Change Detection analysis has been presented. The properties of GNSS-based SAR image are presented. The image properties will be considered in the image processing for the Coherent Change Detection in the next chapters. The definition of coherence in an imaging radar is presented and the acquisition of an image pair for coherent processing with the use of GNSS-based SAR is explained. With GLONASS revisit period to be 8 sidereal days, experimentation becomes a long-term process.

In addition, the coherence calculation formula is explained and the factors that affect it are presented. The received signal components and parameters are presented. The connection of their effect on the coherence is explained along with the factors that affect the coherence. There are three major factors that affect the coherence in an image pair, the thermal, the spatial and the temporal factors. All three are explained and the decorrelation analysis for each of them is presented. The analysis is followed by simulation confirmation.

In the next chapter, the experimental program designed for the experimental confirmation of the temporal decorrelation factor study is presented.

Chapter 4 Experimental Program for CCD

4.1. Introduction

In this chapter the experimental program designed for Coherent Change Detection of a real target is explained. The aim of the study is the estimation of temporal changes with the use of coherence processng. However, coherence is affected not only from the temporal changes, but from thermal and spatial effects. Thus, for better evaluation of CCD's feasibility and performance in "ideal" experimental conditions, we try to design our experimental campaign in that way to minimise those two effects.

In order to minimise the thermal decorrelation, a strong reflector is needed. The signal from a strong reflector will provide higher power signal at the radar antenna input. Also, the stability during the repeat acquisitions is achieved by using the same configuration, as for the antennas, cables, connectors and generally the connections on the receiver system.

Regarding the spatial factor, it has more geometrical nature. Although the resolution of the GNSS-based SAR is not as high as active SAR systems, it can be very sensitive to geometrical changes depending on the data acquisition geometry [50]. The spatial decorrelation is affected by two parameters. The first one is the position of the receiver antennas and the second is the satellite trajectories at each measurement. The stability of both decreases the effect of spatial decorrelation.

With the minimization of the thermal and spatial effects, conditions closest to "ideal" can be achieved. The temporal decorrelation then can be studied on the feasibility and the performance over a real scene with real target conditions.

4.2. Experimental campaign methodology

An experimental campaign is designed for GNSS-based SAR Coherent Change Detection. The point to investigate is the ability of change detection in a scene using GNSS-based SAR. This is a proof of concept study, where we try to understand experimentally if this is fundamentally possible. The change that is under the investigation does not refer to total appearance or disappearance of targets in the observed area, as this is not CCD. CCD deals with small target changes that are comparable to the wavelength (approximately 20 cm in this study) of the signal used in the system.

In order to study the above point, a scene, a target and temporal change are needed. These are connected because this experimentation demands time and accuracy. Generating a set of images acquired over the same scene using a GNSS-based SAR system can take long time. The main reason is the revisit time period of GNSS used. GLONASS constellation that is used in this study has a revisit period of 8 sidereal days. Thus, the scene was selected to be in the surrounding area of the Electronic Electrical and System Engineering (EESE) building in the University of Birmingham campus.

Experimental stability over the repeat satellite pass acquisitions is essential for the spatial decorrelation factor minimization. The stability for the receiver's antenna positioning can be provided from the existing infrastructure on the roof of the EESE building. A rail with a carriage can provide the needed mounting for the radar antenna. The antenna is mounted on a metal pole and the position is marked. In the following figure the carriage on the rail and the radar antenna mounted on it are shown.

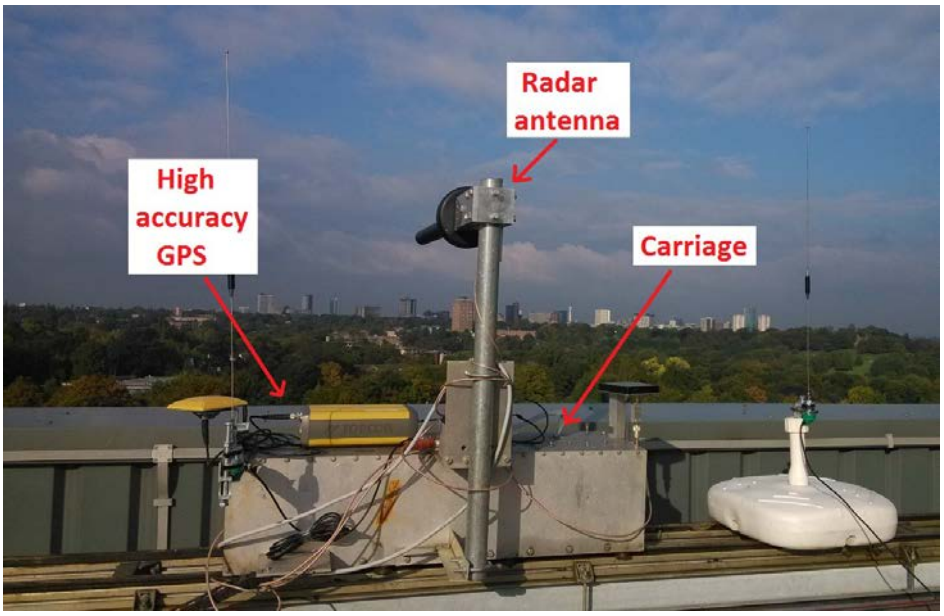

Figure 4-1: Carriage and radar antenna

4.3. Experimental configuration

Since the duration of the study was a matter of months, one of the most important criteria that needed to be satisfied was that the position and the setup of the antennas, in such a way, can be re-mounted without errors. The successful re-mount with the least possible errors is fulfilled by measuring and marking the position of the carriage and the antenna on the supporting pole at each experiment. This was because the equipment used is made for research and it is not totally weather-proof. Each acquisition required the mounting and unmounting of the antennas. The radar antenna was positioned on the rail carriage. The heterodyne antenna, which is used for the direct signal collection, was placed on the floor of the roof. A top view of the roof area and the positions of the antennas are shown in the figure below.

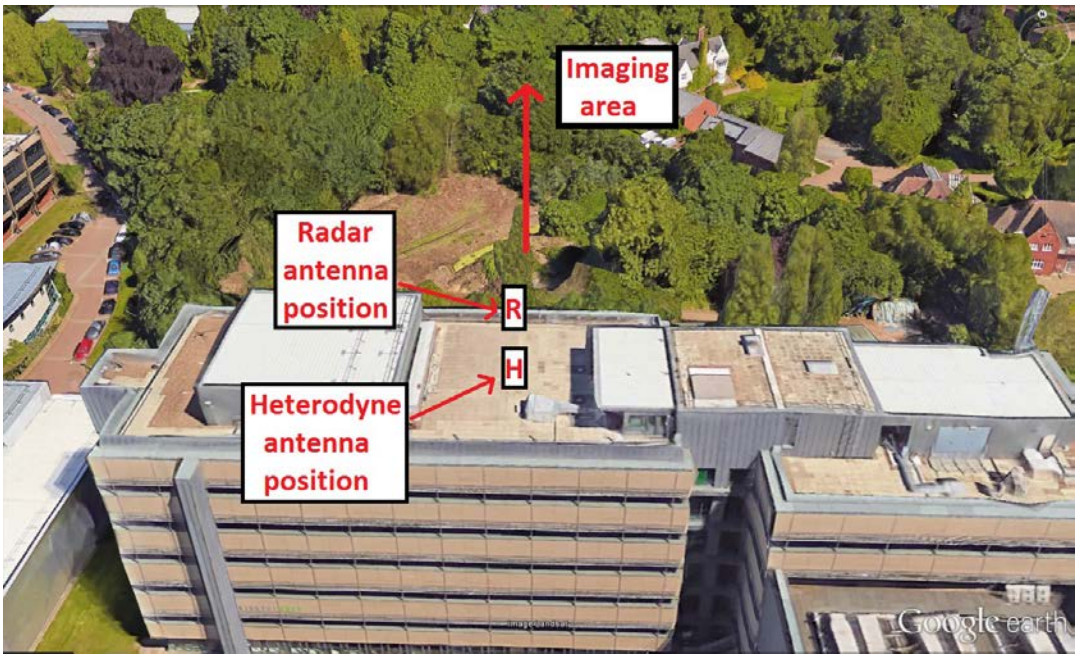

Figure 4-2: Roof area and antenna positions

With the radar antenna mounted on the carriage, the access to a scene is to the north of the building. This scene in view consists of buildings surrounded by big trees. A strong reflector is needed for the minimization of the thermal factor. Corner reflectors cannot be used, due to the unpredictable bistatic scattering. For this reason we choose in-scene targets. The existence of a building block that is isolated from many other targets can provide the desirable target for the purposes of the experiment. It is isolated and in images acquired it has a strong signal return. The scene in view is presented in the following picture. Also, an enlarged view of the building block that is the target used in the study is given in the Figure 4-4.

Figure 4-3: Observed area and position of target of interest

Figure 4-4: Enlargement of the target of interest (building block)

Having created the equipment setup, and also after having checked the available scenery and the possible target in the observed area, the experimental program moves forward to the next stage. The next stage is the selection of a satellite. The selection of the satellite position is important because it defines the resolution of the system and the spatial decorrelation effect. As it has been explained in chapter 2 on the PSF analysis, the position and the direction of the movement of the satellite affect the PSF resolution and orientation. The desired satellite trajectory for best range resolution, is when it is using a Quasi-monostatic configuration. In this case it means to have the satellite moving in the East-West direction and being in the south of the receiver.

However, since the experiments are conducted in the UK, the available satellites for the experiment do not satisfy the quasi-monostatic configuration. This happens due to the fact that the orbits of the satellites follow a pattern of orbits. This pattern is shown in the figure below.

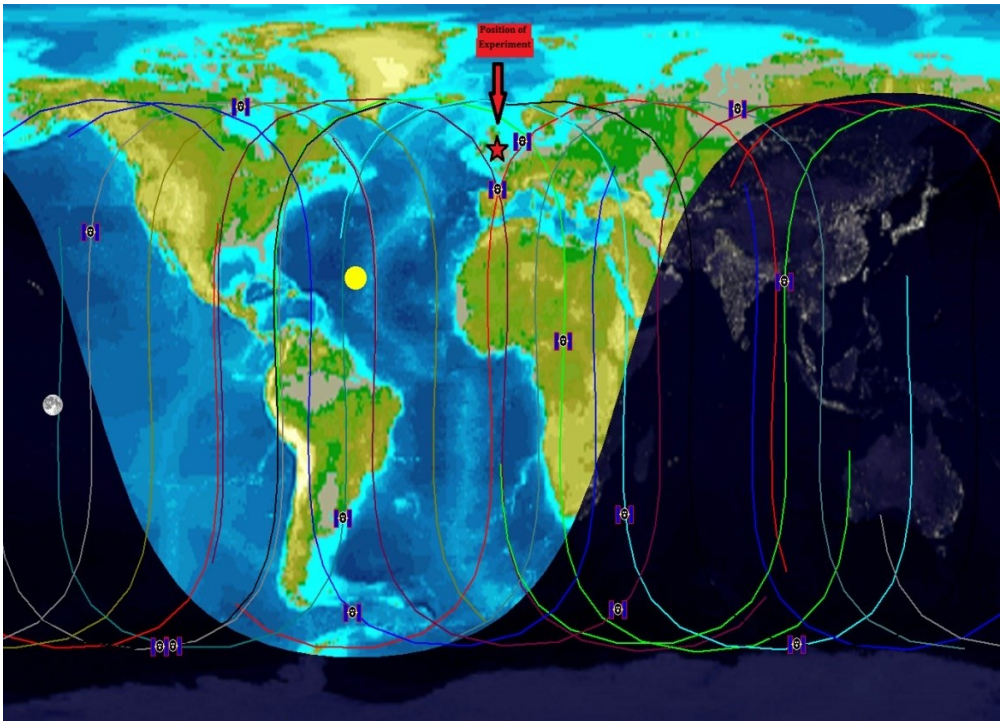

Figure 4-5: Available Satellite orbits

Thus, a simulation for the PSF characteristics is done for all the GLONASS satellites in view for a period of 8 days, to cover all the positions until the revisits start. After performing the simulations for the PSF resolution for all the satellite positions, the one that provided the best resolution was moving from North-to-South at the east of the receiver. The selected satellite trajectory is shown in Figure 4-6. Although the experimental parameters will be presented later, we can mention here that the position of the transmitter at the beginning of the measurements was at azimuth 93 degrees and at 54 degrees elevation.

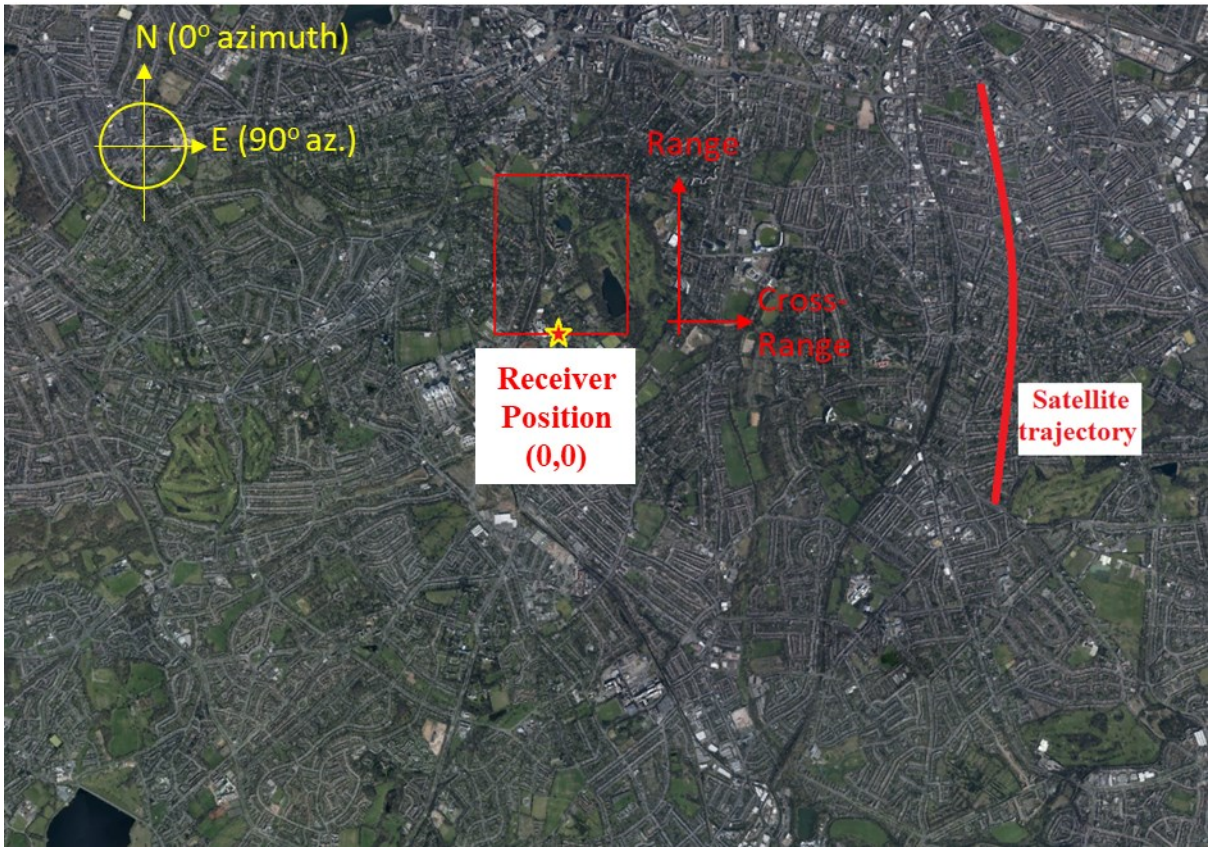

Figure 4-6: Selected Satellite position

Let us consider again the bistatic topology of the system. The transmitted signal from the satellite is collected from the heterodyne antenna for synchronization. From the radar antenna

we use the signal reflected from targets to create the image. For simplicity let us consider that there is only one target in the scene under the investigation (building block).

In the scenario of the target displacement by a small distance *dr*, the reflected signal is going to follow the dotted line (

Figure 4-7). The delay of the reflected signal with the displacement is going to be different from the initial condition. This delay is going to create a phase difference between the two received signals that are reflected from the target. If we represent the above explanation with equations, it will be:

$$s_1 = A_1 \exp\left[-i\frac{2\pi}{\lambda}R_1\right] \tag{4.1}$$

$$s_2 = A_2 \exp\left[-i\frac{2\pi}{\lambda}R_2\right] \tag{4.2}$$

where s_1 and s_2 are the received signals from the target, with $s_1$to be the initial condition and s_2 to be the signal after the displacement, and

$$\begin{aligned} R_1 &= R_{transmitter-target} + R_{target-receiver} \\ R_2 &= R'_{transmitter-target} + R'_{target-receiver} \\ R_2 &= R_1 + \Delta r \end{aligned} \tag{4.3}$$

Therefore, the phase difference between the two signals will be:

$$\Delta\varphi_{1,2} = e^{-j\frac{2\pi}{\lambda}\Delta r} \tag{4.4}$$

If the target can move, there is the possibility of displacement to any direction, *dr = dr(x)* (range) or *dr = dr(y)* (cross-range) or even a combined one *dr = dr(x,y)*. Because of the bistatic configuration we have to take into consideration that $dr \neq \Delta r$ where *dr* is the target displacement and Δr corresponds only to the absolute range difference.

Since the selected target for the experiments is a block building and cannot be moved, there should be a design so that the antenna can be moved to create the desired Δr. This is possible by moving the radar antenna instead. The reference (heterodyne) antenna will be kept on the same position but the radar antenna can be moved to create a Δr difference to the total transmitter-target-receiver range. In the following figure it is represented the radar antenna movement (B) equivalent of the target displacement (A).

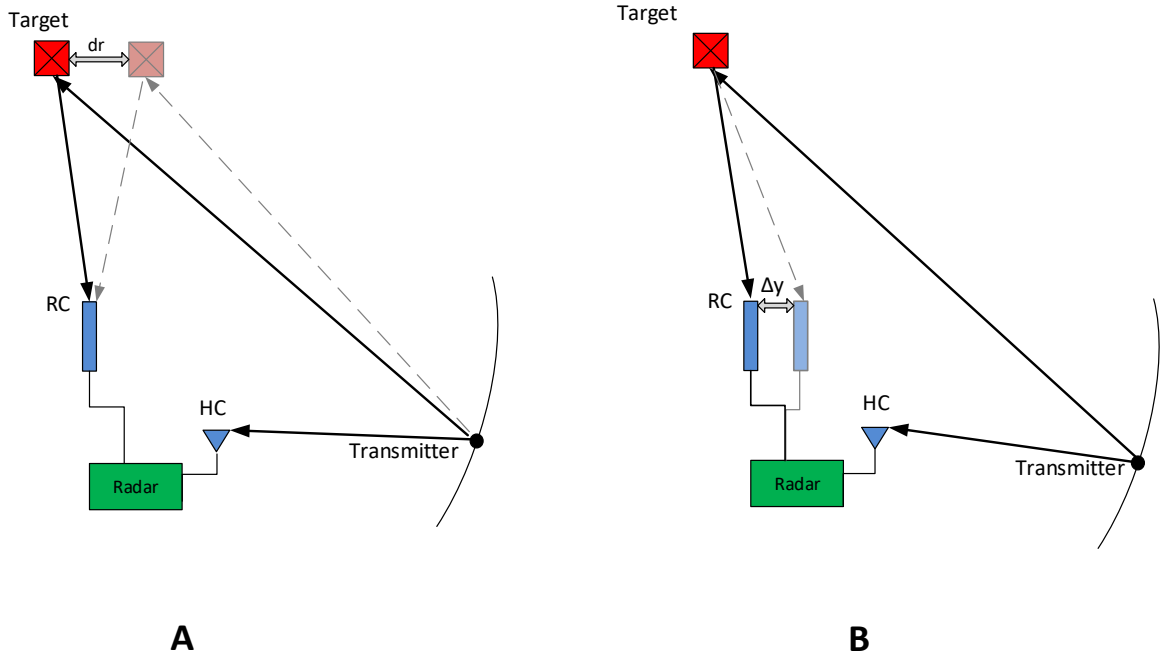

Figure 4-7: (A) Target displacement and (B) antenna movement equivalent

By creating a Δr with the movement of the radar antenna and keeping the reference antenna stable, we have the same reference signal/phase at the revisit of the satellite.

4.3.1. Parameter definition

Having prepared the experimental configuration, there is also the need of defining some parameters. First of all the system specifications are given in the table below.

Table 4-1: System specifications for experimentation

Parameter	***Value***
Satellite used	GLONASS Cosmos 744
Satellite position	Elevation: 54 deg || Azimuth: 93 deg
Bistatic angle	85 deg
Nominal revisit cycle	8 sidereal days
Carrier frequency	1604.8125 MHz
Ranging code bandwidth	5.11 MHz
Wavelength	0.1868 m

Apart from the system specifications, we need to define also the distance variation of the radar antenna position. In order to assess the capability to detect changes as well as the performance, we are ranging the shift by different amounts. The shift is chosen to be of the values:

- λ/4
- λ/2
- 3λ/4

A shift equal to one wavelength in a system with such a resolution (~30 meters in range and 5 meters in cross-range) will not result in low correlation as it will do in a system with very high resolution (active SAR). In the case a shift of one wavelength occurs, the target will be

still in the same resolution cell. Calculating the temporal correlation coefficient from equation (3.32) is given as:

$$\gamma_{Temp} = \exp\left[-\frac{2\pi^2}{\lambda^2}\cdot\Delta x^2\cdot(\cos\alpha_T\cos\beta_T+\cos\alpha_R\cos\beta_R)^2\right]$$
$$\cdot\exp\left[-\frac{2\pi^2}{\lambda^2}\cdot\Delta y^2\cdot(\sin\alpha_T\cos\beta_T+\sin\alpha_R\cos\beta_R)^2\right]$$
$$\cdot\exp\left[-\frac{2\pi^2}{\lambda^2}\cdot\Delta z^2\cdot(\sin\beta_T+\sin\beta_R)^2\right]$$

We can see from the above equation that the correlation coefficient depends on the $\Delta x^2/\lambda^2$. Important point here is that the movement of the radar antenna will occur on the cross-range direction, due to the orientation of the rail where the radar antenna was mounted. A calculation is needed to provide the respective sideways movement of the radar antenna.

Taking into account the positions of the transmitter, the target and the receiver we can calculate the movement of the radar antenna (dy) to create the desired Δr. Also, since the target is fixed and the transmitter is on revisiting trajectory, we consider the distance between transmitter-target to remain the same. Thus the only distance that is affected is the target-receiver distance. The position of the target in the observed area is about 680 meters range and 40 meters azimuth (the minus shows direction). Using just Euclidean geometry for non-right angle triangle we can estimate the dy antenna shift to achieve the desirable Δr for the Equation (4.4). The calculation gives us that for each λ/4 we need to move the radar antenna by 1 meter. So the positions of the antenna to create the Δr needed are as below (minus shows direction):

- $\Delta r = \lambda/4 \rightarrow dy = 1$ meter
- $\Delta r = \lambda/2 \rightarrow dy = 2$ meters

- $\Delta r = 3\lambda/4 \rightarrow dy = 3$ meters.

Summarizing, acquisitions will be done for four radar antenna positions in total and they are the initial and three more that are mentioned above. Also, at each position more than 2 measurements are needed and this is for stability check and averaging techniques.

4.3.2. Factors affecting the system and CCD performance

The performance of the Coherence Change Detection can be affected by several parameters. Using the experimental program that is described above we can minimize the effect of the thermal and spatial decorrelation factors. For the thermal factor, a strong reflector target is chosen and the same antennas, cables and all components are used at each acquisition. For the spatial factor, the antennas are re-mounted with accurate positioning for each acquisition, but there is one more point to be taken into account for the spatial factor.

Timing of data acquisition is essential for the minimization of spatial decorrelation effect. Acquiring the data with even a second earlier or later introduces spatial decorrelation. The azimuth and the elevation angles of the satellite are time dependent, and for this accurate timing is needed. The UTC time at the Prime Meridian is the reference clock for the acquisitions. Although it might be difficult to have all the equipment clocks always synchronized to the UTC time, the corrections were done before each measurement on the local clock. Also after each acquisition, the local clock was compared again to the UTC time. The data are acquired for period larger than the duration needed, and then the data is truncated before the processing.

In addition, another source of spatial decorrelation is the satellite trajectory turbulences. Errors to the trajectory of the satellites occur all the times, but this is something we cannot

control in the experimental setup. However, the turbulences are considered to be of very small duration and amount and in a long integration measurement they can be neglected.

The scintillations in the ionosphere are removed at the image formation stage, where the range compression is done. The matched filtering between HC and RC channels remove the scintillations in one acquisition. The long range between transmitter-receiver compared to the target-receiver range make efficient the removal of the atmospheric propagation errors and scintillations. In addition, due to the location of the experimental program (North Europe) the ionospheric scinttilations are less probable than in areas near the equator or to the poles of the Earth.

Last but not least, the antennas used on the HC and RC channels are narrow beam and wide beam, respectively. However, the received signals, direct satellite signal and target reflected signal, are received in the middle of each antenna's main lobe.

The experimental program is designed to minimize the above mentioned factors that affect the CCD performance. Nevertheless, an overall decorrelation level due to them is expected to be within the limit of maximum parameter decorrelation of 0.05 to 0.1, meaning that the average expected decorrelation, when no target displacement has occurred, to be $\gamma > 0.95$.

4.4. Data Acquisition

Since the transmitter is in motion, the images that are produced can be different even after a very small period of time (e.g. 2 minutes) and the PSF orientation changes. At the initial acquisition we acquired a number of images. Having the initial image, the timetable for the revisits is planned. The revisit of the transmitter satellite is 8 sidereal days and it corresponds to 7 days 23 hours 27 minutes and 28 seconds. Although many experiments were done, not

all were successful due to experimental conditions at the time of measurements. The successful measurements are shown in the table below.

Table 4-2: Dates and times of successful measurements for target CCD

Date	Time	Synch (sec)	Δr	Image No
02/12/2014	17:17:18	237	0	01
10/12/2014	16:44:46	237	0	02
18/12/2014	16:12:14	237	0	03
27/01/2015	13:29:34	237	λ/4	11
04/02/2015	12:57:02	237	λ/4	12
12/02/2015	12:24:30	237	λ/4	13
20/02/2015	11:51:58	237	λ/2	21
28/02/2015	11:19:26	237	λ/2	22
08/03/2015	10:46:54	237	λ2	23
16/03/2015	10:14:22	237	0	04
01/04/2015	9:09:18	237	λ/4	14
17/04/2015	8:04:14	237	λ/2	24
12/06/2015	4:16:30	237	3λ/4	31
28/06/2015	3:11:26	237	3λ/4	32
06/07/2015	2:38:54	237	3λ/4	33

The dates and times correspond to the acquired and processed data. The acquisitions were starting some time before the above shown timestamps to ensure that the complete set of needed data was recorded. The integration time for each image created is 237 seconds despite the total acquisition time. The needed data were in the middle of each dataset and then truncated. This helped in reducing timing errors for the spatial decorrelation.

On the last column of the table above, we have the image number. The image number consists of two digits. The first digit corresponds to the radar antenna position and the second digit refers to the number of the acquisition for the specific antenna position. For example, the image number 01 means that this is the image acquire at the initial position where $\Delta r = 0$

and it is the first image acquired with the radar antenna on this position. In the same way the image number 23 refers to radar antenna position with applied $\Delta r = 3\lambda/4$ and it is the third image acquired at this antenna position. This helps understand easier the processing the images in pairs later before any image is cancelled out for any reason.

4.5. Stages of processing

The acquired data each time, are cropped and processed. For the cropping of the data, the clock of the receiver is compared to the UTC time and any time drifts are removed. The first stage of processing, as it has been mentioned, is the synchronization. Also a stage of fine cropping occurs during the simulation process. The result of the synchronization confirms the correct cropping of the data for the revisit pass of the satellite. This is for the minimization of the spatial decorrelation effect.

After the synchronization part is complete, the image formation algorithm is applied. The image formation is applied on both the heterodyne channel (HC) and the radar channel (RC). The image that is produced from the HC gives us the PSF of the acquisition, as it emulates a single point target located at position (0,0). The RC gives us the image of the observed area. Thus, we have two images for each measurement.

The comparison of the images is done in pairs. Firstly, we can compare the Point Spread Function of every acquisition to compare coherence between the measurements, for stability estimation This can be done, since the reference antenna is not moved from measurement to measurement. Since the reference channel is not used for direct temporal decorrelation detection, it can be used for the Coherence calculation between revisits of the transmitter satellite and also for the estimation of the effect of spatial decorrelation that occurs.

After calculating the correlation coefficient for the direct signal channel images, we move on to the radar channel images. The radar channel is illuminating a large area and the target area needs to be cropped out for processing. Other targets cannot be used for the calculation of the temporal change because the antenna movement was calculated only for the specific target. Targets at different range and cross-range positions will not have the same Δr as the target under the investigation selected at the experimental design. When the target under the study is cropped and isolated it is considered as the image of the RC for processing. A rotation stage is needed after the cropping too. As the orientation of the PSF is not on zero degrees neither on ninety degrees, the target image is rotated to the range axis or to the cross-range axis (on the range axis in this study). As it has been mentioned before in the chapter, the processing is done using averaging window that is rectangular and the longer side is parallel to the range resolution of the PSF.

With the images cropped and rotated, the calculation of the correlation coefficient (coherence) is calculated. The images are processed in pairs. For each pair, the correlation coefficient is calculated for each pixel. The value of each pixel is averaged by the neighboring pixels. Calculating the correlation coefficient for all the pixels of the target image pair, then the mean value of these calculations define the coherence level between the two images. We can sum up the stages of processing in the next figure.

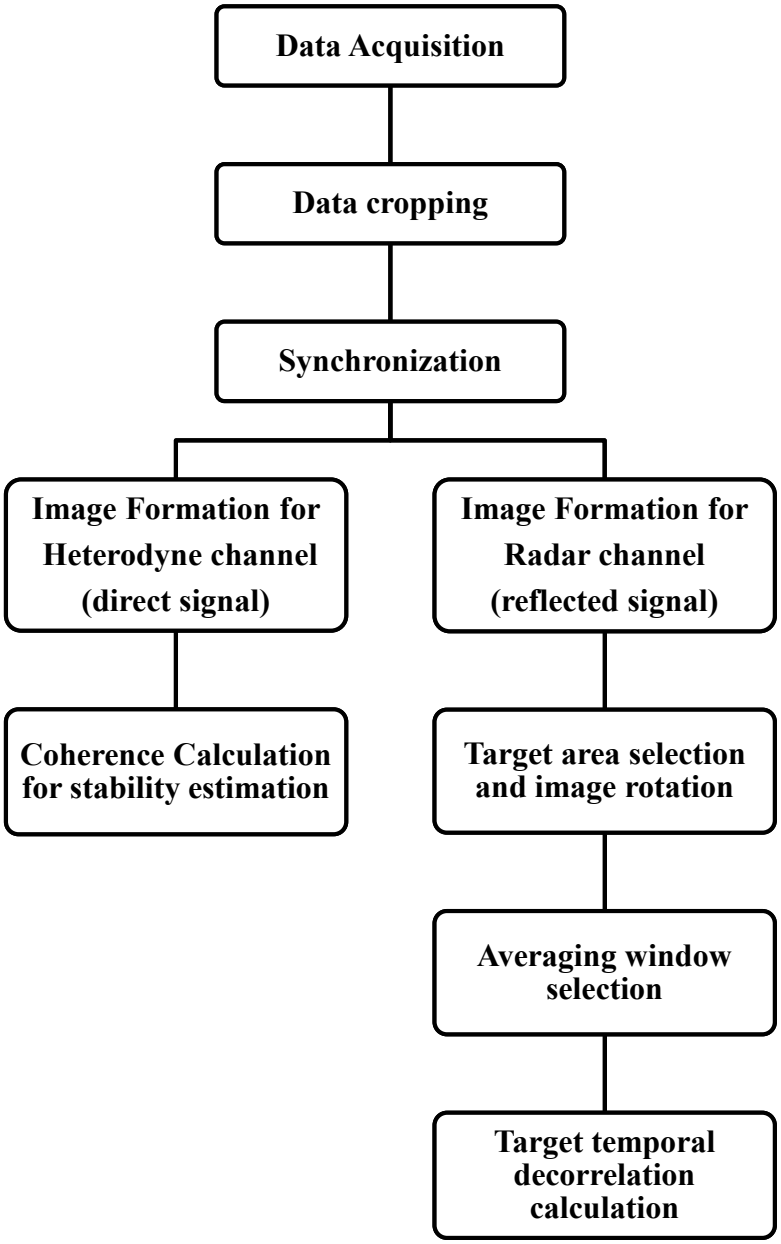

Figure 4-8: Stages of processing (block diagram)

4.6. Data Evaluation

Evaluation of the data occurs in two stages of the processing. The first evaluation takes place after the synchronization and the second is after the spatial coherence calculation. The synchronization needs to provide the expected results for the Doppler shift, the phase, the delay and the signal spectrum of the signal. Along with the navigation message, these are the needed data for further processing. However, the navigation message is expected to be different at every acquisition. The navigation message consists of information about the time and constellation information for Global positioning purposes (Navigation satellite). The second stage of evaluation occurs after the spatial coherence calculation. When the PSF for the measurement is created, it is compared coherently to the primary PSF. The coherence coefficient shows the level of the coherence and the coherence map for the comparison is created. The two evaluations combined confirm the correct processing and provide the coherence level of each image pair, which is taken into account in the target coherent change detection.

4.7. Conclusions

In this chapter the experimental program for Coherent Change Detection has been described. For the study of the temporal decorrelation and coherent change detection, the experimentation holds a great importance. The importance of the experimental accuracy is analysed and the factors that affect the experiments are explained. Decided solutions and methods for best performance and accuracy are shown. The experimental configuration is analysed and the parameters are explained. The methods used for the minimization of the thermal and spatial decorrelation effects are described.

The data acquisition was a long term plan. Experimental conditions occur and they extend the total duration. The parameter that affects most is the long satellite revisit interval that is 8 sidereal days. Accurate calculation of the revisit day and time was done and the experiments were conducted whenever the satellite was in the revisit position. The weather conditions affected the experimentation, since the equipment used is developed for research and not as a commercial product with waterproof specifications.

Processing the acquired data is the next part that will provide the results. The stages of the data processing are explained and the results of that processing will be presented in the next chapter.

Chapter 5 CCD experimental results and analysis

5.1. Introduction

In this chapter the experimental results and the analysis of them are presented. The output image from each acquisition is used in two ways, as an individual image and also as a component of an averaged image. Coherent Change Detection methods that are widely used are presented and the results are compared to the theoretical value.

5.2. Averaging and coherence

Coherent Change Detection relates to radar interferometry. In interferometry, averaging is used for two reasons. First reason is because averaging removes any speckle noise that occurs during the acquisition. The second reason is that averaging is used to increase the signal to noise ratio. In our case, the produced radar images denote statistical values, since the resolution cell covers a rather big area.

In order to calculate the coherence between two images, a small area covering a number of image pixels is averaged. This area is measured in resolution pixels, where for the PSF is set to 9 pixels (square shape, three-by-three pixels), the smaller the area, the more sensitive. Thus, a small area is used for the PSF coherence calculation. For the target coherence calculation the case is different. The averaging window is selected to be wider. The reason for this is the dimensions of the target that are greater than a point target. The target is spread over several resolution cells, approximately five PSFs area, and the averaging window is

expanded too. A rectangular window is selected because the shape of the PSF is ellipsoid. The ratio for the dimensions of this averaging window can be 1:3 to 1:4.

Since we refer now to the target returns, the coordinate system chosen is the local coordinates with point O(0,0) to be the position of the HC antenna (as shown in Figure 4-6).

5.3. Coherence of synchronization channel

The coherence for the synchronization channel (or direct signal) is expected to be very high. Since no change occurs on the direct channel, we can calculate the summation of the thermal and spatial decorrelation. The stability of the measurements on the satellite revisit is confirmed using this method as well. First, we compare the PSF acquired for the measurements on the initial position. These are shown in the figure below.

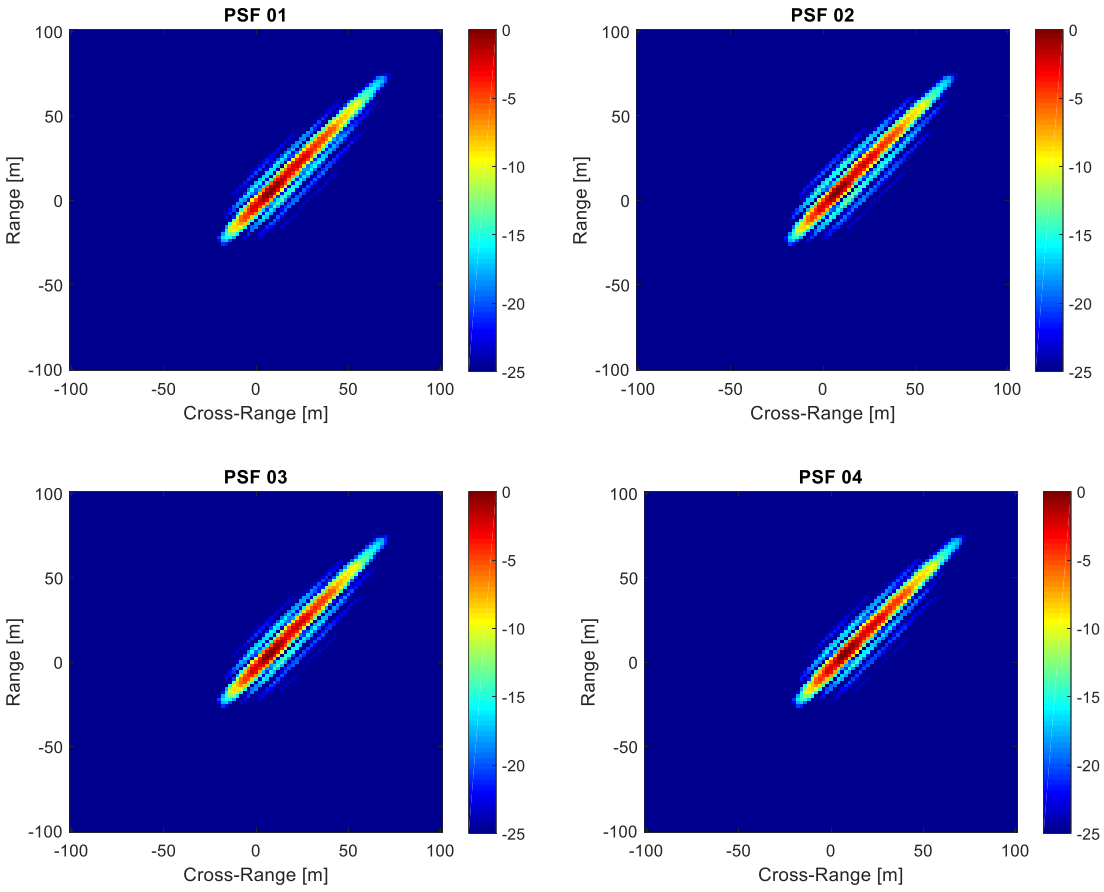

Figure 5-1: PSFs from acquisitions at the initial antenna position

Although the above images look very similar, a cross-correlation calculation for the coherence will provide a more detailed comparison.

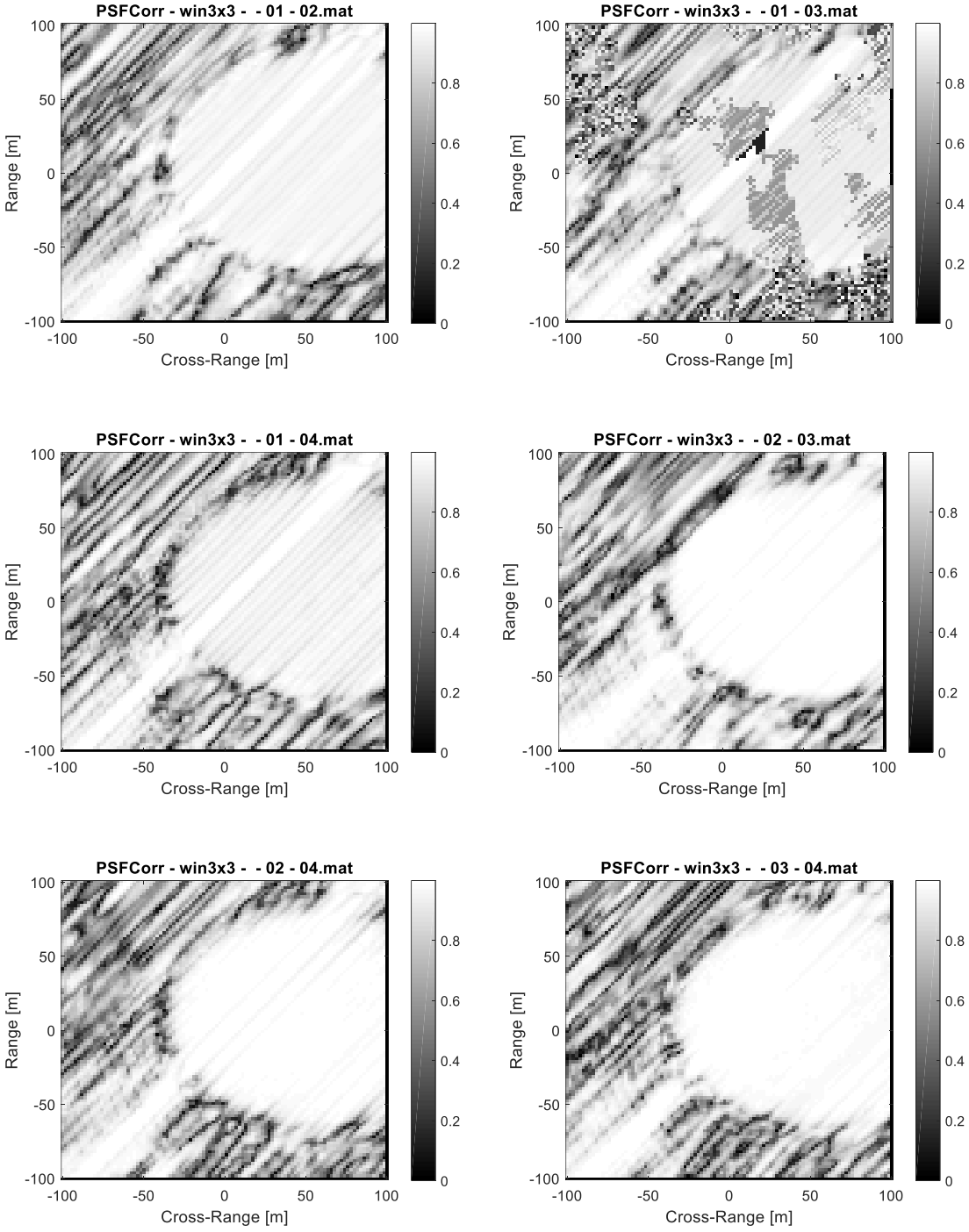

Figure 5-2: PSF coherence maps for initial antenna position

In the above graphs we see the coherence maps that are produced from the cross-process of the PSFs from the initial antenna position.

The process is done using the equation (3.2) , $\left(\gamma = \frac{\left| \left\langle s_1 \cdot s_2^* \right\rangle \right|}{\sqrt{\left\langle s_1 \cdot s_1^* \right\rangle \cdot \left\langle s_2 \cdot s_2^* \right\rangle}} \right)$, as mentioned before.

As we can see from the coherence maps above, the coherence level from all the measurements is high, as the area near the target return has values higher than 0.85 in average. Also we can observe that the area of high correlation is much bigger than the area of the PSF itself we see in the dynamic range of [-25 0] dB.

In the same way we compare the PSFs from the next measurements.

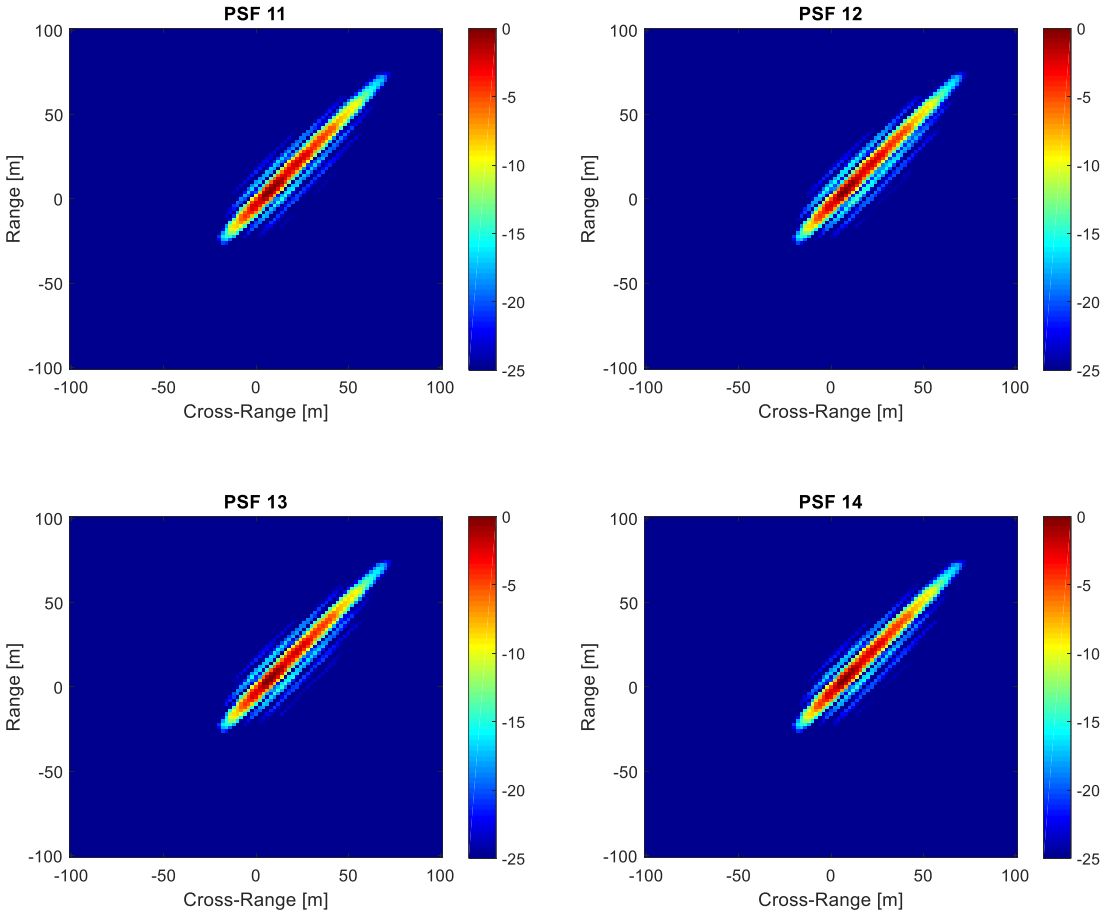

Figure 5-3: PSFs from acquisitions at antenna position $\Delta r = \lambda/4$

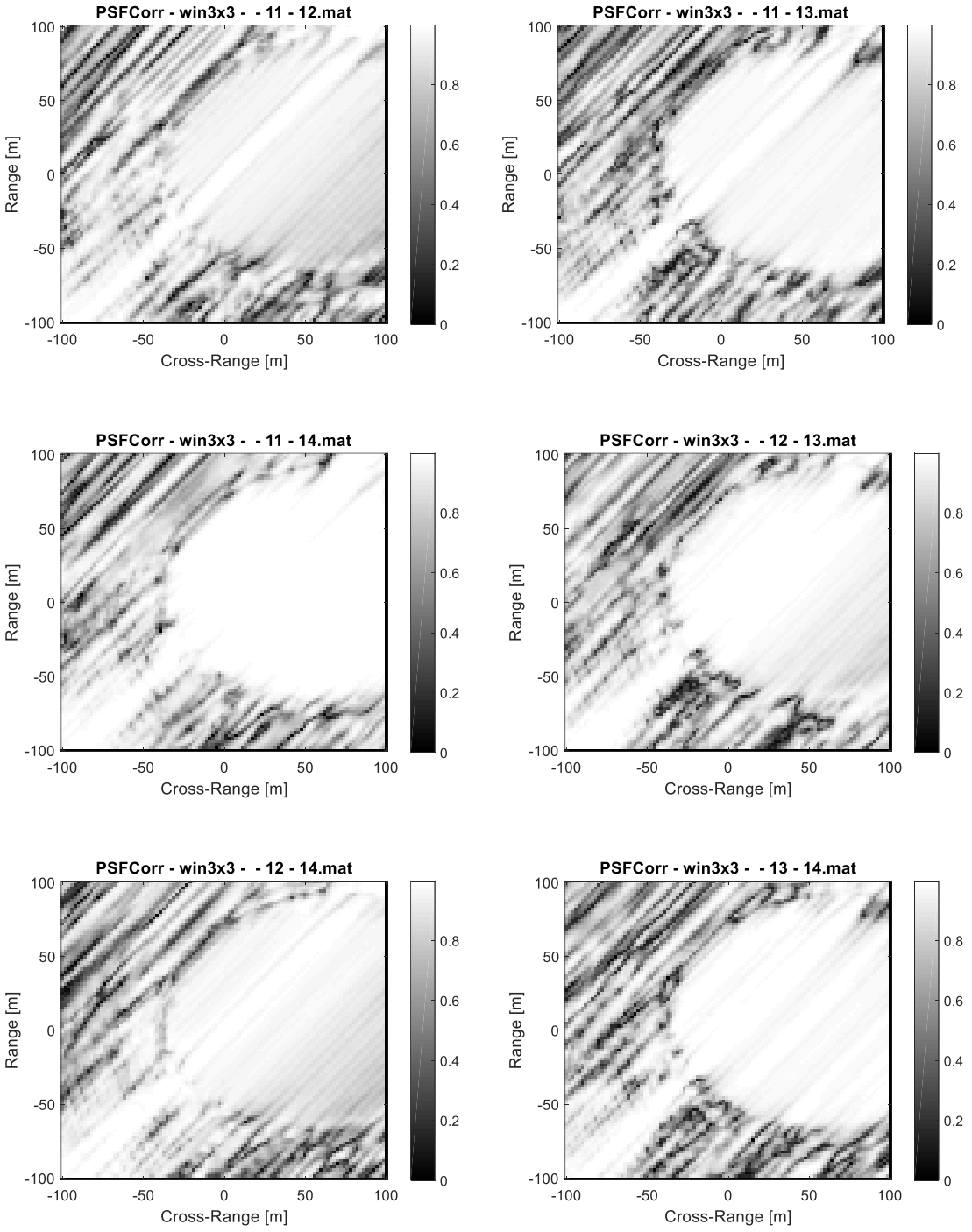

Figure 5-4: PSF coherence maps for antenna position with $\Delta r = \lambda/4$.

The PSFs for the next antenna position are given in the following figure. The coherence maps from the PSF comparison at this position are presented as well.

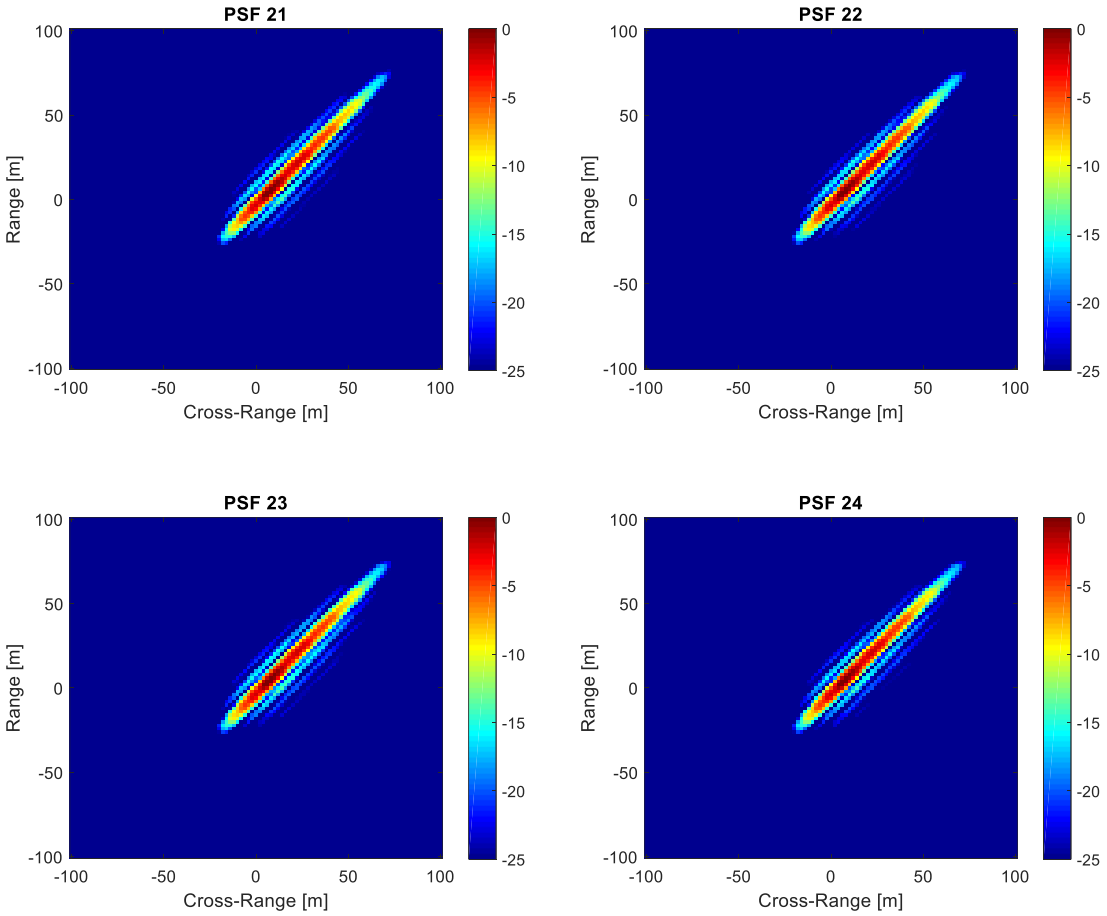

Figure 5-5: PSFs from acquisitions at antenna position $\Delta r = \lambda/2$

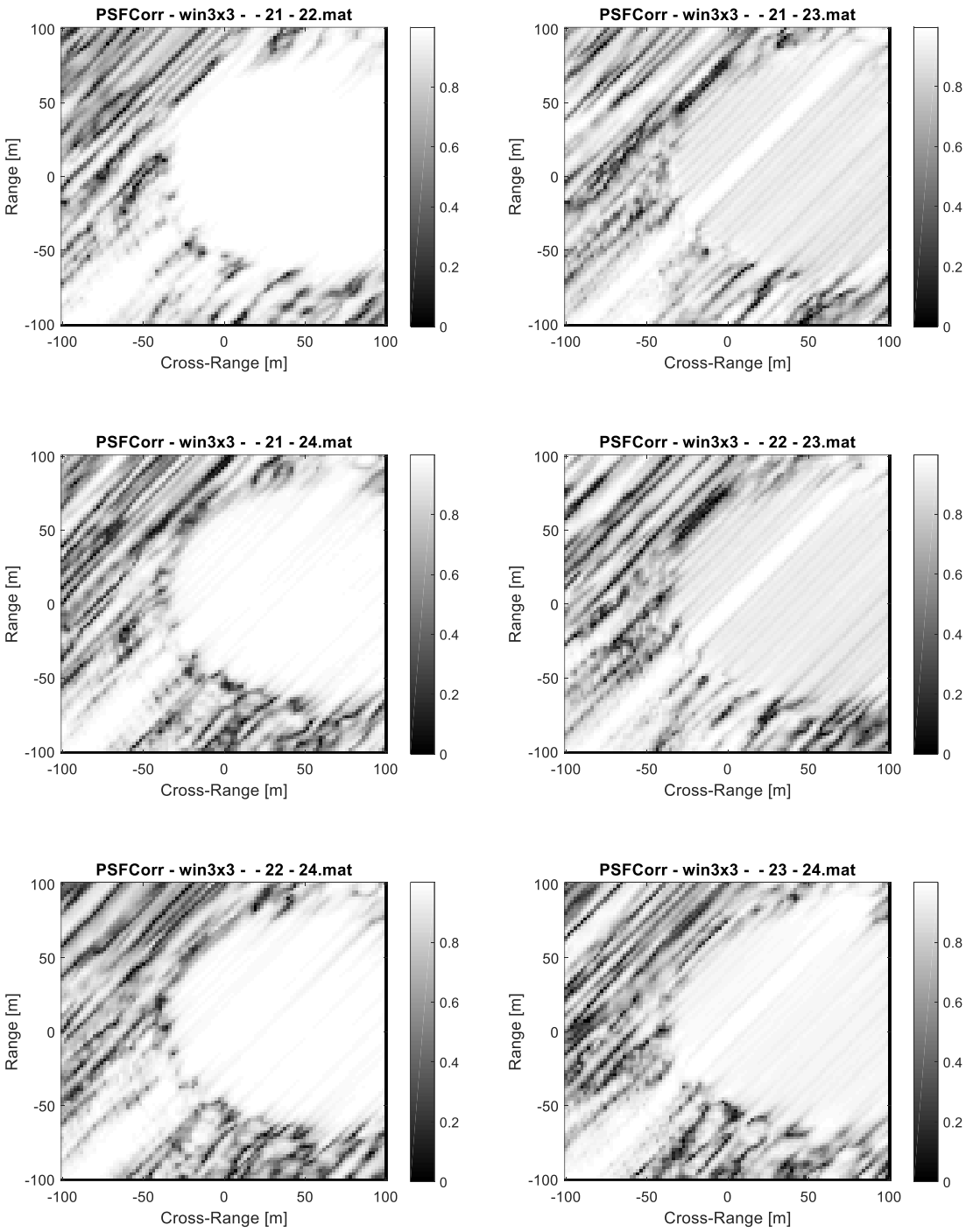

Figure 5-6: PSF coherence maps for antenna position with $\Delta r = \lambda/2$.

For the next antenna position there are only three measurements and the PSFs acquired are shown in the figure below.

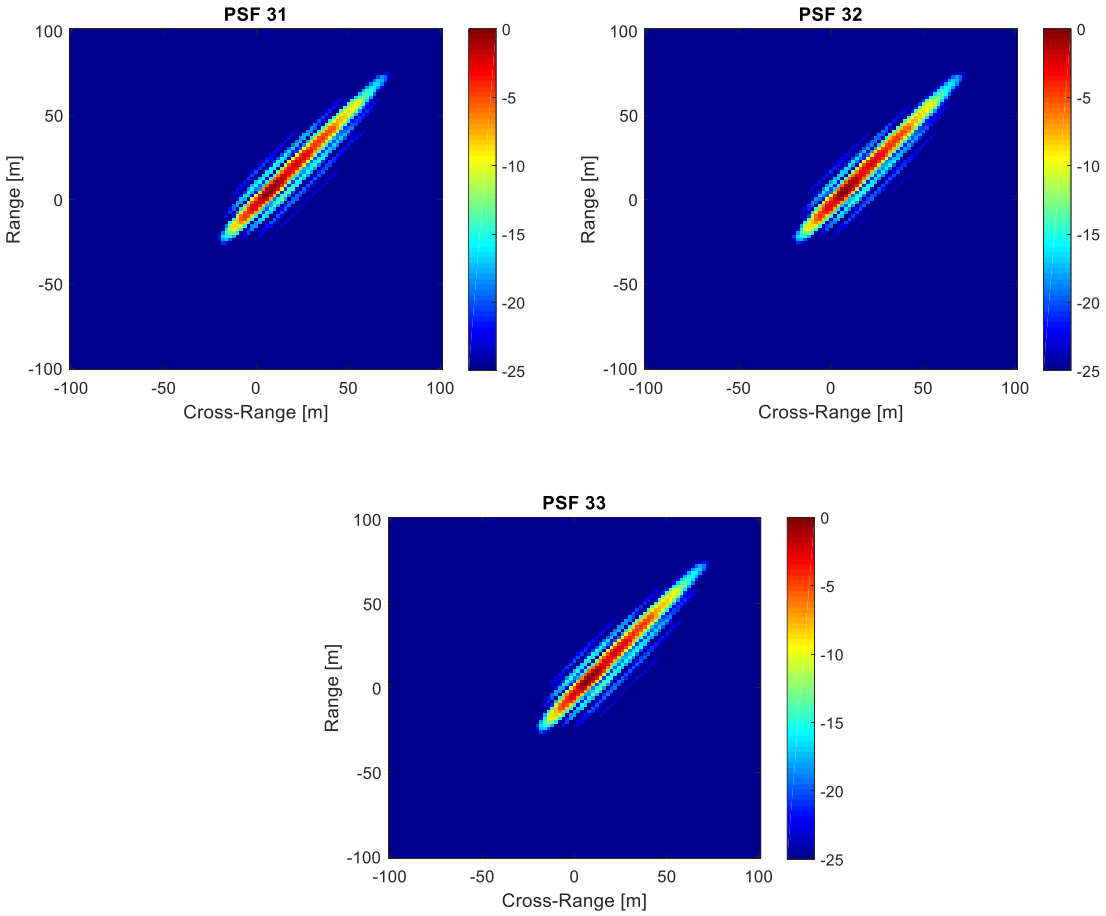

Figure 5-7: PSFs from acquisitions at antenna position $\Delta r = 3\lambda/4$

The coherence maps for the above PSFs are presented in the following figure.

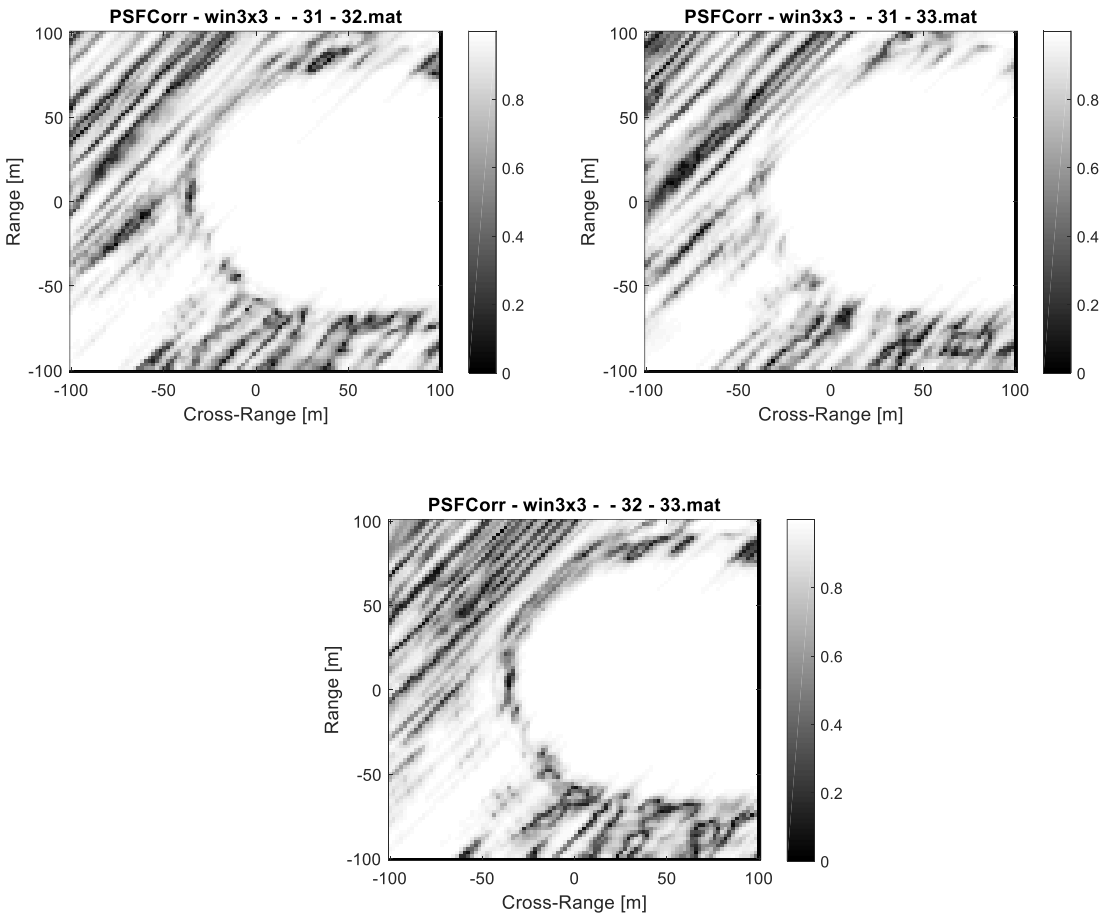

Figure 5-8: PSF coherence maps for antenna position with $\Delta r = 3\lambda/4$.

5.4. Non-temporal decorrelation

The decorrelation in the coherence maps that are shown in the previous paragraph is due to the thermal and spatial decorrelations that occur in the measurements. The coherence level is 0.96 as average. It is important to notice that the calculation of the coherence level has been done using very small averaging window. For larger averaging window, the coherence would result in higher levels. The individual results and mean values are presented in the following table.

Table 5-1: Mean PSF coherence

PSF Comparison	***Value***	**PSF Comparison**	***Value***
01-02	0.9505	11-12	0.9352
01-03	0.9148	11-13	0.9508
01-04	0.9375	11-14	0.9822
02-03	0.9667	12-13	0.9742
02-04	0.9765	12-14	0.9514
03-04	0.9637	13-14	0.9697
Mean	0.9516	Mean	0.9605
PSF Comparison	***Value***	**PSF Comparison**	***Value***
21-22	0.9905	31-32	0.9829
21-23	0.9071	31-33	0.9910
21-24	0.9668	32-33	0.9784
22-23	0.9012		
22-24	0.9654		
23-24	0.9537		
Mean	0.9474	Mean	0.9841

The above results are calculated for each PSF from a rectangular area that includes the close area around the PSF. This area is shown in the picture below.

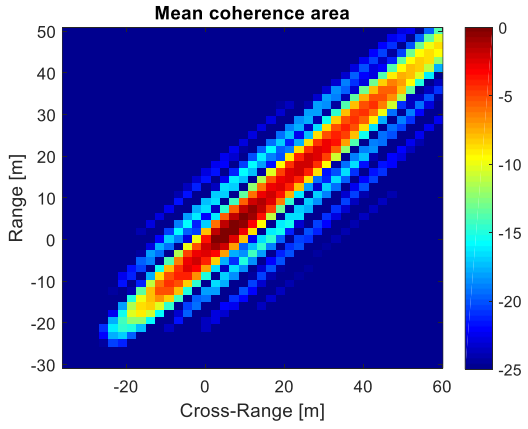

Figure 5-9: Mean coherence value area

From the table above it can be observed that the worst case for the average coherence level is 0.947. Also, the overall minimum coherence level is 0.9012, coherence that is still acceptable. Depending on the SAR system, coherence levels above 0.85 or 0.9 are considered acceptable. The overall average value of the coherence level is 0.9609. This result shows that the effects of the spatial and the thermal decorrelation remain low throughout the experiment, as well as all other parameters mention in paragraph 4.3.2.

Another observation that can be extracted is that the time is not affecting the coherence. For the stability of the measurements and the effect of the time on the coherence, the measurements we acquired in the order that is presented in the figure below.

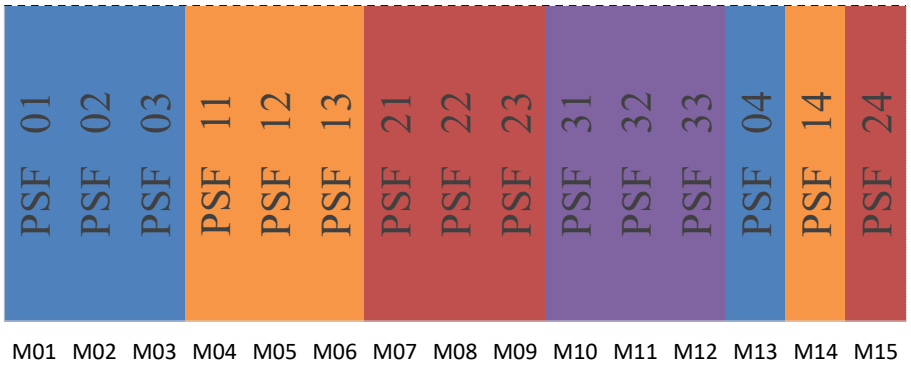

Figure 5-10: PSF stability time-plan

Due to the long duration of the experimental campaign, at the end of the experimental campaign, stability evaluation measurements were acquired for each position. However, it is important to mention again here that the direct signal antenna was not moved. For this reason we can compare each PSF to any other, and from the table above there is not any sign of coherence degradation over time.

5.5. Temporal decorrelation factor

In order to calculate the Temporal decorrelation factor we need to calculate the equivalent for the selected target in the scene. The scenery consists of several targets, as can be seen in Figure 5-11. The return from the target occupies area that is bigger than the point target return. In other words, the return from the target building covers bigger area than the PSF. An approximate estimation is a ratio of 3:1, where the target building is covering three times to the area a PSF (point target return) covers (Figure 5-12).

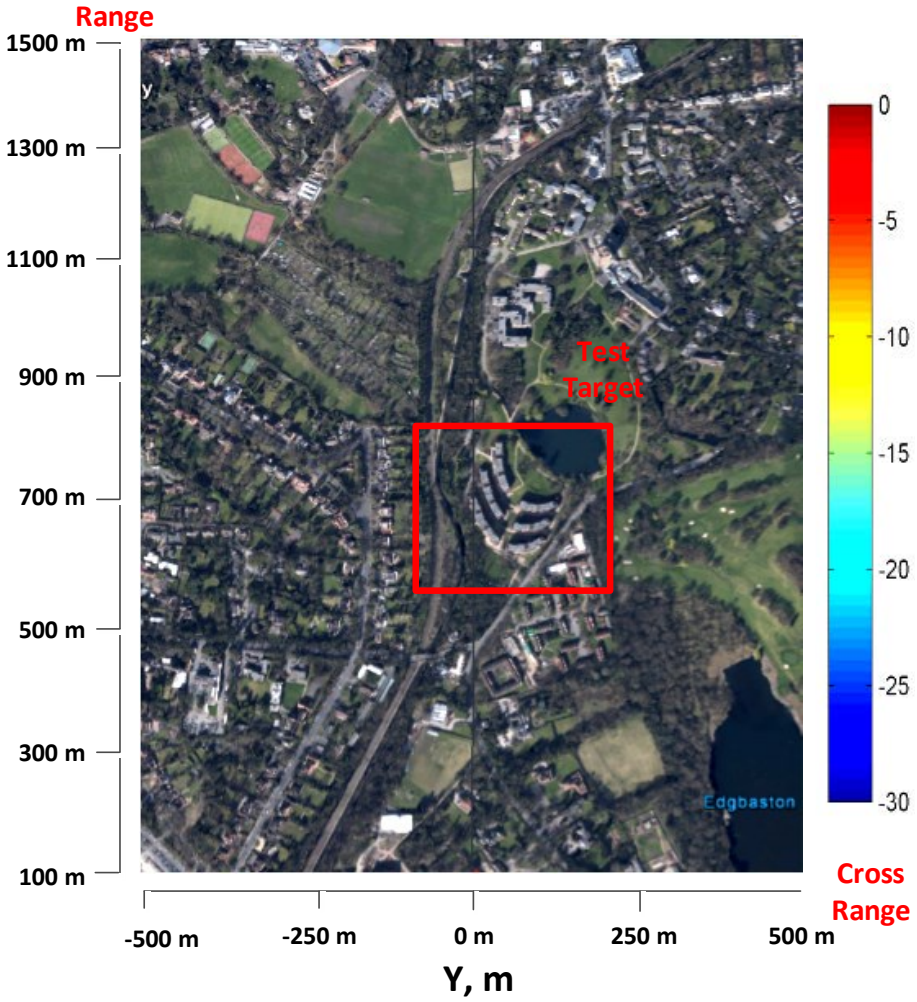

Figure 5-11: Imaged area and selected target

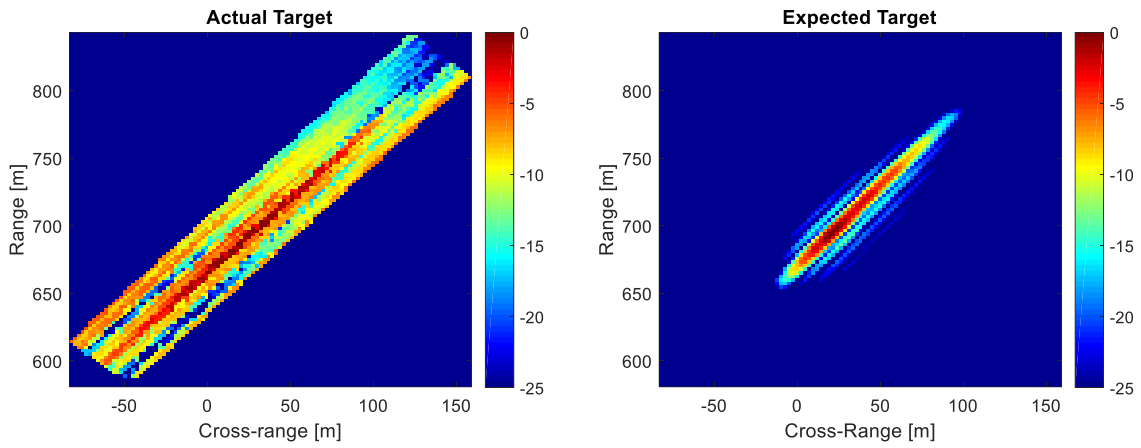

Figure 5-12: Selected target image and Single point image area comparison

Calculating the coherence of the target is done by the same method, but some variables have different values. The differences are:

- Averaging window shape
- Reference for comparison
- Area used for the coherence calculation

The shape of the averaging window for the PSF was square to achieve minimum averaging possible. For the target coherence, the windows is preferred to be rectangular with dimensions ratio of 1:3 or 1:4. This is due to the shape of the PSF that is ellipsoid and not round or square. Thus the dimensions of the averaging windows that were used are 3x9, 3x11 and 3x13.

Another big difference is the reference that is used for the comparisons. In the PSF comparison, each PSF is compared to other PSFs for cross coherence calculation. The target calculation is done using the same reference for all the comparisons.

The reference for the target coherence calculation and comparisons, is the target return that has been isolated from the extended background in the scene. The first image of the area is used for the isolation of the target and creating the reference target.

The figure 5-11 below shows the reference (master image) for all the target coherence calculations. The selected area for the master image is the one that contains the signal return from the target location. The selection for the reference was done considering the highest coherence between the images acquired at the initial antenna position.

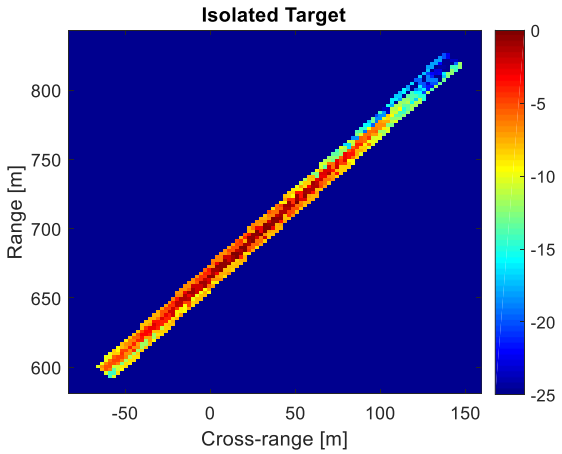

Figure 5-13: Reference target (Isolated target for coherence calculation)

Although four measurements were done for each antenna position only three will be used. This is due to the time separation between the initial three and the fourth for confirmation. In the time period before the last set of measurements were done, a construction for some building maintenance was added next to the target building. Thus, we have the measurements corresponding to the target displacement summarized in Figure 5-14. The images acquired from each antenna position are in Figure 5-15 – Figure 5-18.

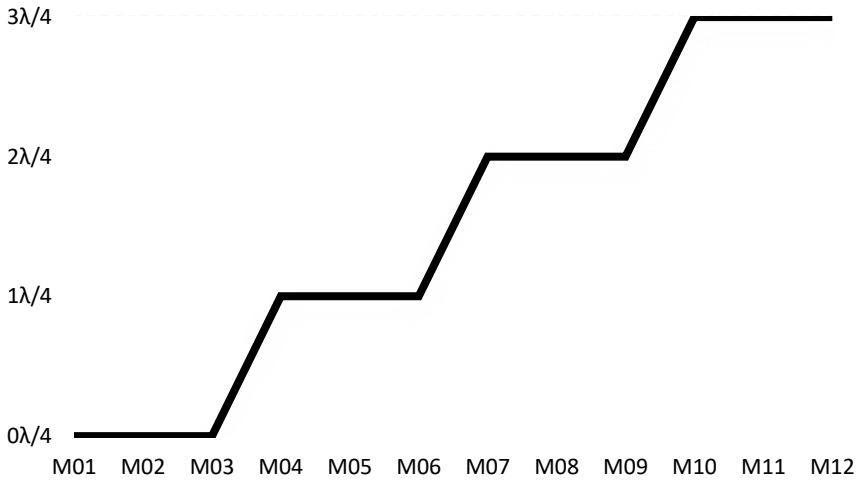

Figure 5-14: Measurements and corresponding Δr variation

The images acquired from each antenna position are resented below.

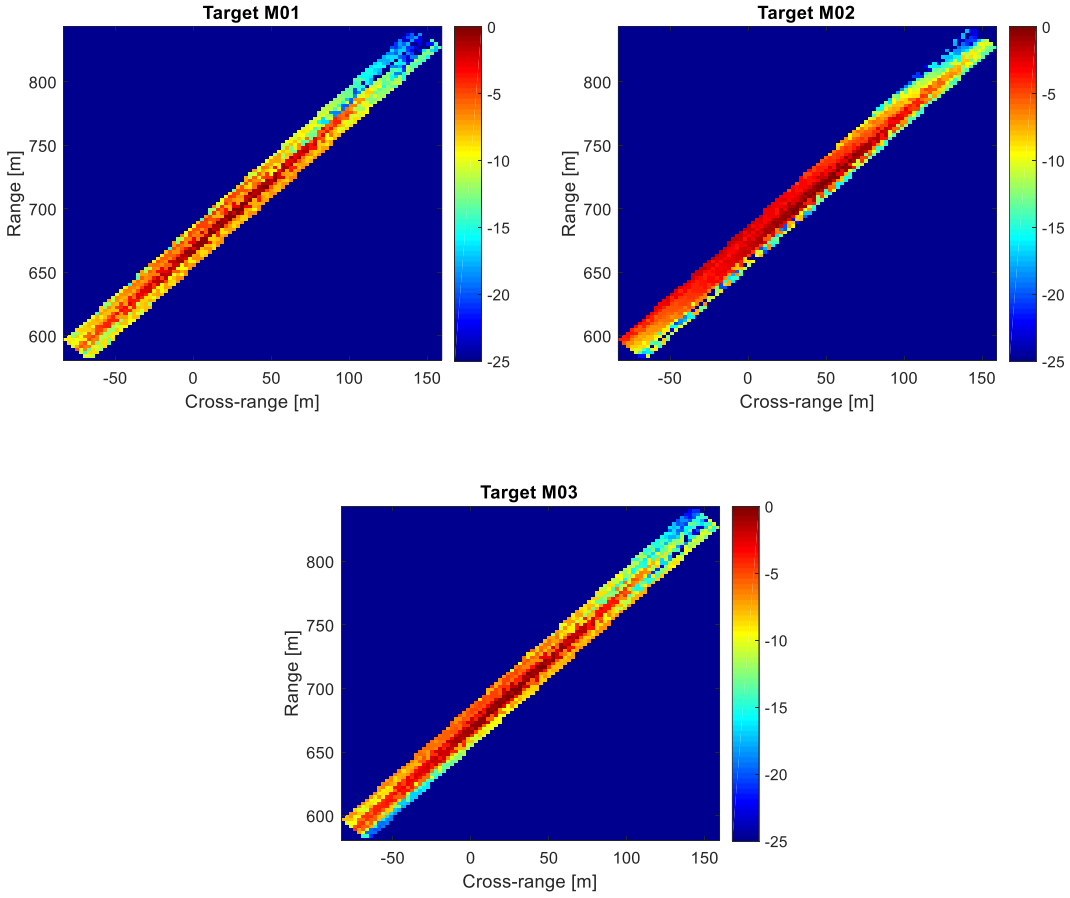

Figure 5-15: Images of reference target (building) at initial antenna position

Calculating the coherence level between the above images provides the opportunity of choosing the reference image for the target comparison at all antenna positions.

In the same way the images acquired at each antenna position are processed for coherence level for every antenna position (antenna positions: λ/4, λ/2 and 3λ/4). In the figures below these cross-comparisons are presented.

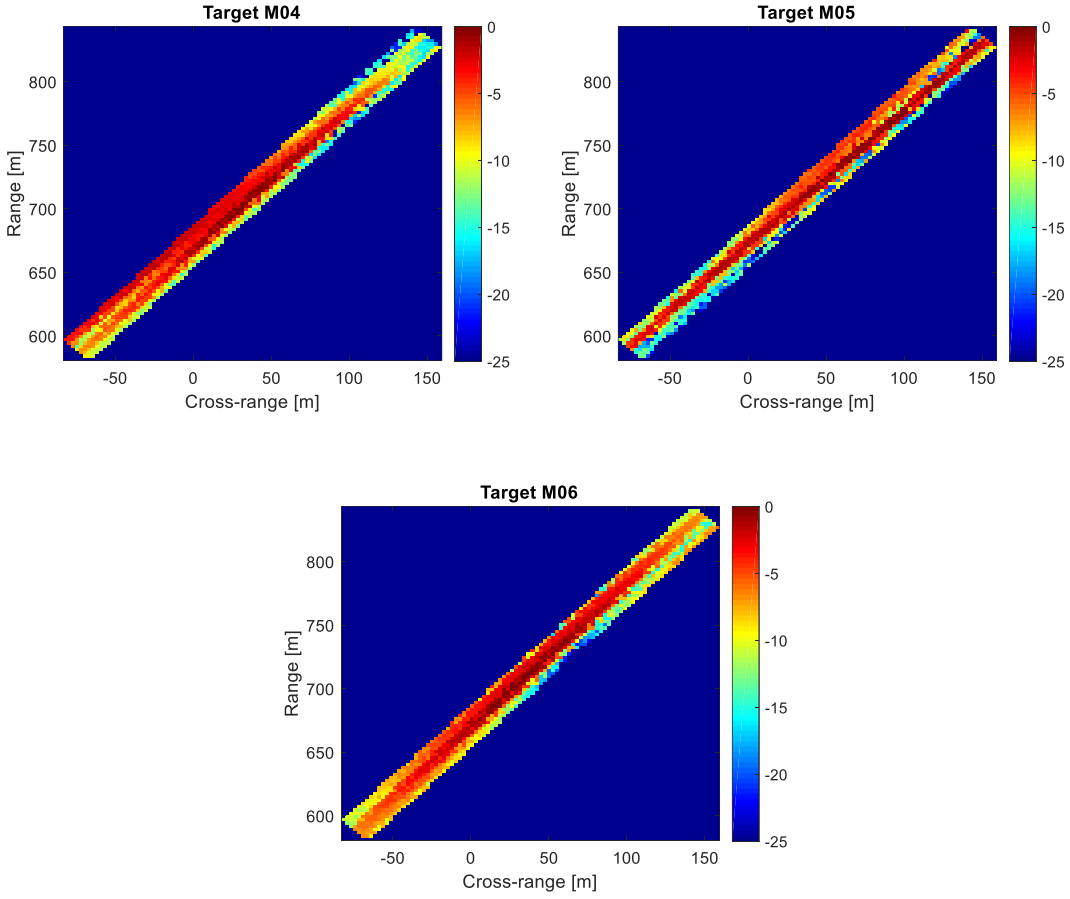

Figure 5-16: Images of reference target (building) at antenna position Δr = λ/4

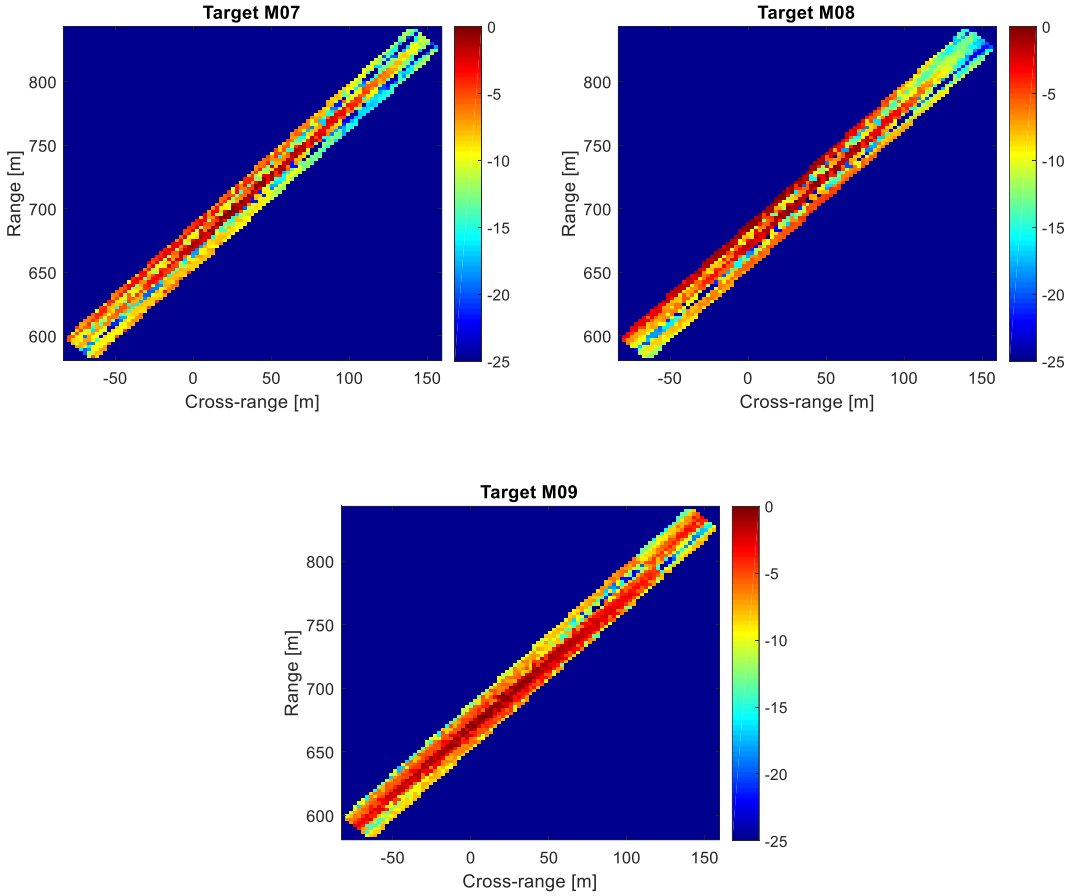

Figure 5-17: Images of reference target (building) at antenna position $\Delta r = \lambda/2$

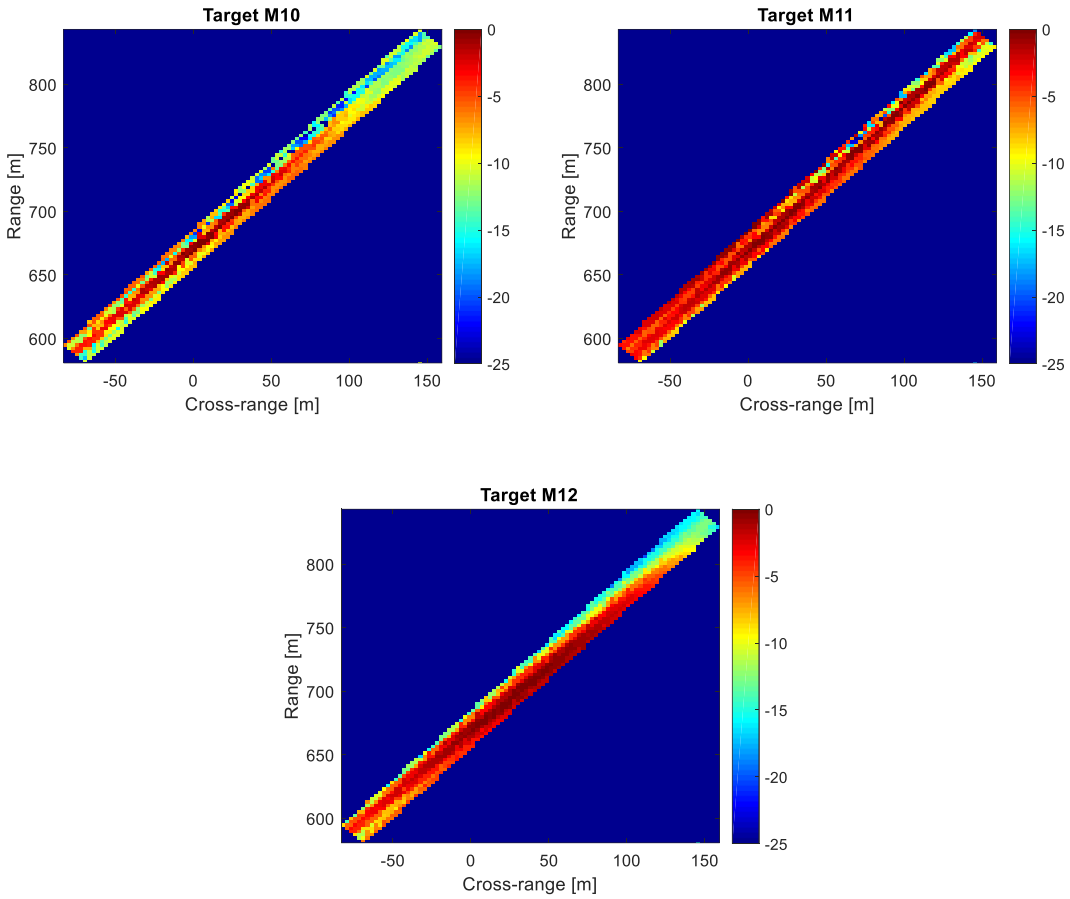

Figure 5-18: Images of reference target (building) at antenna position $\Delta r = 3\lambda/4$

The correlations between the images at the same antenna position are presented in the figures below. In this case the broad area around the target is used for coherence calculation.

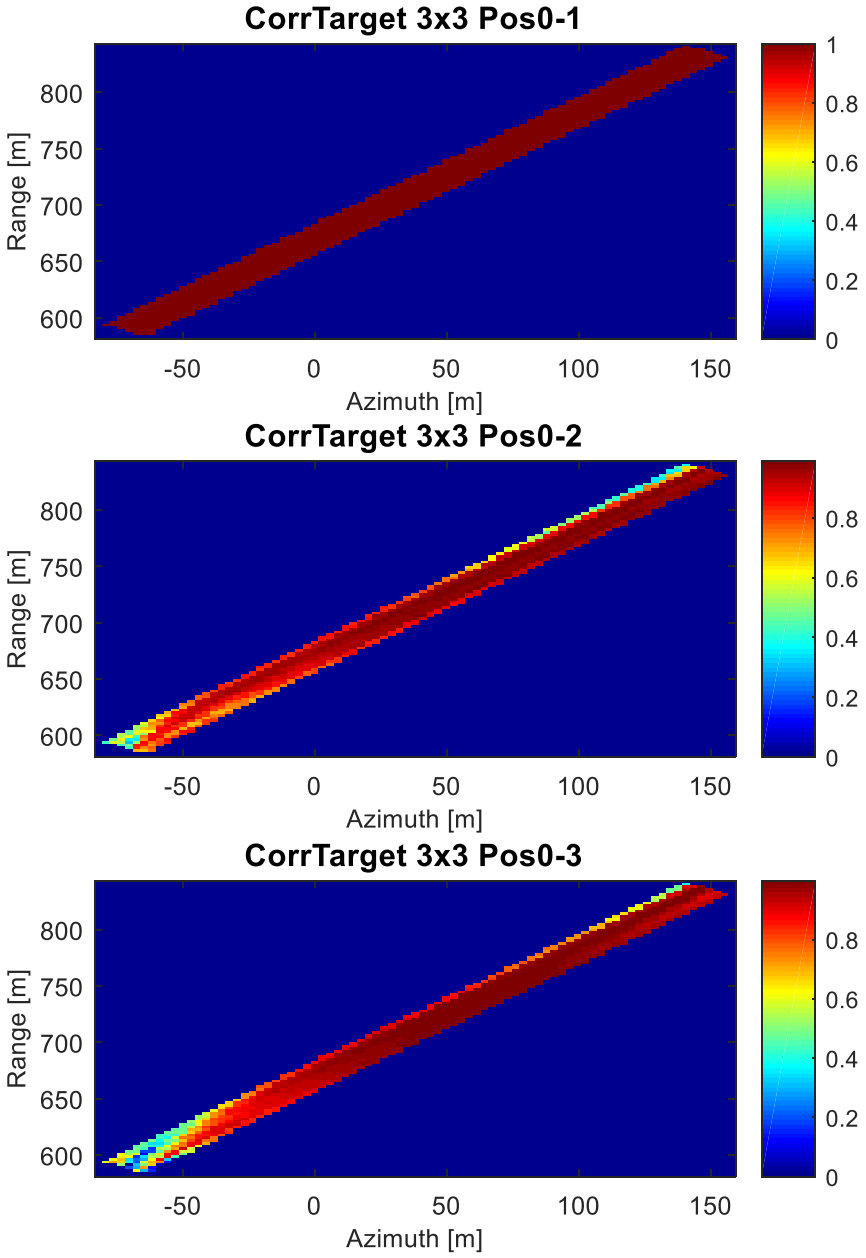

Figure 5-19: Coherence level between images from initial antenna position

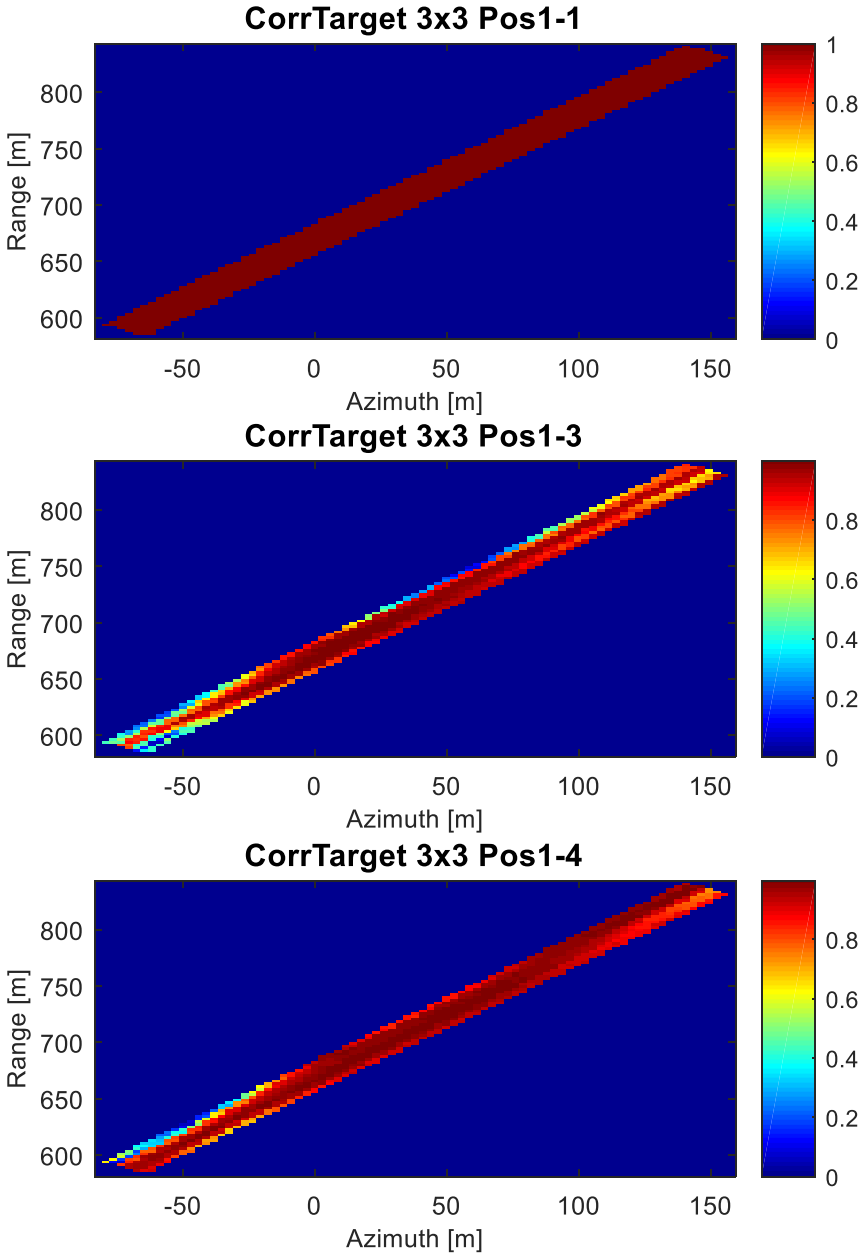

Figure 5-20: Coherence level between images from antenna position $\Delta r = \lambda/4$

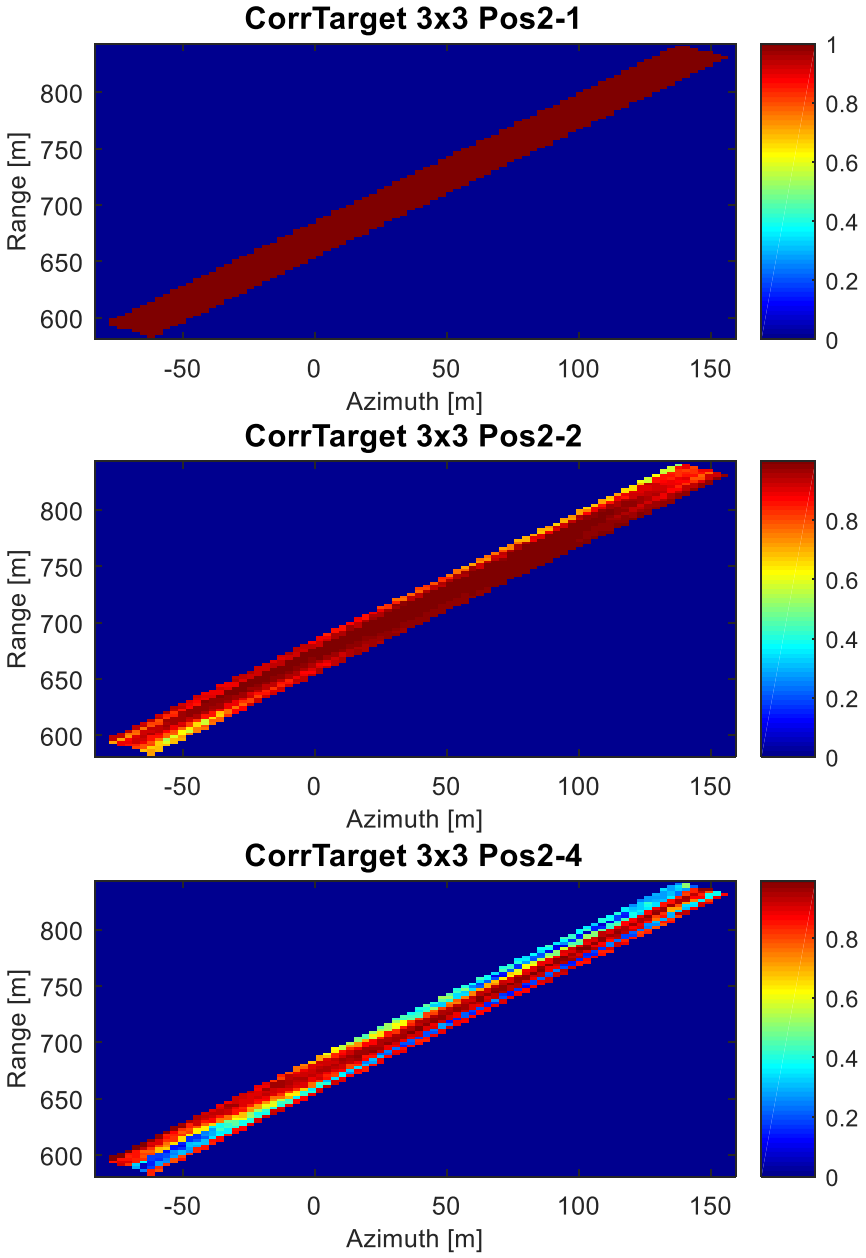

Figure 5-21: Coherence level between images from antenna position $\Delta r = \lambda/2$

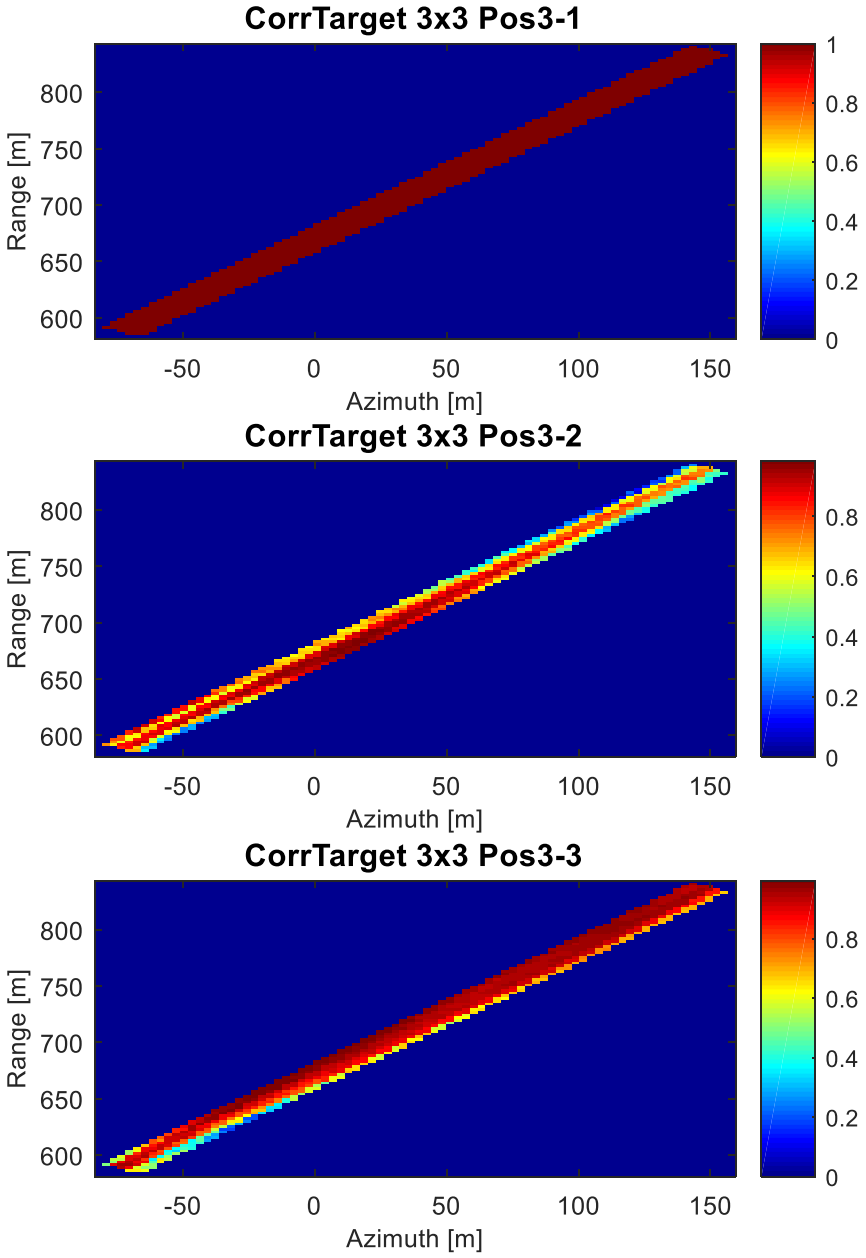

Figure 5-22: Coherence level between images from antenna position $\Delta r = 3\lambda/4$

In the coherence calculations above the averaging window that was used was 3 pixels by 3 pixels for the estimation of the correlation between revisit images with the exactly same configuration. The stability of the measurements can be estimated better. A table with the

values of the coherence between revisit measurements for each antenna position is presented below.

Table 5-2: Master target image of each antenna position (No 1) compared to the slave target images of each antenna position for correlation level

Master compared with	Position $\Delta r = 0$	Position $\Delta r = \lambda/4$	Position $\Delta r = \lambda/2$	Position $\Delta r = 3\lambda 4$
No 1	1	1	1	1
No 2	0.92	0.84	0.92	0.81
No 3	0.89	0.91	0.85	0.93

When a larger averaging window is used for the above calculations, the above results tend to be the value 1, making it difficult the estimation of the revisit stability. The above numbers show that even for the minimum window the correlation is high between images acquired from the same positions. However, the objective is to detect and measure the change that has occurred to the target due to the slight difference of the signal path. The considered displacement of the target is to be examined and estimated. The estimation of the change can be extracted from the correlation of the master image from the initial position with each slave image acquired from every other antenna position. In the table below the coherence between the master from initial antenna position and the slaves from all other positions are presented. The results are acquired by averaging window that is three pixels by eleven pixels (3x11). When a window of dimensions 3x9 or 3x13 is used, the values change by maximum 0.02. Hence, only the window 3x11 is presented and used for the rest of the study.

Table 5-3: Correlation-Coherence level between reference measurement (master) and measurements from different antenna positions (slave) for averaging window (3x9 pixels)

Averaging window = 3 pixels by 9 pixels				
Master compared with slave measurement	Position $\Delta r = 0$	Position $\Delta r = \lambda/4$	Position $\Delta r = \lambda/2$	Position $\Delta r = 3\lambda 4$
No 1	0.963	0.921	0.711	0.925
No 2	0.899	0.783	0.675	0.901
No 3	0.942	0.883	0.535	0.708

Table 5-4: Correlation-Coherence level between reference measurement (master) and measurements from different antenna positions (slave) for averaging window (3x11 pixels)

Averaging window = 3 pixels by 11 pixels				
Master compared with slave measurement	Position $\Delta r = 0$	Position $\Delta r = \lambda/4$	Position $\Delta r = \lambda/2$	Position $\Delta r = 3\lambda 4$
No 1	0.954	0.908	0.711	0.912
No 2	0.892	0.772	0.675	0.884
No 3	0.934	0.873	0.528	0.703

Table 5-5: Correlation-Coherence level between reference measurement (master) and measurements from different antenna positions (slave) for averaging window (3x13 pixels)

Averaging window = 3 pixels by 13 pixels				
Master compared with slave measurement	Position $\Delta r = 0$	Position $\Delta r = \lambda/4$	Position $\Delta r = \lambda/2$	Position $\Delta r = 3\lambda 4$
No 1	0.945	0.902	0.703	0.907
No 2	0.884	0.767	0.668	0.879
No 3	0.925	0.863	0.523	0.697

From the tables above we can see that there are small differences between the values depending on the averaging window. However, we can observe that the variations in the values are at similar levels. Also, it can be noticed that the results for each antenna position of $\Delta r = \lambda/4$ and $\Delta r = 3\lambda/4$ are at the same levels. This is something expected as the difference on the target-receiver distance is translated in phase. The $\lambda/4$ distance difference to the initial antenna position add a phase of $\pi/2$ to the initial antenna position received signal, whereas the $3\lambda/4$ distance difference adds a phase that is $3\pi/2$ or $-\pi/2$. Thus, the calculation of the coherence will provide same level results.

Although for every image pixel there are many scatter points that contribute to the return signal value, we can consider that when the absolute distance between the target and the receiver is changed by an addition of $\lambda/4$ then each scatter point will be approximately $\lambda/4$ further away. In other words, as the absolute distance from the target increases, the absolute distance of each scatter point of the target increases by the same amount. That is the reason why we expect that the antenna movement can emulate the target movement. Using the above estimation, we can compare the experimental results for an antenna position to a simulation result.

Using the model for the calculation of the correlation coefficient due to temporal change that is explained in chapter 3, and using the topology used in the data acquisitions we calculate the theoretical value of the correlation coefficient. In the following figure we present the coherence level in relation to a Δr displacement (target displacement or equivalent antenna movement)

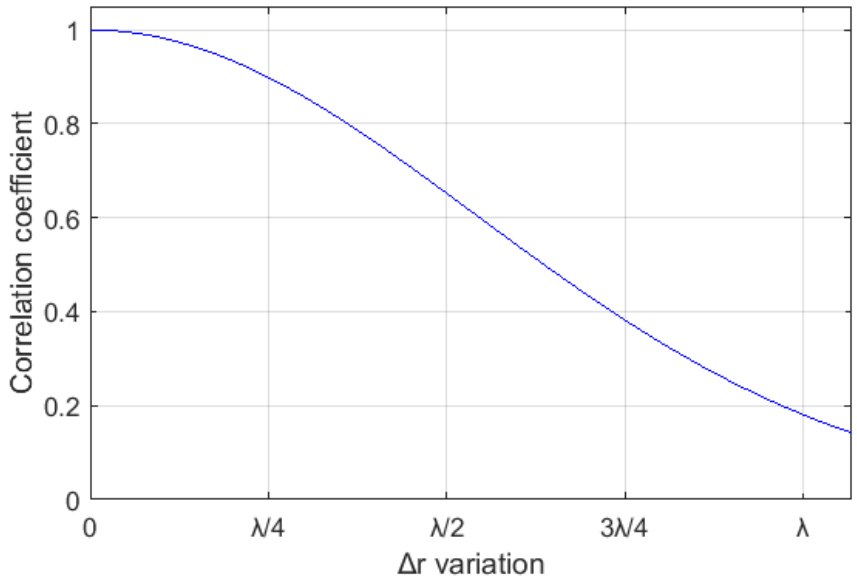

Figure 5-23: Theoretical coherence calculation for Δr variation

On the graph above we can observe that the correlation factor is dropping even for $\Delta r = 3\lambda/4$. This is the model used for the calculation of the coherence when a Δr is applied. As it has been explained before in the thesis, the resolution of the system covers in average an area of 40 meters in range and 5 meters in azimuth, whereas every image pixel represents an area two meters by two meters (2m x 2m). Using theoretical values from the above plot, we can plot on the same graph the theoretical correlation coefficient calculated and the experimental results for comparison. The combined graph is shown below.

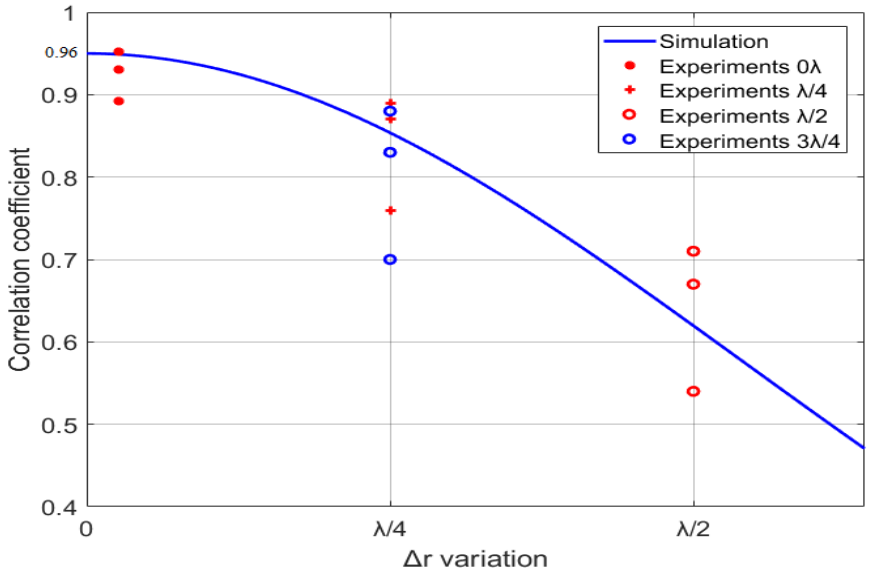

Figure 5-24: Simulation and experimental results

In the figure above we see theoretical value of the correlation coefficient in the blue line and the points that correspond to respective experimental results. Additionally we have included a decorrelation factor due to the non-temporal effects as a factor of 0.96, as it has been observed from the PSF comparisons and the coherence values calculated. Due to the coherence calculation process, and because the target dimensions are bigger than the system resolution, the values from antenna position at $\Delta r = 3\lambda/4$ are considered as negative phase, for example as for $\Delta r = -\lambda/4$. With this into account the correlation coefficient will be compared as $|\Delta r|$. Taking here the absolute value for the phase difference we can plot it on the same graph.

From Figure 5-24 presented above, we can confirm that the experimental results coincide with the theoretical values.

5.6. Phase information

The correlation between the images acquired has been presented but this is one part of the study. From the results above we can connect the coherence level between two measurements to the Δr displacement. Moving further the study it is important to investigate the phase information in the images. For the phase calculation we will need again both signals, direct and reflected. Keeping in mind that the direct signal path has not been modified during the whole period of the experiments, the phase will give us any trajectory errors from measurement to measurement. This phase difference on the direct signal will be taken into account for the calculation of the target phase difference (measured distance of target displacement) too. Starting with the initial antenna position (Δr = 0) we get the phase difference between one measurement and the rest measurements as:

Table 5-6: PSF phase difference calculations at antenna position Δr = 0

Phase comparison between measurements	Phase difference in degrees
Ref – M01	0
Ref – M02	-40
Ref – M03	9

The table above shows the stability of the measurements at this position. Any phase difference on the direct signal image should be subtracted from the target reflected signal.

Calculating now the phase for the target image, and combining it with the above results we get the following table.

Table 5-7: Target phase difference calculations for antenna position $\Delta r = 0$

Phase comparison between measurements	**PSF Phase difference [in degrees]**	**Target phase difference [in degrees]**	**Actual target phase difference [in degrees]**
Ref – M01	0	0	0
Ref – M02	-40	-87	-47
Ref – M03	9	50	41
Average			**-2**

We can see from the above results that the phase difference is calculated for each measurement individually and the average value is minus two degrees (-2 deg). Therefore we can continue to the next antenna positions and perform the same process for the phase calculation.

Table 5-8: Target phase difference calculations for antenna position $\Delta r = \lambda/4$

Phase comparison between measurements	**PSF Phase difference [in degrees]**	**Target phase difference [in degrees]**	**Actual target phase difference [in degrees]**
Ref – M04	-18	63	81
Ref – M05	-34	77	111
Ref – M06	-26	97	123
Average			**105**

Table 5-9: Target phase difference calculations for antenna position $\Delta r = \lambda/2$

Phase comparison between measurements	PSF Phase difference [in degrees]	Target phase difference [in degrees]	Actual target phase difference [in degrees]
Ref – M07	-17	144	161
Ref – M08	-40	98	138
Ref – M09	-27	165	192
Average			**163**

Table 5-10: Target phase difference calculations for antenna position $\Delta r = 3\lambda/4$

Phase comparison between measurements	PSF Phase difference [in degrees]	Target phase difference [in degrees]	Actual target phase difference [in degrees]
Ref – M10	-44	269	313
Ref – M11	-42	206	248
Ref – M12	-45	276	311
Average			**290**

From the above experimental results we can see that there is a maximum of 20 degrees error calculation for the average phase for each antenna position and the maximum individual error doesn't go over 50 degrees.

5.7. Calculation of distance from phase

The phase information can easily be transformed into distance information. The complex form for to connect the distance with the phase is shown in the equation below:

$$s_2 = s_1 \cdot e^{-2\pi i(\Delta r)} \tag{5.1}$$

but where the complex form is not needed, a simpler equation can be used. The simpler form is as shown below:

$$\Delta r = \frac{C}{4\pi f}\Delta\phi \tag{5.2}$$

Using the equation (5.2) we calculate the distance in centimetres for easier understanding and comparison to the expected experimental distance estimation. The following table shows the calculations for each antenna position in degrees and centimetres.

Table 5-11: Phase to distance and error calculations

Parameter	**Δr = 0**	**Δr = λ/4**	**Δr = λ/2**	**Δr = 3λ/4**
Measured phase	-2 deg	105 deg	163 deg	290 deg
Measured Δr	-0.052 cm	5.47 cm	8.49 cm	15.10 cm
Expected Δr	0 cm	4.68 cm	9.36 cm	14.04 cm
Error in Δr	**-0.052 cm**	**0.79 cm**	**-0.87 cm**	**1.06 cm**
Error in Δr expressed in phase terms	-2 deg	+15 deg	-17 deg	+20 deg

5.8. Error estimation

The results presented in this chapter confirm the expected and the theoretical values with a reasonable accuracy. From the tables shown the maximum error is near 20 percent of the

theoretical values. For the proposed system with its specifications, the results provide a good proof of concept despite the errors. The system used a mechanical way to emulate the real target displacement and coherent change detection techniques for the detection of the change. A source of possible error introduction, perhaps the major error introduction factor, in the experiments is the antenna movement. In order to create the 0.05 m difference in the target-receiver antenna range, it was moved sideways by the distance of 1 m. This probably affects the experiments as far it has to deal with scatter points and major scatter contributors. When the viewing angle of a target is changed, even by a very small amount, the scatter points might be changed. Thus, a possible error source is this one. It has been explained in the previous chapter why such topology was used. Despite this, the system has proved its capabilities.

5.9. Conclusions

In this chapter the Coherent Change Detection results have been presented. PSF comparisons for experimental stability are calculated and non-temporal decorrelation is estimated. The acquired images from the scene are generated and the target area is isolated to the target coherence calculation. The correlation coefficient is calculated for the each image to the reference one in pairs and the coherence level is estimated. The results confirm the theoretical model with good accuracy. Along with the correlation coefficient, phase calculations are performed for each measurement and the results are presented. The phase information confirms the occurred temporal change. It has been shown that the optimal measurement accuracy is better than 1 cm. The errors have been analysed and possible factors that might create errors have been explained.

Chapter 6 Conclusions and future work

6.1. Summary and conclusions

The aim of this thesis is to investigate whether or not it is plausible to use GNSS-based SAR images to monitor scene changes. For this reason we investigated:

a) *A model of temporal de-correlation effects in GNSS-based SAR and its relationship to scene displacements*

GNSS-based SAR temporal decorrelation effects were modelled and the model was tested. It was found that the sensitivity to temporal changes varies with the bistatic geometry. The model was compared to Monte Carlo simulation. The comparison shows that the model is a good approach for the temporal change and its relation to the correlation coefficient.

b) *The development of a CCD algorithm for GNSS-based SAR images*

A CCD algorithm was developed for the GNSS-based SAR images. This algorithm is taking into account the factors that affect the coherence between a SAR image pair. The study of the coherence factors helps in developing ways to keep the unwanted decorrelation in low levels. The unwanted decorrelation occurs due to the thermal and the spatial decorrelation factors. Appropriate measures for keeping the thermal and spatial decorrelation factors to minimum are studied.

c) *The design and execution of a proof-of-concept experimental campaign to confirm the feasibility of GNSS-based SAR change detection*

The application of the algorithm for CCD in GNSS-based SAR was used in an experimental campaign. The experimental campaign is designed to study the feasibility of GNSS-based SAR change detection with experimental data in a real scene. During the experimental campaign many challenges appeared. The minimization of the thermal and spatial decorrelation was achieved with appropriate measures. At the same time, the temporal decorrelation was studied experimentally on real target. However, the fact that the target was a building block that cannot be moved, the temporal change was achieved with the antenna movement. The needed antenna displacement was calculated, and the experiment was designed for accurate repetition. The experiments covered a period of several months without any problem, apart from the weather, since the equipment is not waterproof at this stage, just for research.

d) A comparison between theoretical and experimental results to confirm the validity of theoretical models

To confirm the model, displacements of the target were emulated with the antenna movement. The tested target displacements were $\lambda/4$, $\lambda/2$ and $3\lambda/4$. At each position the stability was estimated and the temporal decorrelation was calculated. The experimental results were compared to the theoretical ones using the proposed model for the decorrelation calculation. The temporal decorrelation calculated theoretically is confirmed by the experimental data. However, there are small deviations, but they are expected in a real system. The experiments were conducted in a real environment with real target. Also, the target return consisted of a block of buildings. The phase information that was extracted

showed also the expected temporal change. Therefore, it can be used in the GNSS-based SAR for CCD, and maybe some more advance CCD techniques can be used. With the results from this study we can conclude that GNSS-based SAR monitoring is feasible.

6.2. Future work

The results that are provided in this thesis with experimentation on real target returns show that the accuracy is satisfying. However there is always room for improvement. Some steps forward this point can be:

- Developing the next generation equipment with which the data processing can be real time instead of post-processing that is used for the moment.
- Area monitoring using multi-view imaging. This can be achieved with the use of more than one satellite for the area observation. This will enable the capability of estimating also the direction of the change. This can also achieved with the combination of results acquired from different constellation satellite.
- Using CCD on combined Galileo signals where achieved resolution can be greatly increased.
- Apply advance CCD techniques for temporal change calculation using the phase information.
- Move beyond CCD techniques to local area observation via interferometric techniques.

References

[1] M. A. Richards, J. A. Scheer, and W. A. Holm, “Principles of Modern Radar,” *Basic Princ.*, vol. I, p. 924, 2010.

[2] M. Cherniakov, *Bistatic radar : principles and practice*. Chichester, England Hoboken, NJ: John Wiley, 2007.

[3] G. Stimson, *Introduction to airborne radar*, 2nd Ed. Mendham, N.J: SciTech Pub, 1998.

[4] D. Barton, *Modern radar system analysis*. Norwood, MA: Artech House, 1988.

[5] M. Skolnik, *Radar Handbook, Third Edition*, 3rd Editio. New York: McGraw-Hill, 2008.

[6] W.G. Carrara, R.S. Goodman, R.M. Majewski, *Spotlight Synthetic Aperture Radar*, Artech House, 1995.

[7] I.G. Cumming, F.H. Wong, *Digital processing of Synthetic Aperture Radar data*, Artech House, 2005.

[8] P. Dubois-Fernandez et al, “ONERA-DLR bistatic SAR campaign: planning, data acquisition, and first analysis of bistatic scattering behaviour of natural and urban targets”, IET Proc. In Radar, Sonar and Navigation, vol. 153, no. 3, pp. 214-223 , June 2006.

[9] M. Rodriguez-Cassola et al, “First bistatic spaceborne SAR experiments with Tandem-X”, IEEE Geoscience and Remote Sensing Letters, vol. 9, no. 1, pp. 33-37, January 2012.

[10] Moreira et al, “Tandem-L: a highly innovative bistatic SAR mission for global observation of dynamic processes on the Earth’s surface”, IEEE Geoscience and Remote Sensing Magazine, vol. 3, no. 2, pp. 8-23, June 2015.

[11] R. Wang, O. Loffeld, H. Nies, J.H.G. Ender, “Focusing spaceborne/airborne hybrid bistatic SAR data using wavenumber-domain algorithm”, IEEE Trans. On Geoscience and Remote Sensing, vol. 47, no. 7, pp.2275-2283, July 2009.

[12] D. Martinsek, R. Goldsteing, “Bistatic radar experiment”, EUSAR 1998, pp. 31-34.

[13] M. Rodriguez-Cassola et al., “Bistatic TerraSAR-X/F-SAR spaceborne–airborne SAR experiment: description, data processing, and results”, IEEE Trans. on Geoscience and Remote Sensing, vol. 48, no.2, pp. 781-794, February 2010.

[14] Walterscheid et al., “Bistatic SAR experiments with PAMIR and TerraSAR-X—setup, processing, and image results”, IEEE Trans. on Geoscience and Remote Sensing, vol. 48, no. 8, pp. 3268-3279, August 2010.

[15] R. Wang et. al, “Double-channel bistatic SAR system with spaceborne illuminator for 2-D and 3-D SAR remote sensing”, IEEE Trans. on Geoscience and Remote Sensing, vol. 51, no. 8, pp. 4496-4507 , August 2013.

[16] T. Zeng, R. Wang, F. Li, T. Long, “A modified nonlinear chirp scaling algorithm for spaceborne/stationary bistatic SAR based on series reversion” , vol. 51, no. 5, pp. 3108-3118, May 2013.

[17] F. Behner, S. Reuter, “S. HITCHHIKER-hybrid bistatic high resolution SAR experiment using a stationary receiver and TerraSAR-X transmitter”, EUSAR 2010, pp. 1030-1033.

[18] Antoniou M., “Image formation algorithms for space-surface bistatic SAR”, Ph.D Thesis, University of Birmingham, 2007.

[19] Cherniakov M., Zeng T., Plakidis E., “Ambiguity function for bistatic SAR and its application in SS-BSAR performance analysis,” Proceedings of the international radar conference, pp. 343-348, 2003.

[20] Zeng T., Cherniakov M., Long T., "Generalized approach to resolution analysis in BSAR," IEEE Transactions on Aerospace and Electronic Systems, vol. 41, pp. 461-474, 2005.

[21] He X., Zeng T., Cherniakov M., "Interference level evaluation in SS-BSAR with GNSS non-cooperative transmitter," Electronics letters, vol. 40, pp. 1222-1224, 2004.

[22] He X., Zeng T., Cherniakov M., "Signal detectability in SS-BSAR with GNSS non-cooperative transmitter," IEE Proceedings Radar, Sonar and Navigation, vol. 152, pp. 124-132, 2005.

[23] Cherniakov M, Zeng T., Plakidis E., "Galileo signal-based bistatic system for avalanche prediction," IGARSS, vol. 2, pp. 784-786, 2003

[24] Antoniou M., Cherniakov M., Zeng T., "Problems of surface change detection based on SS-InBSAR," IEEE International Radar Conference, pp. 791-795, 2005

[25] Anoniou M., Cherniakov M., Saini R., Edwards J., Zuo R., "Modified rangedoppler algorithm for space-surface BSAR imaging," CIE International Conference on Radar, pp. 1-4, 2006

[26] Antoniou M., Saini R., Zuo R., Cherniakov M., "Image formation algorithm for space-surface BSAR," European Radar Conference, pp. 413-416, 2007

[27] Antoniou M., Saini R., Cherniakov M., "Results of a space-surface bistatic SAR image formation algorithm," IEEE Transactions on Geoscience and Remote Sensing, vol. 45, pp. 3359-3371, 2007

[28] Antoniou M., Saini R., Zuo R., Cherniakov M., "Space-surface bistatic SAR topology and its impact on image formation," EUSAR, pp. 1-4, 2008

[29] Antoniou M., Cherniakov M., Hu C., "Space-surface bistatic SAR image formation algorithms," IEEE Transactions on Geoscience and Remote Sensing, vol. 47, pp. 1827-1843, 2009

[30] Saini R., Zuo R., Cherniakov M., “Signal synchronization in SS-BSAR based on GLONASS satellite emission,” IET International conference on Radar Systems, pp. 1-5, 2007

[31] Saini R., Zuo R., Cherniakov M., “Problem of signal synchronization in spacesurface bistatic synthetic aperture radar based on global navigation satellite emissions-experimental results,” IET Radar, Sonar & Navigation, vol. 4, pp. 110-125, 2010

[32] Cherniakov M., Saini R., Zuo R., Antoniou M., “Space-surface bistatic synthetic aperture radar with global navigation satellite system transmitter of opportunity-experimental results,” IET Radar, Sonar & Navigation, vol. 1, pp. 447-458, 2007

[33] Saini R., Zuo R., Cherniakov M., “Development of space-surface bistatic synthetic aperture radar with GNSS transmitter of opportunity,” IEEE Radar conference, pp. 1-6, 2008.

[35] Russian Institute of Space Device Engineering, “Global Navigation Satellite System (GLONASS) Interface Control Document”, Edition 5.1, 2008.

[36] China Satellite Navigation Office, “BeiDou Navigation Satellite System Signal In Space Interface Control Document, Open Service Signal”, 2013.

[37] Global Positioning Systems Wing (Systems Engineering and Integration), “Navstar GPS space segment/navigation user interfaces”, IS-GPS-200, Rev. E, 2010.

[38] European GNSS Open Service Signal-in-Space Interface control document (OS SIS ICD), Issue 1.1, September 2010.

[39] G.R. Lennen, “The USSR’s GLONASS P-code- determination and initial results”, ION GPS, pp. 77-83, 1989.

[40] R. Zuo, Bistatic synthetic aperture radar using GNSS as transmitters of opportunity, Ph. D. thesis, University of Birmingham, UK, 2012.

[41] J. Tsui, Fundamentals of Global Positioning System Receivers (Wiley, New York, 2004)

[42] M. Antoniou, M. Cherniakov, “GNSS-based bistatic SAR: a signal processing view”, EURASIP Journal on Advances in Signal Processing, vol. 2013:98, May 2013. Available online at: http://asp.eurasipjournals.com/content/2013/1/98

[43] Soumekh M: *Synthetic Aperture Radar Signal Processing with MATLAB Algorithms*. Wiley, New York; 1999.

[44] M. Cherniakov (Ed.), Bistatic Radar- Emerging Technology, Wiley, 2008.

[45] F. Liu, M. Antoniou, Z. Zeng, M. Cherniakov, “Coherent Change Detection Using Passive GNSS-Based BSAR: Experimental Proof of Concept”, IEEE Trans. on *Geoscience and Remote Sensing*, vol. 51, no. 8, pp. 4544-4555, August 2013.

[46] N. J. Willis, Bistatic Radar, Boston, MA: Artech House, 1991.

[47] F. Liu, M. Antoniou, Z. Zeng, M. Cherniakov, “Point Spread Function Analysis for BSAR With GNSS Transmitters and Long Dwell Times: Theory and Experimental Confirmation”, IEEE Geoscience and Remote Sensing Letters, vol. 10, no. 4, pp. 781-785, July 2013.

[48] Zebker, H. A., & Villasenor, J. (1992). Decorrelation in interferometric radar echoes. IEEE Transactions on Geoscience and Remote Sensing, 30(5), 950–959.

[49] E. Rodriguez, and J. M. Martin, “Theory and design of interferometric synthetic aperture radars,” IEE Proceedings-F, vol. 139, no. 2, pp.147-159, 1992.

[50] Q. Zhang, M. Antoniou, W. Chang and M. Cherniakov, "Spatial Decorrelation in GNSS-Based SAR Coherent Change Detection," in *IEEE Transactions on Geoscience and Remote Sensing*, vol. 53, no. 1, pp. 219-228, Jan. 2015.

[51] J. M. Goodman, “Statistical properties of laser speckle patterns,” *Topics Appl. Phys.*, vol. 9, pp. 9–75, 1975.

[52] Neo Y. L., “Digital processing algorithms for bistatic synthetic aperture radar data,” Ph.D thesis, 2007

APPENDIX A

LAGRANGE INTERPOLATION

Lagrange interpolation is a linear polynomial interpolation, given there is a Lagrange polynomial passing through *n+1* point sets

$$(x_0, y_0), (x_1, y_1), (x_2, y_2), \ldots, (x_n, y_n) \tag{A.1}$$

where $(x_i)_{0 \le i \le n}$ is defined as points of interpolation and $(y)_{0 \le i \le n}$ is defined as values of interpolation. The Lagrange polynomial is given by:

$$y(x) = \sum_{i=0}^{n} y_i L_i \tag{A.2}$$

where $L_i = \prod_{\substack{0 \le m \le n \\ m \ne n}} \frac{x - x_m}{x_i - x_m} = \frac{(x - x_1) \cdot (x - x_2) \cdot \ldots \cdot (x - x_{i-1}) \cdot (x - x_{i+1}) \cdot \ldots \cdot (x - x_n)}{(x_i - x_1) \cdot (x_i - x_2) \cdot \ldots \cdot (x_i - x_{i-1}) \cdot (x_i - x_{i+1}) \cdot \ldots \cdot (x_i - x_n)}$

Hence, the polynomial evaluated at x_i could be obtained by following equation:

$$\begin{aligned} y_i = & \frac{(x_i - x_2) \cdot (x_i - x_3) \cdot \ldots \cdot (x_i - x_n)}{(x_1 - x_2) \cdot (x_1 - x_3) \cdot \ldots \cdot (x_1 - x_n)} y_1 \\ & + \frac{(x_i - x_1) \cdot (x_i - x_3) \cdot \ldots \cdot (x_i - x_n)}{(x_2 - x_1) \cdot (x_2 - x_3) \cdot \ldots \cdot (x_2 - x_n)} y_2 \\ & + \ldots + \frac{(x_i - x_1) \cdot (x_i - x_2) \cdot \ldots \cdot (x_i - x_{n-1})}{(x_n - x_1) \cdot (x_n - x_2) \cdot \ldots \cdot (x_n - x_{n-1})} y_n \end{aligned} \tag{A.3}$$

APPENDIX B

PUBLICATION LIST

1. F. Santi, D. Pastina, M. Bucciarelli, M. Antoniou, D. Tzagkas and M. Cherniakov, "Passive multistatic SAR with GNSS transmitters: Preliminary experimental study," *2014 11th European Radar Conference*, Rome, 2014, pp. 129-132

2. F. Santi, M. Antoniou, D. Pastina, D. Tzagkas, M. Bucciarelli and M. Cherniakov, "Passive multi-static SAR with GNSS transmitters: first theoretical and experimental results with point targets," *EUSAR 2014; 10th European Conference on Synthetic Aperture Radar*, Berlin, Germany, 2014, pp. 1-4

3. D. Tzagkas, M. Antoniou and M. Cherniakov, "Coherent Change Detection experiments with GNSS-based passive SAR," *2016 European Radar Conference (EuRAD)*, London, 2016, pp. 262-265.

4. H. Ma, D. Tzagkas, M. Antoniou, M. Cherniakov, "Maritime Moving Target Indication and Localisation with GNSS-based MultiStatic Radar: Experimental Proof of Concept", *International Radar Symposium 2017*, Prague, 2017